

Dmytro Byelov

A SANS study of microemulsions with
polymer additions

2003

Physikalische Chemie

**A SANS study of microemulsions with
polymer additions**

Inaugural-Dissertation
zur Erlangung des Doktorgrades der Naturwissenschaften
im Fachbereich Chemie und Pharmazie
der Mathematisch-Naturwissenschaftlichen Fakultät
der Westfälischen Wilhelms-Universität Münster

vorgelegt von

Dmytro Byelov
aus Odessa, Ukraine

- 2003 -

Dekan:	Prof. Dr. Jens Leker
Erster Gutachter:	Prof. Dr. Dieter Richter
Zweiter Gutachter:	Prof. Dr. Hellmut Eckert
Tag der mündlichen Prüfungen:	30,01,2004; 02,02,2004; 05,02,2004
Tag der Promotion:	05,02,2004

Contents

1	Introduction	1
2	Thermodynamics of microemulsions	5
2.1	From membrane properties to the bicontinuous microemulsion . . .	5
2.1.1	Curvature energy	5
2.1.2	Gaussian Random Field approximation	8
2.1.3	Diblock copolymer addition	10
2.1.4	Homopolymer addition	11
2.1.5	Addition of homopolymer and diblock copolymer	12
2.1.6	Ginzburg-Landau model for the scattering intensity	12
2.2	Theory of droplet microemulsions	15
2.2.1	General part	15
2.2.2	Fluctuations of spherical droplets.	17
2.2.3	Droplet to cylinder phase transition	19
2.2.4	Addition of diblock copolymer	22
2.3	Scattering functions of droplet microemulsions	25
2.3.1	Introduction	25
2.3.2	Core-shell sphere formfactor	27
2.3.3	Core-shell ellipsoid of revolution formfactor	28
2.3.4	Core-shell cylinder formfactor	29
2.3.5	Polydispersity	30
2.3.6	Structure factor	31
3	Aspects of small angle neutron scattering	33
3.1	Experimental setup	33
3.2	Absolute calibration	34
3.3	Resolution effects	36
3.4	Multiple scattering	37
4	Sample preparation	41

5	The bicontinuous phase	43
5.1	Results	43
5.1.1	Addition of homopolymers only	45
5.1.2	Simultaneous addition of homopolymers and diblock copolymers	52
5.2	Discussion	60
6	The droplet phase microemulsion	65
6.1	Results	65
6.2	SANS	68
6.2.1	Droplets at low oil content and low temperature	69
6.2.2	Bidisperse objects - low oil content and low temperature	72
6.2.3	Droplets at low oil content and high temperature	73
6.2.4	Droplets at high oil contents	76
6.3	Discussion	80
7	Summary and Conclusions	87
	Appendix	91
	A: Tables of compositions	91
	B: The effect of diblock copolymer addition	95
	List of Figures	99
	List of Tables	102
	Bibliography	104
	Acknowledgments	109
	CV(Lebenslauf)	111

Chapter 1

Introduction

In applications polymers are added to oil-water-surfactant mixtures for various reasons. In this study we focus on small polymer additions, which change the emulsification behaviour of the surfactant. According to recent works [1,2] the addition of amphiphilic diblock copolymers to balanced bicontinuous microemulsions causes a dramatic increase of the surfactant efficiency. We will extend the application of diblock copolymers to the droplet phase. As a complementary study, we investigate the effect of homopolymers, which would allow to tune the viscosity of the microemulsion. Tuning the emulsification behaviour and/or viscosity might find application in cosmetics, detergents, cleaning agents and paints.

Microemulsions consist of two otherwise non-miscible components oil and water, which are mediated by a third component, the surfactant. Oil and water form domains, which are separated by the surfactant film. It has been established that the microemulsion is dominated by the surfactant layer properties. All theoretical descriptions focus on the surface energy as the main contribution to the free energy [3]. Helfrich [4] introduced two bending moduli κ and $\bar{\kappa}$ of the mean curvature and the gaussian curvature. All discussions therefore base on these moduli. The domain sizes of microemulsions reach from ten to thousands of nanometers [5,6]. Furthermore, microemulsions are interesting for their large variety of phases. Microemulsions are by definition thermodynamically stable contrary to emulsions.

The polymer boosting effect was introduced by H. Endo, B. Jakobs and co-workers [1,2] on bicontinuous microemulsions. Bicontinuous microemulsions form when equal amounts of water and oil are used as well as a surfactant with zero preferred curvature. Then, the surfactant efficiency is defined by the minimum amount of surfactant needed to form a one phase microemulsion. It was shown that small amounts of amphiphilic diblock copolymer (10% per total amphiphile or 0.4% per total volume [2]) increase the efficiency by more than 3 times. By small angle

neutron scattering experiments it has been shown, that the amphiphilic block copolymers are anchored in the surfactant layer and that the bending rigidity (κ) is increased by the polymer. A more rigid film allows for larger structures, which needs less surface.

In this study we want to connect the macroscopic behaviour and the mesoscopic structure of microemulsions. We therefore observed phase diagrams by visual turbidity measurements. In the case of bicontinuous microemulsions, the minimum amount of surfactant is the crucial parameter for the efficiency of the surfactant. This number is also connected with the gaussian bending modulus $\bar{\kappa}$, and can therefore compared with theory. In the case of droplet microemulsions, we took the maximum oil content at a given amount of surfactant as a measure for efficiency.

Small angle neutron scattering (SANS) is involved to observe the mesoscopic structure of the microemulsion. For the bicontinuous microemulsion, the scattering data can be described by the Teubner-Strey formula [7], which yields the two structural parameters: the domain size d and the correlation length ξ . By the gaussian random field model these two parameters are connected with the bending rigidity κ , which can be compared with theories. For the droplet microemulsions, the scattering data tell about the shape and size of the droplets. Scattering models were developed to describe the scattering curves and to extract the essential structural parameters. By using different neutron contrasts, we were able to focus on specific parts of the structure.

For curiosity and for possible applications with tunable viscosity, the complementary effect of homopolymers is interesting. We restrict our studies to the simultaneous addition of two homopolymers, which directly correspond to the two blocks of the respective diblock copolymer. One of which is water soluble, and the other one dissolves in oil. Thus, the system remains still symmetric. Phase diagram measurements (indirect measure of $\bar{\kappa}$) and SANS measurements (for κ) are compared. A theory of Eisenriegler [8] predicts a decrease of κ and an increase of $\bar{\kappa}$, which means a decrease of the surfactant efficiency. In a second step, homopolymers and diblock copolymers are added simultaneously. Phase boundary measurements and SANS measurements allow to check if the opposite effects of polymer additions superpose. A possible superposition would allow for a constant efficiency with increased viscosity.

Many applications involve only small amounts of oil (or water). In this region of the phase diagram a droplet microemulsion forms. The aim of this part is to transfer the polymer boosting effect to this morphology. We studied different diblock copolymers with different molecular weights and different chain length ratios, to chose the best polymer as an efficiency booster. The efficiency was determined by phase diagram measurements. By SANS measurements the droplet

size and shape was determined. Finally, we could draw some connections between the microscopic structure and the macroscopic behaviour.

Chapter 2

Thermodynamics of microemulsions

2.1 From membrane properties to the bicontinuous microemulsion

2.1.1 Curvature energy

In the oil-water-surfactant microemulsion the surfactant forms a monolayer-membrane separating oil and water. The modeling of physical properties of this system was done by using the interface or membrane model which is assumed to determine the properties of the system. This model is valid in conditions of length and energy scales separation, insolubility of oil and water and fluidity of the membrane. The membrane is considered as a closed two dimensional surface, embedded in three-dimensional space. Locally, such surface is described by two radii of curvature R_1 and R_2 (see fig. 2.1). They can also have different signs as shown in the figure. Usually two curvatures are introduced:

$$2H = c_1 + c_2 = \frac{1}{R_1} + \frac{1}{R_2} \quad \text{mean curvature} \quad (2.1)$$
$$K = c_1 c_2 = \frac{1}{R_1} \frac{1}{R_2} \quad \text{Gaussian curvature}$$

The spontaneous curvature model for the elastic energy of the membrane was introduced by Helfrich [4]. It is based on the assumption that the local free

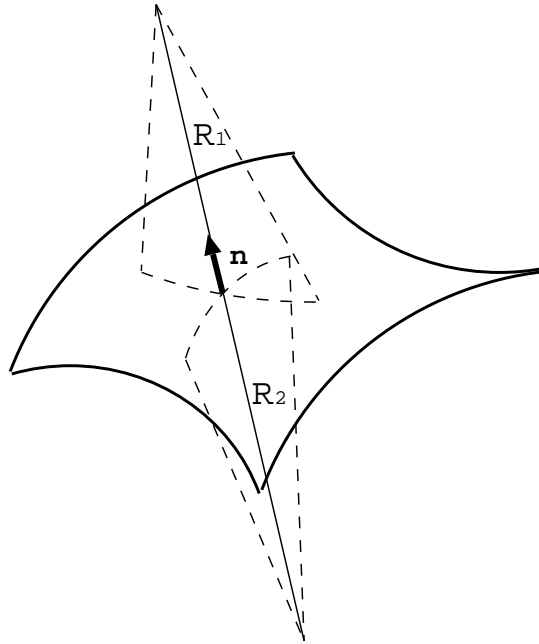


Figure 2.1: *The two principal radii of the curvature, R_1 and R_2 at a point on the surface.*

energy of membrane bending can be expanded in powers of H and K . The form of the curvature energy is given by the Hamiltonian

$$F = \int dS [\gamma + 2\kappa(H - c_0)^2 + \bar{\kappa}K + \dots] \quad (2.2)$$

where $\gamma, \kappa, \bar{\kappa}$ are the elastic constants of the membrane which depend on the structure and interactions of the membrane molecules. The first term is proportional to the area of the membrane; so the physical meaning of γ is a surface tension. The second term presents the difference between mean curvature H and spontaneous curvature c_0 . The spontaneous curvature reflects a possible asymmetry of the membrane. The elastic constant κ is the bending rigidity. The last part corresponds to the topology of the membrane and $\bar{\kappa}$ is the saddle-splay modulus. According to the Gauss-Bonnet theorem the integral over the Gaussian curvature K of a connected membrane is a topological invariant given by $4\pi(1 - g)$ where g is the genus (the number of holes or handles of the membrane). It is easy to perform the simple analysis of stability and preferred shape of membrane based on the curvature energy [3]. In the case of $c_0 = 0$ the membrane energy can be

rewritten in the following form:

$$F = \int dS \left[\frac{k_+}{2} (c_1 + c_2)^2 + \frac{k_-}{2} (c_1 - c_2)^2 \right] \quad (2.3)$$

where $k_+ = \kappa + \bar{\kappa}/2$, $k_- = -\bar{\kappa}/2$. For this form of the bending energy, the condition $k_+ > 0, k_- > 0$ should be satisfied in order to have an energy minimum at finite values of curvatures c_1 and c_2 . The upper condition is equivalent to $-2\kappa < \bar{\kappa} < 0$ in terms of $\kappa, \bar{\kappa}$. If both values k_+ , and k_- are finite and positive, the curvatures tend to $c_1 \rightarrow 0$ and $c_2 \rightarrow 0$. Such curvatures describe a lamellar structure. When $k_+ \rightarrow 0$ is small, then the energy minimum tends to satisfy the conditions $(c_1 - c_2)^2 \rightarrow 0$ and $(c_1 + c_2)^2$ can be very large. This means that the membrane tends to form a spherical shape: $c_1 \approx c_2$. For the opposite case $k_- \rightarrow 0$, then it should be $(c_1 + c_2)^2 \rightarrow 0$ and $(c_1 - c_2)^2$ can be very large. That corresponds to $c_1 \approx -c_2$ (see Fig. 2.1). This type of curvature is characteristic for the class of minimal surfaces.

A very important property of the membrane curvature energy F is that it is scale invariant, i.e. the membrane curvature energy F does not depend on its size. So in order to explain the transition between mesophases with different geometry, thermal excitations should be taken into account.

The effect of thermal fluctuations at small scales (compared to the domain size) decreases the rigidity of membrane at the large scales as follows from renormalization group calculations [9, 10] and leads to the expressions for renormalized rigidities:

$$\kappa_R(\lambda) = \kappa - \alpha \frac{k_B T}{4\pi} \ln(\lambda/a) \quad (2.4)$$

$$\bar{\kappa}_R(\lambda) = \bar{\kappa} - \bar{\alpha} \frac{k_B T}{4\pi} \ln(\lambda/a) \quad (2.5)$$

where $\alpha = 3$ and $\bar{\alpha} = -10/3$. a is a microscopic cutoff (e.g. size of molecules). A cutoff for λ is determined by the average separation of neighboring membranes and is connected to the membrane volume fraction $\Psi \equiv aS/V = a/\lambda$. For the k_{\pm} , it was obtained $k_{\pm}^R(\lambda) = k_{\pm} - \alpha_{\pm} \frac{k_B T}{4\pi} \ln(\lambda/a)$ with $\alpha_+ = \alpha + \bar{\alpha}/2 = 4/3$, and $\alpha_- = -\bar{\alpha}/2 = 5/3$.

The instabilities of the lamellar phase start to appear at $k_{\pm}^R(\lambda) \rightarrow 0$ when the effect of thermal fluctuations is included. At the line of phase instability, the

following equation [11] should be valid:

$$\ln(\Psi/\Psi_0) = -\frac{4\pi}{\alpha_{\pm}} \frac{k_{\pm}}{k_B T} \quad (2.6)$$

This equation expresses the connection between microscopic properties of microemulsions (bending moduli $\kappa, \bar{\kappa}$) and its macroscopic properties (surfactant content Ψ). Ψ_0 can differ from 1 due to deviations in the cutoff. However, Ψ_0 is a microscopic number.

2.1.2 Gaussian Random Field approximation

For the modeling of the bicontinuous phase, the phenomenological approach called Gaussian Random Field approximation is used [12, 13]. In this case, amounts of oil and water are approximately equal and separated in two subspaces by a surfactant film. The membrane is modeled as a level surface of the scalar field $h(\vec{r}) = \alpha$, where $\vec{r} \in \mathbb{R}^3$ and $-\infty < \alpha < \infty$. Within the GRF model the statistics of the scalar field are defined by the quadratic Hamiltonian

$$\mathcal{H}_0 = \frac{1}{2} \int d\vec{r} h(\vec{r}) w(\vec{r} - \vec{r}') h(\vec{r}')$$

Here $w(\vec{r} - \vec{r}')$ is the coupling or the two body interaction. Thermal fluctuations of the scalar field are calculated with the Boltzman weight $e^{\mathcal{H}_0}$. The coupling should decay fast enough with the argument $(\vec{r} - \vec{r}')$ to make the integral, second and fourth moments finite. Two normalization conditions $\langle h(\vec{r}) \rangle = 0$, $\langle h^2(\vec{r}) \rangle = 1$ are included. The practical use of the GRF model is that it is possible to calculate averaged geometrical characteristics of the level surfaces (i.e curvatures $\langle H \rangle$, $\langle K \rangle$) analytically [14]. At this stage, the GRF gives just a qualitative description of the fluctuating membrane ensemble. It is necessary to define analytical expressions for the function $w(\vec{r} - \vec{r}')$ or its Fourier transformation $w(\vec{q})$. The result was obtained with the implementation of the variational approach method [15, 16]. The idea is based on the following consideration: For the full system with hamiltonian H and free energy F , and the reference system with hamiltonian H_0 and free energy F_0 the Gibbs-Bogoliubov-Feynman inequality [17] is valid:

$$F \leq F_0 + \langle H - H_0 \rangle_0 \quad (2.7)$$

To obtain the lowest upper boundary of F (see eq. 2.7) a parameterized reference system is used. An optimal spectral density $1/w(\vec{q})$ is then obtained. As

calculated in [15, 16], this leads to the Teubner-Strey formula (see eq. 2.29).

$$G(q) = \frac{1}{w(q)} = \frac{a}{q^4 - bq^2 + c} \quad (2.8)$$

The coefficients a, b, c are functions of the bending rigidity κ and surface-to-volume ratio S/V of the system. They are not dependent on the saddle splay modulus $\bar{\kappa}$ [15, 16].

A Fourier transform of equation 2.8 gives the correlation function:

$$\int \frac{d^2q}{(2\pi)^2} G(q) e^{-i\vec{q}\vec{r}} = \frac{1}{k_0 r} e^{-r/\xi} \sin k_0 r$$

where $k_0 = \frac{1}{2}(2\sqrt{c} - b)^{1/2}$ is the characteristic wave vector ($2\pi/k_0 = d$ - the domain size), and $\xi = 2(2\sqrt{c} + b)^{-1/2}$ is the correlation length. The correlation function is normalized to be unity for small r . This provides the direct connection between experimental values and microscopic parameters. The connection between k_0 , ξ and κ is given by [2]:

$$k_0 \xi = \frac{64}{5\sqrt{3}} \frac{\kappa}{k_B T} \Theta \left(\frac{\kappa}{k_B T}, a \frac{S}{V} \right) \underset{\kappa \rightarrow \infty}{=} \frac{64}{5\sqrt{3}} \frac{\kappa}{k_B T} \quad (2.9)$$

The asymptotic dependencies, when $\kappa/k_B T$ is large, read [3]:

$$1/d \sim S/V \quad (2.10)$$

$$\xi \sim \kappa (S/V)^{-1} \quad (2.11)$$

$$\xi/d \sim \kappa \quad (2.12)$$

That is a very suitable form to check theory predictions with experimental results.

2.1.3 Diblock copolymer addition

Let us consider the effect, which is caused by the addition of amphiphilic diblock copolymer to the microemulsion. The polymer is anchored in the surfactant surface with the hydrophilic block in water and the hydrophobic block in oil, correspondingly. Both anchored blocks are effectively repelled from the membrane surface. Two cases should be distinguished: One case is called “brush regime” at high polymer density on the membrane. Another is called “mushroom regime” at lower densities. The overlap polymer concentration appears, when the average distance between two anchored polymers is equal to the averaged end-to-end distance of the polymer block in oil or water ($\sigma R_{ee}^2 = 1$). The amount of diblock copolymer was below the overlap concentration in our experiments; so we will consider only the mushroom regime. Qualitatively, the effect of diblock copolymer anchoring can be understood in terms of the entropy [3]. When the polymers are homogeneously tethered to the membrane surface, both the membrane surface and the neighboring polymers restrict the number of configurations which are accessible to the polymer. This should cause entropic repulsion suppressing the membrane fluctuations. Furthermore, diblock copolymers make saddle shape surface deformations unfavorable. The simple explanation of this effect was proposed in [18]. There, a thin shell with volume V and height h above a surface of area A is considered. The ratio of the volume V available for chains in a layer of height h and grafting area A in bend geometries is expanded as:

$$\frac{V}{Ah} = 1 + \frac{1}{2}(c_1 + c_2) + \frac{1}{3}c_1c_2 \quad (2.13)$$

where c_1 and c_2 are local curvatures of the surface. Then, for the saddle shape surface $c_1 = -c_2 = hc$ one obtains $V/Ah = 1 - \frac{1}{3}(hc)^2$. So when the local curvature of the surface is increased, there is less space for the monomers than for the unbent shell and chains must stretch upon bending. Those tethered diblock copolymers should increase the absolute values of the bending rigidity κ and the saddle splay modulus ($\bar{\kappa}$). The analytical expressions for the bending modulus were calculated for the polymer decorated membrane in [19] (see also Appendix B).

$$\kappa_{eff} = \kappa + k_B T \frac{1 + \pi/2}{12} \sigma (R_O^2 + R_W^2) \quad (2.14)$$

$$\bar{\kappa}_{eff} = \bar{\kappa} - k_B T \frac{1}{6} \sigma (R_O^2 + R_W^2) \quad (2.15)$$

R_O and R_W are the end-to-end distances of the respective oil and water soluble blocks. From these equations it is seen that the influence of diblock decoration is

quite weak (of the order of $k_B T$). Why it is so pronounced for the macroscopic properties of the microemulsion follows from the expression connecting the membrane content at the emulsification boundary with the bending modulus (see eq. 2.6). In combination with equation 2.15 it gives:

$$\ln(\Psi/\Psi_0) = -\frac{\pi}{3\alpha_-} \sigma(R_o^2 + R_w^2) \quad (2.16)$$

So the membrane content at the emulsification boundary is an exponential function of $\bar{\kappa}$. Even small changes in κ cause a visible macroscopic effect. That was already tested experimentally [2, 20].

2.1.4 Homopolymer addition

The influence of the homopolymer addition on the membrane properties is predicted by different authors [19, 21, 8]. The change of the bending moduli with additions of short polymer chains will be [8]:

$$\frac{\Delta\kappa}{k_B T} \approx -n_p \frac{R_{ee}^3}{D^{3/2}} 0.133(1 - 0.0713\varepsilon) + O(\varepsilon^2) \quad (2.17)$$

$$\frac{\Delta\bar{\kappa}}{k_B T} \approx n_p \frac{R_{ee}^3}{D^{3/2}} 0.133(1 - 0.177\varepsilon) + O(\varepsilon^2) \quad (2.18)$$

Here n_p is the polymer number density, D is the dimension of the space containing polymers and $\varepsilon = 4 - D$. So for our case $D = 3$ and $\varepsilon = 1$. It was assumed that the chains stay in the solvent (in oil or water) and are repelled by the surface. The final equation reads:

$$\frac{\Delta\kappa}{k_B T} = -0.0238 \frac{\phi_p}{V_p} (R_O^3 + R_W^3) \quad (2.19)$$

$$\frac{\Delta\bar{\kappa}}{k_B T} = 0.0211 \frac{\phi_p}{V_p} (R_O^3 + R_W^3) \quad (2.20)$$

R_O and R_W are the end-to-end distances of added polymers, ϕ_p is volume fraction of the polymer in the system and V_p is the monomer volume times the degree of polymerization N . In this equation we accounted for the effect of two different homopolymers which are located at different membrane sides.

2.1.5 Addition of homopolymer and diblock copolymer

For the renormalized bending rigidity of a membrane with addition of diblock copolymer and homopolymers we summed over all effects discussed above:

$$\begin{aligned}
 \frac{\kappa_R}{k_B T} &= \frac{\kappa_0}{k_B T} && \text{pure membrane} && (2.21) \\
 &+ \frac{\alpha}{4\pi} \ln(\psi) && \text{thermal fluctuations} && \\
 &+ \frac{1}{12} \left(1 + \frac{\pi}{2}\right) \sigma (R_W^2 + R_O^2) && \text{diblock copolymer} && \\
 &- 0.0238 \frac{\phi_p (R_W^3 + R_O^3)}{V} && \text{homopolymer} &&
 \end{aligned}$$

where $\alpha = 3$, σ is the grafting polymer density, R_W and R_O are the mean squared end to end distance of the polymer in water and oil respectively. And analogously for the saddle-splay modulus as

$$\begin{aligned}
 \frac{\bar{\kappa}_R}{k_B T} &= \frac{\bar{\kappa}_0}{k_B T} + \frac{\bar{\alpha}}{4\pi} \ln(\psi) && (2.22) \\
 &- \frac{1}{6} \sigma (R_W^2 + R_O^2) + 0.0211 \frac{\phi_p (R_W^3 + R_O^3)}{V}
 \end{aligned}$$

where $\bar{\alpha} = -10/3$. For these general expressions of κ_R , $\bar{\kappa}_R$ we assumed a superposition over all effects of diblock and homopolymer additions. This assumption should be tested by our experiments.

2.1.6 Ginzburg-Landau model for the scattering intensity

The scattering function for the bicontinuous microemulsion in the bulk contrast was constructed by Teubner and Strey in [7] on the basis of the Ginzburg-Landau theory for the critical point. The origin of this model based on the phenomenological Landau free energy approach with the appropriate symmetry. For this purpose, the appropriate choice of the order-parameter is done. This order-parameter is defined on mesoscopic length scales, which is large compared to microscopic scales, but small compared to macroscopic scales. Then, the Landau free energy is approximated by the expansion in powers of the order-parameter. Only first few terms of the expansion are necessary for the description of the problem. The order-parameter ψ in the case of microemulsions was connected

with the water-to-oil ratio. And the simplest free energy functional appropriate for the description is:

$$F\{\psi\} = \int d\vec{r}[a_0\psi^2 + a_1(\vec{\nabla}\psi)^2 + a_2(\Delta\psi)^2] \quad (2.23)$$

with conditions $a_0 > 0$, $a_1 < 0$, necessary for existence of interface and $a_2 > 0$, $4a_0a_2 - a_1^2 > 0$ for the stability of the system. This functional gives the scattering intensity distribution like

$$\frac{d\Sigma}{d\Omega}(Q) \sim \frac{1}{a_0 + a_1Q^2 + a_2Q^4} \quad (2.24)$$

This function has a single broad maximum for $a_1 < 0$ and a decay $\sim Q^{-4}$. The two points correlation function can be obtained from 2.24.

$$\langle\psi(\vec{r}_1)\psi(\vec{r}_2)\rangle = \int d\vec{Q}e^{-i\vec{Q}(\vec{r}_2-\vec{r}_1)}S(\vec{Q}) = G(|\vec{r}_2 - \vec{r}_1|) \quad (2.25)$$

if spherical symmetry is assumed. It is $\langle\psi(\vec{r}_1)\psi(\vec{r}_1)\rangle = 1$. The correlation function is then:

$$G(r) = 4\pi \int_0^\infty dQ Q^2 \frac{\sin(Qr)}{Qr} S(Q) \quad (2.26)$$

and so

$$G(r) = \frac{1}{k_0 r} e^{-r/\xi} \sin(k_0 r) \quad (2.27)$$

where ξ is the correlation length and $k_0 = 2\pi/d$ gives the periodicity in arrangement of oil and water domains. To obtain the proportionality constant in 2.24 from 2.27, we arrived at

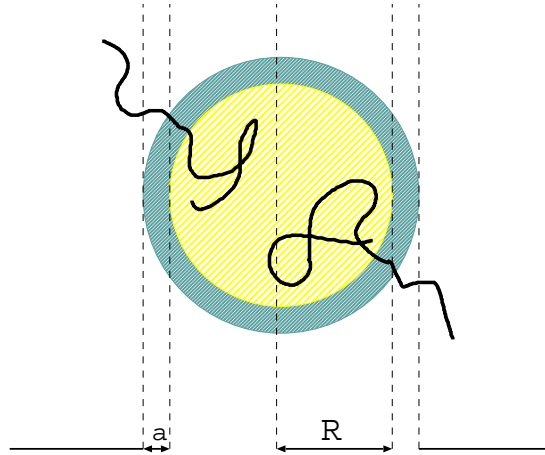
$$\frac{d\Sigma}{d\Omega}(Q) = \langle\nu^2\rangle 4\pi \int_0^\infty dr r^2 \frac{\sin(Qr)}{Qr} G(r) \quad (2.28)$$

where $\langle\nu^2\rangle \equiv \langle(\rho - \bar{\rho})^2\rangle$ is the mean square scattering length density fluctuation. It can be approximated $\langle\nu^2\rangle = \phi_o\phi_w\Delta\rho^2$. ϕ_o, ϕ_w are volume fractions of oil and

water. $\Delta\rho$ is the difference of scattering length densities of oil and water, which is the neutron constant. Finally we obtain:

$$\frac{d\Sigma}{d\Omega}(Q) = \frac{8\pi\langle\nu^2\rangle/\xi}{Q^4 - 2(k_0^2 - \xi^{-2})Q^2 + (k_0^2 + \xi^{-2})^4} \quad (2.29)$$

The function 2.29 has a peak at $Q = (k_0^2 - \xi^{-2})^{1/2}$.

Figure 2.2: *Schematic droplet representation.*

2.2 Theory of droplet microemulsions

2.2.1 General part

One observes a wide variety of thermodynamically stable phases by changing the content of different components and the temperature of the system. In particular droplet-type structures have been treated in much detail [22, 23, 24, 25, 26]. This comprises droplet phases of water droplets in oil (w/o microemulsion or L_2 phase) or oil droplets in water (o/w or L_1 phase), both surrounded by a monomolecular surfactant layer. We finally aim at oil in water droplets with small additions of diblock copolymer (see fig. 2.2). At Fig.2.3, typical phase diagrams are presented: the phase triangle and temperature/concentration diagram for the oil in water microemulsion. The grey line shows phase curves of the system at different phase diagrams when the oil concentration increases.

The free energy of the droplet phase microemulsion, neglecting interfacial tension, consists of two parts. One part F_{curv} is the Helfrich's free energy. It describes the curvature free energy of the interfacial surfactant layer that separates the oil and the water phases. The second part is the entropy contribution F_{ent} .

$$F = F_{curv} + F_{ent} \quad (2.30)$$

The curvature part of the free energy has the standard form:

$$F_{curv} = \frac{1}{2}\kappa \int dS (c_1 + c_2 - 2c_0)^2 + \bar{\kappa} \int c_1 c_2 dS \quad (2.31)$$

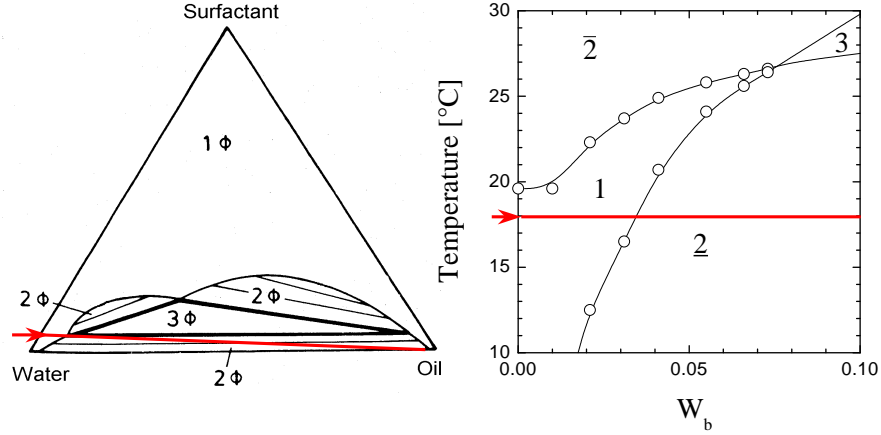


Figure 2.3: *On the left : phase triangle. 1ϕ indicates the one phase region, 2ϕ indicates 2-phase region and 3ϕ the three phase region. On the right: typical phase diagram temperature versus oil content W_b for the droplet phase microemulsion. 1 indicates the one phase region. $\underline{2}$ the 2 phase region with excess oil; $\bar{2}$ the 2 phase region with excess water (this phase appears for higher temperatures in the phase triangle) and 3 the three phase coexistence.*

where integration is over the droplet surface. Just using the membrane curvature part F_{curv} it is possible to obtain a qualitative picture of the global features of a microemulsion phase diagram. To obtain more close correspondence between the experiment and theoretical predictions, some additional effects should be included. That is entropy and polydispersity effects. The most general form of the translation entropy can be written as

$$F_{ent} = Nk_B T f(\phi) \quad (2.32)$$

Here N is the number of droplet aggregates in the system, ϕ is the volume fraction of the droplets. The function f depends only on the volume fraction of droplets. This means no other interaction between droplets except steric exclusion. Different forms of this function were proposed based on different models of mixing. In paper [27] some of such functions were analyzed. For the system with low droplet volume fraction, the most consistent result was obtained with the Flory-Huggins

entropy of mixing used by [24]:

$$f(\phi) = \frac{1}{\phi}(\phi \ln(\phi) + \dots) \quad (2.33)$$

For future considerations two constraints are considered. Because we have a one phase system and the surfactant molecules are supposed to form a monolayer between internal (oil) and external (water) phases, the total volume V_{int} of droplets and total surface of the interface S are constants.

2.2.2 Fluctuations of spherical droplets.

Droplets with spherical shape were studied widely by [23, 24]. For the spherical droplets with curvature $c_1 = c_2 = c_s$, the free energy normalized to the surface S reads

$$F/S = 2\kappa(c_s - 2c_0)^2 + \bar{\kappa}c_s^2 + \frac{k_B T}{4\pi}c_s^2 f(\phi) \quad (2.34)$$

When the maximum amount of oil is reached (surfactant solubilization capacity), the addition of oil causes an excess oil phase. It is easy to obtain the maximum droplet radius $1/c_m$ by minimization of the total free energy (eq. 2.34) as

$$\frac{c_0}{c_m} = \frac{\bar{\kappa} + 2\kappa}{2\kappa} + \frac{k_B T}{8\pi\kappa} f(\phi) \quad (2.35)$$

A next step of the theory would account for the thermal fluctuations of the droplets [23]. The fluctuating shape of a quasi-spherical droplet can be parameterized by

$$R(\theta, \phi) = R_0 \left(1 + \sum_{l \geq 0} \sum_{m=-l}^l u_{l,m} Y_{lm}(\theta, \phi) \right) \quad (2.36)$$

where $u_{l,m}$ are the fluctuation amplitudes, with indices $|m| \leq l$. For real fluctuations: $u_{l,-m} = (-1)^m u_{l,m}^*$ and Y_{lm} are the spherical harmonic modes. The mean square amplitude [23] characterizes the fluctuations of the shape and size of a droplet:

$$\langle |u_{l,m}|^2 \rangle = \frac{k_B T}{(l+2)(l-1) [(l(l+1) - 6 + 4Rc_0)\kappa - 3\bar{\kappa} - 3Tf(\phi)/(4\pi)]} \quad (2.37)$$

The right part of equation 2.37 is independent on m , which is due to the equipartition theorem [28]. It has been shown in [23, 24] that the main contribution to the fluctuations comes from first two modes $\langle |u_{00}|^2 \rangle$ and $\langle |u_{2m}|^2 \rangle$. The mode $\langle |u_{00}|^2 \rangle$ corresponds to the frustration of the mean droplet radius i.e. polydispersity. Translations ($\langle |u_{1m}|^2 \rangle$) would be described by a diffusion model, and are not considered here. The modes $\langle |u_{2m}|^2 \rangle$ correspond to the most important droplet shape fluctuations, i.e. the peanutlike deformations. The negative value of $\bar{\kappa}$ increases the $l = 0$ mode and decreases modes with $l \geq 2$ [22]. The physical origin is that $\bar{\kappa}$ couples to the number of droplets in the system (from Gauss-Bonnet theorem) and a negative value of $\bar{\kappa}$ tends to increase the number of droplets in the system or the polydispersity. Polydispersity is affected due to restrictions of oil and surfactant amounts. The observed polydispersity is just determined by the $\langle |u_{00}|^2 \rangle$ as stated in [22]:

$$\epsilon = (\langle |u_{00}|^2 \rangle / (4\pi))^{1/2} \quad (2.38)$$

Another way to access the connection between the bending modulus and experimental parameters is to use the result from [24]. Considering the bending energy of droplet shapes as a function of modes u_{2m} , the minimal energy was shown to have a shape of prolate ellipsoid of revolution. That is the case when $u_{2m} \neq 0$ only for one m . Choosing the solution with the mode $|u_{20}|^2 \neq 0$ only, we obtain for the average droplet shape:

$$\begin{aligned} R(\theta, \phi) &= R_0 \left(1 + \sqrt{\langle |u_{00}|^2 \rangle} Y_{00}(\theta, \phi) + \sqrt{\langle |u_{20}|^2 \rangle} Y_{20}(\theta, \phi) \right) \\ &= R_0 \left(1 + \frac{\sqrt{\langle |u_{00}|^2 \rangle}}{2\pi} + \frac{\sqrt{\langle |u_{20}|^2 \rangle}}{\sqrt{16\pi}} 5\sqrt{5}(3 \cos^2 \theta - 1) \right) \end{aligned} \quad (2.39)$$

Implementing this result to the ellipsoid with the average axis ratio $\epsilon = R(0)/R(\pi/2)$, we obtain:

$$\epsilon = \frac{1 + \sqrt{\pi} \sqrt{\langle |u_{00}|^2 \rangle} / 2 + 10\sqrt{5\pi} \sqrt{\pi} \sqrt{\langle |u_{20}|^2 \rangle} / 4}{1 + \sqrt{\pi} \sqrt{\langle |u_{00}|^2 \rangle} / 2 - 5\sqrt{5\pi} \sqrt{\pi} \sqrt{\langle |u_{20}|^2 \rangle} / 4} \quad (2.40)$$

This gives the way to solve for modes $\langle |u_{00}|^2 \rangle$ and $\langle |u_{20}|^2 \rangle$ in terms of polydispersity ϵ and axis ratio ϵ (combination of 2.38, 2.40). But from the result [24] it is possible to express modes $\langle |u_{00}|^2 \rangle$ and $\langle |u_{20}|^2 \rangle$ as a function of bending constants

κ , $\bar{\kappa}$ as shown in 2.37. Substituting the spontaneous curvature from expression 2.35 into 2.37, we obtain:

$$\langle |u_{00}|^2 \rangle = \frac{k_B T}{(2\kappa + \bar{\kappa} + k_B T f(\phi)/(4\pi))(6 - 4Rc_0)} \quad (2.41)$$

and

$$\langle |u_{20}|^2 \rangle = \frac{k_B T}{16\kappa R c_0 + (3 - 2Rc_0)(4\bar{\kappa} + k_B T f(\phi)/\pi)} \quad (2.42)$$

When the experimental situation is very close to the emulsification boundary, then $R \rightarrow 1/c_m$ and we can obtain the spontaneous curvature from 2.35. Putting this to equations 2.41, 2.42, with the condition that the product Rc_m is close to 1 near the emulsification boundary, we obtain:

$$\langle |u_{00}|^2 \rangle = \frac{k_B T}{2(2\kappa + \bar{\kappa}) + 0.5k_B T f(\phi)/\pi} \quad (2.43)$$

$$\langle |u_{20}|^2 \rangle = \frac{k_B T}{4(4\kappa - \bar{\kappa}) - k_B T f(\phi)/\pi} \quad (2.44)$$

From these equations it is possible to express the bending moduli of the droplet surface by measuring the polydispersity ϵ and shape fluctuations ε . From equation 2.44 one expects less shape fluctuations with increasing κ .

2.2.3 Droplet to cylinder phase transition

Since we observed in our experiments a cylindrical droplet structure, it is necessary to give an overview of theoretical considerations for the formation of cylindrical structures and of the sphere to cylinder transition. The first work has been done by Safran [29]. In his model, for the free energy the Helfrich curvature energy was considered only. The entropy of mixing was neglected.

Suppose that we have oil droplets in water and the surfactant head group (which is approximately half volume of surfactant molecule) belongs to the globule. Indicating the number density of monodisperse globules by n , one obtains for the surface and volume of the droplets by the incompressibility conditions:

$$nA\delta = \phi_s; \quad nV = \phi_o + \phi_s/2 \quad (2.45)$$

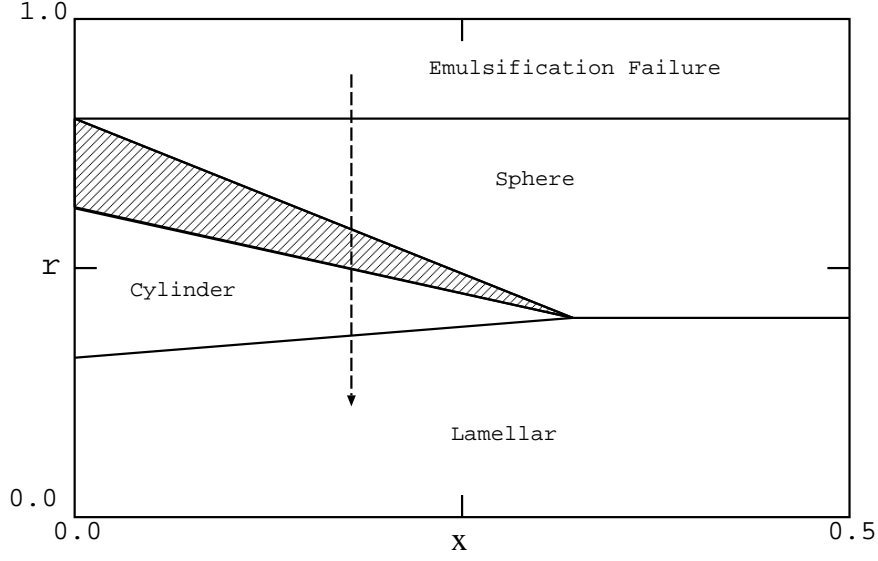


Figure 2.4: *Regions of stability of different phases of a microemulsion as functions of $x = -(1 + 2\kappa/\bar{\kappa})^{-1}$ and normalized radius $r = c_0 R_s = c_0 3\delta \frac{\phi_o + \phi_s/2}{\phi_s}$. The dashed region indicates the coexistence of spheres and cylinders. The dashed arrow is a trajectory of our system at constant composition with increasing of temperature.*

where δ is the thickness of the surfactant layer and ϕ_o , ϕ_s are volume fractions of oil and surfactant in the sample.

For the N_s spheres with radius R_s , we obtain for the free energy (eq. 2.31) neglecting the term to the second order in spontaneous curvature.

$$F_s = N_s \pi \kappa (4(2 + \bar{\kappa}/\kappa) - 16R_s/R_0) \quad (2.46)$$

with conditions of conservation of volume $V_s = N_s \frac{4}{3} \pi R_s^3$, and surface $A_s = N_s 4\pi R_s^2$. The mean radius is given by $R_0 = 1/c_0$. For the cylinder, whose length L is large compared to the radius R_c (curvature energy of the end cups is neglected), we write

$$F_c = N_s \pi L \kappa (1/R_c - 4/R_0) \quad (2.47)$$

with the volume $V_c = N_c \pi R_c^2 L$, and surface $A_c = N_c 2\pi R_c L$. If the system consists of a mixture of spheres and cylinders, than we obtain using the volume fractions

of spheres $\psi_s = N_s 4/3\pi R_s^3/V$ and cylinders $\psi_c = N_c 4\pi R_c^3/V$

$$F_{sc}/V = \psi_s \kappa [3(2 + \bar{\kappa}/\kappa)/R_s^3 - 12/(R_0 R_s^2)] + \psi_c \kappa [1/R_c^3 - 4/(R_0 R_c^2)] \quad (2.48)$$

with volume and area constraints

$$\psi_s + \psi_c = 1 \quad (2.49)$$

and

$$\frac{A}{V} = \frac{3\psi_s}{R_s} + \frac{2\psi_c}{R_c} = \frac{1}{d} \frac{\phi_s}{\phi_o + \phi_s/2} \equiv \frac{1}{\omega} \quad (2.50)$$

These conditions give immediately the sphere radius for the case of pure spheres ($\psi_s = 1$)

$$R_s = 3d \frac{\phi_o + \phi_s/2}{\phi_s} \quad (2.51)$$

For the case of pure cylinders ($\psi_c = 1$), we obtain the cylinder radius:

$$R_c = 2d \frac{\phi_o + \phi_s/2}{\phi_s} \quad (2.52)$$

The free energies for these cases will be

$$\frac{\omega^3 F_s}{\kappa V} = \frac{(2 + \bar{\kappa}/\kappa)}{9} - \frac{4}{3R_0} \quad (2.53)$$

and

$$\frac{\omega^3 F_c}{\kappa V} = \frac{1}{8} - \frac{1}{R_0} \quad (2.54)$$

In order to find the phase boundaries between the region with a mixture of spheres and cylinders and the regions with pure spheres and pure cylinders, the free energy F_{sc} is minimized with respect to the radii ($\partial F_{sc}/\partial R_s = 0$, $\partial F_{sc}/\partial R_c = 0$) and the radii R_s , R_c are represented in terms of $\bar{\kappa}/\kappa$ and R_0 . For large values of R_0 , the system forms planar sheets of surfactant films (lamellar phase). The transition to the lamellar phase is determined by zero curvature energy ($F_{sc} = 0$) in 2.48. With all free energies (pure cylinders, pure droplets, and mixed case), one obtains the phase boundaries by minimization.

The addition of more oil causes an emulsification failure, i.e. the one phase droplet microemulsion with optimal droplet radius coexists with an excess oil phase (emulsification failure). The emulsification failure yields the constraint equation $\psi_s + \psi_c + \psi_o = 1$ according for the presence of an excess phase, where ψ_o is the volume fraction of the excess phase. The minimization of the free energy ($\partial F_{sc}/\partial \psi_o = 0$) with the condition that $\psi_o = 0$ at emulsification failure gives the solubilization limit for the phases of spheres, cylinders and spheres+cylinders. The phase diagram for these transitions is represented in Fig.2.4 as obtained by [29].

This consideration gives a large variety of shapes even without accounting for thermal undulations. For the measurement of samples with constant composition but at different temperatures it is known that the bending rigidity and saddle splay modulus are approximately constant within the considered temperature range. But the spontaneous curvature is a linear function of the temperature $c_0 \sim (T - \bar{T})$. Here \bar{T} is the so called inversion temperature. So an increase of temperature could cause a change of the domain shape in the direction indicated by the dashed line in Fig.2.4. The dashed region of the figure corresponds to the area of coexistence of spheres and cylinders.

So even for very simple assumptions one obtains a qualitative picture. In later works by Safran [30] the entropy of mixing was included, and a closed-loop coexistence region in the mixture of spheres and cylinders was obtained.

Further development of the theory was done in [31] where in addition to the entropy of mixing the radial polydispersity of cylinders and droplets and the cylinder length polydispersity was included. An important consequence of the translation entropy is that the transition from spheres to cylinders is washed out. So at any finite temperature, the amount of spheres and cylinders is determined by the Boltzman distribution. Regions with neat spheres or neat cylinders are prohibited. This enhanced model still contains simplifications like neglecting interactions between aggregates, and the mean-field character.

2.2.4 Addition of diblock copolymer

When the surface of the droplet is grafted by the diblock copolymer as shown in the picture 2.2, there can occur different situations depending on the curvature of the surface, polymer grafting density and length of the blocks. An overview is given by the schematic picture (fig. 2.5) taken from the work [32]. Let us consider the inner block as a grafted polymer chain consisting of N monomers. It is assumed to be linear, flexible, made of identical, neutral monomers of length a . The chain is grafted to the surface of the sphere of radius R with scaled grafting

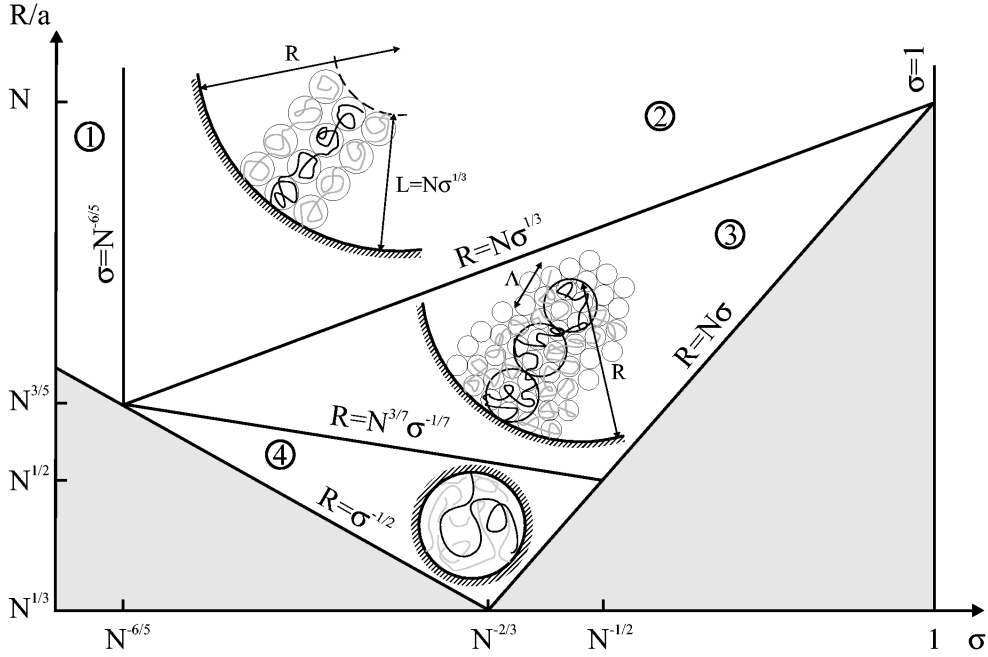


Figure 2.5: Various regimes for the polymer grafted to the concave spherical surface. Scaled radius of surface curvature vs. scaled grafting density. 1 - mushroom regime, 2 - weak concave brush, 3 - compressed brush, 4 - collapsed brush, in gray : unphysical regions

density σa^2 and repelled by the interface. Good solvent conditions are assumed, and for the Flory radius of gyration one obtains $R_F = aN^{3/5}$.

When the polymer is grafted to the concave side of the interface, there could be four physically accessible regions characterizing the polymer state. Region 1 corresponds to the case of a large sphere radius and a relatively small grafting density (mushroom regime). The interaction starts when $\sigma \approx (a/R_F)^2 = N^{-6/5}$. With increasing grafting density, the chains are stretched and the system comes to the brush regime. The height of the brush for such geometry is alike in the planar geometry $L \approx aN\sigma^{1/3}$ (case 2 in Fig.2.5). This region is limited by the condition that the grafting density cannot be bigger than one chain per squared monomer site ($\sigma A^2 \leq 1$). The curvature of the sphere becomes important when $R \simeq L$ (region 3). The region 4 corresponds to confined chains. That is the case when the radius of the sphere is equal to the natural size of the chain in semi-dilute solution ($R \simeq a\sigma^{-1/7}N^{3/7}$). The limits occur when there is not enough solvent in the sample ($R \geq aN\sigma$) or when there is only one chain per droplet ($R \geq a\sigma^{-1/2}$). Our experimental situation for a high oil content supposedly is

in the mushroom regime. For that case, it is possible to implement results of equations 2.14 and 2.15 which are valid in the case of a spherical geometry (see Appendix B).

2.3 Scattering functions of droplet microemulsions

2.3.1 Introduction

The coherent component of the macroscopic differential scattering cross section has the form

$$\frac{d\Sigma}{d\Omega}(\vec{q}) = V^{-1} \left\langle \left| \sum_{i=1}^N b_i e^{i\vec{q}\vec{r}_i} \right|^2 \right\rangle \quad (2.55)$$

b_i is the scattering length of i th nucleus and \vec{r}_i the position of this nucleus, V is the sample volume. \vec{q} is the scattering vector. If the sample contains a collection of N_p particles in homogeneous solvent and the number of nuclei in the j th particle is N_j , then the center of mass of the particle \vec{R}_j is introduced. Now the position of the nuclei i in the j th particle is $r_{ij} = R_j + r_i$. The sum in 2.55 is now:

$$\frac{d\Sigma}{d\Omega}(\vec{q}) = V^{-1} \left\langle \left| \sum_{j=1}^{N_p} e^{i\vec{q}\vec{R}_j} \sum_{i=1}^{N_j} b_{ij} e^{i\vec{q}\vec{r}_i} \right|^2 \right\rangle \quad (2.56)$$

The second sum in equation 2.56 is usually called scattering amplitude of a particle.

$$A_j(\vec{q}) = \sum_{i=1}^{N_j} b_{ij} e^{i\vec{q}\vec{r}_i} \quad (2.57)$$

So after substitution in 2.56 one obtains:

$$\frac{d\Sigma}{d\Omega}(\vec{q}) = V^{-1} \left\langle \sum_{j=1}^{N_p} \sum_{i=1}^{N_p} A_j^*(\vec{q}) A_i(\vec{q}) e^{i\vec{q}(\vec{R}_i - \vec{R}_j)} \right\rangle \quad (2.58)$$

The considered system consists of plenty of atoms which are placed on their characteristic repeat distances $\Delta r \approx 1\text{\AA}$. In the SANS Q range all pure materials

appear as a continuous medium. The scattering length density of a pure material is defined as

$$\rho_j(\vec{r}) = V_j^{-1} \sum_i b_{ij} \delta(\vec{r} - \vec{r}_i) \quad (2.59)$$

where V_j is the macroscopic particle volume. The scattering amplitude (eq. 2.57) becomes an integral

$$A_j(\vec{q}) = \int_{V_j} d\vec{r} (\rho_j(\vec{r}) - \rho_s) e^{i\vec{q}\vec{r}} + \rho_s \int d\vec{r} e^{i\vec{q}\vec{r}} = \int_{V_j} d\vec{r} \Delta\rho_j(\vec{r}) e^{i\vec{q}\vec{r}} \quad (2.60)$$

for $\vec{q} \neq 0$. ρ_s is the scattering length density of the solvent, and $\Delta\rho_j(\vec{r}) = \rho_j(\vec{r}) - \rho_s$ is the neutron contrast.

Assuming that the particle size and orientation are uncorrelated with the position of the particles,

$$\frac{d\Sigma}{d\Omega}(\vec{q}) = V^{-1} \left\langle \sum_{j=1}^{N_p} \sum_{i=1}^{N_p} \langle A^*(\vec{q})_j A(\vec{q})_i \rangle e^{i\vec{q}(\vec{R}_i - \vec{R}_j)} \right\rangle \quad (2.61)$$

where the product of $A(\vec{q})$, $A^*(\vec{q})$ is averaged over distributions of particle sizes and orientations.

$$\langle A^*(\vec{q})_j A(\vec{q})_i \rangle = (\langle |A(\vec{q})|^2 \rangle - |\langle A(\vec{q}) \rangle|^2) \delta_{ij} + |\langle A(\vec{q}) \rangle|^2 \quad (2.62)$$

Finally, for the scattering cross section we obtain

$$\frac{d\Sigma}{d\Omega}(\vec{q}) = \frac{N_p}{V} P(\vec{q}) S(\vec{q}) \quad (2.63)$$

In the equation above the form factor is introduced:

$$P(\vec{q}) = \langle |A(\vec{q})|^2 \rangle \quad (2.64)$$

which reflects the size and shape and density distribution inside a scattering particle. And the structure factor

$$S(\vec{q}) = 1 + \frac{|\langle A(\vec{q}) \rangle|^2}{\langle |A(\vec{q})|^2 \rangle} \left(\frac{1}{N_p} \left\langle \sum_{j=1}^{N_p} \sum_{i=1}^{N_p} e^{i\vec{q}(\vec{R}_i - \vec{R}_j)} \right\rangle - 1 \right) \quad (2.65)$$

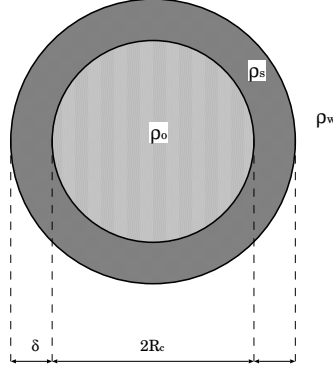


Figure 2.6: Core-shell geometry schematic picture.

gives information about place and interaction between particles in solution. If there is no correlation among particles, $S(\vec{q})$ becomes unity and the scattering cross section (eq. 2.63) is simply written as

$$\frac{d\Sigma}{d\Omega}(\vec{q}) = \frac{N_p}{V} P(\vec{q}) \quad (2.66)$$

If the particles are uniform, the structure factor becomes

$$S(\vec{q}) = \frac{1}{N_p} \left\langle \sum_{j=1}^{N_p} \sum_{i=1}^{N_p} e^{i\vec{q}(\vec{R}_i - \vec{R}_j)} \right\rangle \quad (2.67)$$

This limit is achieved for spherical particles with small polydispersity.

2.3.2 Core-shell sphere formfactor

In the case of a homogeneous spherical particle $\Delta\rho(\vec{r}) = \text{const.}$ For the scattering amplitude equation 2.60 becomes

$$A(\vec{q}) = \Delta\rho \int_{V_{\text{sphere}}} d\vec{r} e^{i\vec{q}\vec{r}} \quad (2.68)$$

For the spherical polar coordinates with the z -axis parallel to \vec{q} one obtains

$$A(q) = \Delta\rho \int_0^R dr \int_{-\pi}^{\pi} d\phi \int_{-\pi/2}^{\pi/2} d\theta r^2 \sin\theta e^{iqr \cos\theta} \quad (2.69)$$

and thus

$$A(q, R) = \Delta\rho \frac{4}{3}\pi R^3 \frac{3[\sin(qR) - qR\cos(qR)]}{(qR)^3} = \Delta\rho \frac{4}{3}\pi R^3 \frac{3}{qR} j_1(qR) \quad (2.70)$$

where R is the sphere radius and j_1 is the Bessel function of first kind. Normalized to the volume equation 2.70 gives:

$$F_s(q, R) = \frac{A(q, R)}{\Delta\rho V_{sphere}} = \frac{3}{qR} j_1(qR) \quad (2.71)$$

Formula 2.64 includes the averaging over orientations. So for the spherically symmetric particles $P(q) = A^2(q)$.

The form factor of the core-shell spherical particle is obtained on the basis of the form factor for the spherical particle (eq. 2.71). If the radius of the core is R_c , the thickness of the shell is δ , scattering length densities of the core, shell, and solvent are ρ_o , ρ_s and ρ_w , respectively, the form factor reads:

$$P(q) = [\Delta\rho_{core} V_{core} F_s(q, R_c) + \Delta\rho_{shell} V_{shell} F_s(q, R_c + \delta)]^2 \quad (2.72)$$

where $\Delta\rho_{core} = (\rho_s - \rho_o)$, $\Delta\rho_{shell} = (\rho_w - \rho_s)$, $V_{core} = 4\pi R_c^3/3$ and $V_{shell} = 4\pi(R_c + \delta)^3/3$. Please note, that the indices of scattering lengths correspond to oil, surfactant and water.

2.3.3 Core-shell ellipsoid of revolution formfactor

If the scattering particles have the form of an ellipsoid with semi axes $R, R, \varepsilon R$, its form factor obtained by averaging over orientations relative to scattering vector \vec{q} reads:

$$P(q) = \int_0^{\pi/2} F_s^2(q, r(R, \varepsilon, \alpha)) \sin \alpha \, d\alpha \quad (2.73)$$

Here we used $F_s(q, r(R, \varepsilon, \alpha))$ from equation 2.71 and $r(R, \varepsilon, \alpha) = R(\sin^2 \alpha + \varepsilon^2 \cos^2 \alpha)^{1/2}$. This expression was obtained by [33]. It is easy to generalize the

form factor for a core-shell particle

$$P(q) = \int_0^{\pi/2} [\Delta\rho_{core}V_{core}F_s(q, r(\varepsilon_c, \alpha)) + \Delta\rho_{shell}V_{shell}F_s(q, r(\varepsilon_s, \alpha))]^2 \sin \alpha \, d\alpha \quad (2.74)$$

As above, volumes of core and shell are $V_{core} = 4\pi\varepsilon_c R_c^3/3$ and $V_{shell} = 4\pi\varepsilon_s(R_s + \delta)^3/3$ respectively, $\Delta\rho$ is the difference of the scattering length densities as for the core-shell sphere formfactor and $\varepsilon_c, \varepsilon_s$ are the axis ratios of core and shell respectively. In the results section we discuss the mean axis ratio $\varepsilon = \frac{1}{2}(\varepsilon_c + \varepsilon_s)$ only.

2.3.4 Core-shell cylinder formfactor

For particles with cylindrical symmetry it is necessary to calculate the orientation average of the cylinder axis with respect to \vec{q} . For the homogeneous cylinder with constant scattering length density, choosing cylindrical coordinates with z -axis in the direction of the cylinder axis, we have:

$$A(q, \beta) = \Delta\rho \int_{-L/2}^{L/2} dz \int_0^R dr \int_{-\pi}^{\pi} d\phi \, r e^{iqz \cos \beta + iqr \sin \beta \cos \phi} \quad (2.75)$$

where R and L are the radius and the length of cylinder. β is the angle between \vec{q} and the axis of the cylinder, and ϕ is the angle between the projection of the vector \vec{q} on the radial cylinder plane. r is the cylindric coordinate. With the use of Bessel j_n functions we obtain

$$\begin{aligned} A(q, \beta) &= \Delta\rho \frac{2 \sin(qL/2 \cos \beta)}{q \cos \beta} \int_0^R dr \, r 2\pi j_0(qr \sin \beta) \\ &= \Delta\rho \frac{4\pi \sin(qL/2 \cos \beta)}{q \cos \beta} \frac{R j_1(qR \sin \beta)}{q \sin \beta} \end{aligned} \quad (2.76)$$

Dividing $A(q, \beta)$ by the scattering contrast and the cylinder volume $\Delta\rho V_{cylinder} = \Delta\rho \pi R^2 L$ we obtain:

$$F_c(q, R) = \frac{2j_1(qR \sin \beta)}{qR \sin \beta} \frac{\sin(qL/2 \cos \beta)}{qL/2 \cos \beta} \quad (2.77)$$

With the use of the previous notation for the spherical core-shell model, we can write the form factor of the cylinder including averaging over its orientation:

$$P(q) = \int_0^{\pi/2} [\Delta\rho_{core}V_{core}F_c(q, R_c) + \Delta\rho_{shell}V_{shell}F_c(q, R_c + \delta)]^2 \sin\beta d\beta \quad (2.78)$$

here volumes for the core and shell are $V_{core} = \pi LR_c^2$ and $V_{shell} = \pi L(R_c + \delta)^2$. End caps are neglected by using one identical length L .

2.3.5 Polydispersity

When the particles are not uniform in size, the form factors (eqs. 2.72,2.78) should be averaged over the particle distribution. Concerning the experimental data, we used averaging over the core radius for the spherical shell and over the radius of the cylindrical shell for the cylindrical core shell model.

$$\langle P(q) \rangle = \int_0^{\infty} P(q, r)f(r)dr \quad (2.79)$$

The function $f(r)$ should be a narrow size distribution function. For such function usually the Gauss or the Schulz-Zimm distribution functions are chosen [34]. For our model fitting, we used the normalized ($\int_0^{\infty} f(r)dr = 1$) Schulz-Zimm distribution [35], [36].

$$f(r) = \frac{(z+1)^{z+1}r^z}{r_0^{z+1}\Gamma(z+1)}e^{-\frac{(z+1)r}{r_0}} \quad (2.80)$$

where r_0 is the mean core radius and $\Gamma(x)$ is the gamma function. With this distribution it is possible to calculate the integral 2.79 analytically [34]. However, complicated hypergeometric functions are involved then. The normalized standard deviation or polydispersity ϵ is connected with the parameter z by:

$$\epsilon \equiv \frac{\langle (r - r_0)^2 \rangle^{1/2}}{r_0} = \frac{1}{\sqrt{1+z}} \quad (2.81)$$

2.3.6 Structure factor

When the density of particles in the system is large, one cannot neglect the inter-particle interaction, and the structure factor (eq. 2.65) should be considered. To calculate the structure factor $S(q)$, one needs to solve the Ornstein-Zernike equation for the direct correlation function $c(r)$ using a known interaction potential $U(r)$ [37]. Actually, for polydisperse particles, the partial structure factors $S_{ij}(\vec{q})$ should be calculated from the matrix form of the Ornstein-Zernike equation for the pair potential $U(r_{ij})$ between particles with hard-core diameters σ_i, σ_j . But with the assumption that the particle size and position are uncorrelated, we have to deal with the average structure factor $S(\vec{q})$ (eq. 2.65). The simplest model for the structure factor is the hard-sphere model that can be solved with the Percus-Yevick approximation. This approximation yields an analytical expression that depends on the hard sphere diameter σ and the number density of hard spheres in the system n . The number density of hard spheres is related to its volume fraction ϕ by $\phi = \pi n \sigma^3 / 6$. So we obtain:

$$S(q) = \frac{1}{1 - nc(q)} \quad (2.82)$$

where $c(q)$ is the Fourier transform of the direct correlation function.

$$c(q) = \int_0^\sigma (-\alpha - \beta r - 0.5\alpha\phi r^3) e^{-i\vec{q}\vec{r}} d\vec{r} \quad (2.83)$$

with the coefficients α and β given by [38]:

$$\alpha = \frac{(1 + 2\phi)^2 + \phi^3(\phi - 4)}{(1 - \phi)^4} \quad (2.84)$$

$$\beta = -\phi \frac{18 + 20\phi - 12\phi^2 + \phi^4}{3(1 - \phi)^4} \quad (2.85)$$

This is a good approach for our system, because we used nonionic components and the main interaction between the droplets is the result of steric repulsion.

Chapter 3

Aspects of small angle neutron scattering

3.1 Experimental setup

The schematic picture of the experimental setup is shown in Fig. 3.1. In our case neutrons are a result of a nuclear chain reaction in the reactor (FRJ-2). The neutrons are moderated by D_2O before they can react with the next nucleus. A cold source is inserted in the reactor for the extraction of some neutrons, which are moderated to low temperatures ($\sim 30\text{K}$). The result is a polychromatic neutron beam, which is monochromated by a neutron velocity selector (here the scheme starts). This is a rotating cylinder with tilted absorbing lamellae. Only neutrons with a defined wavelength λ ($\Delta\lambda/\lambda \approx 0.1$) can pass. Neutron guides bring the neutrons to the collimation aperture. Then, the neutrons propagate freely to the sample aperture, which defines the divergence of the beam. The neutrons hit the sample and are either scattered or not. The transmitted (non-scattered) neutrons hit the beam stop on the detector and are used to measure the transmission of the sample. The scattered neutrons are detected on the position sensitive detector, which are used to measure the macroscopic cross section of the sample. The collimation and detector distances are varied within 1 and 20 meters to achieve lower or higher resolution. We perform our scattering experiments at the KWS2 diffractometer in the Forschungszentrum Jülich. Some of the parameters concerning the experimental setup are summarized in [table 3.1](#).

One assumes that the size of the sample is much smaller than distances from the source to the sample and from the sample to the detector. The wave field of the incident and scattered beam is described by the wave vectors \vec{k} and \vec{k}' respectively. In the case of the elastic scattering $k = |\vec{k}| = k' = |\vec{k}'| = \frac{2\pi}{\lambda}$. Here

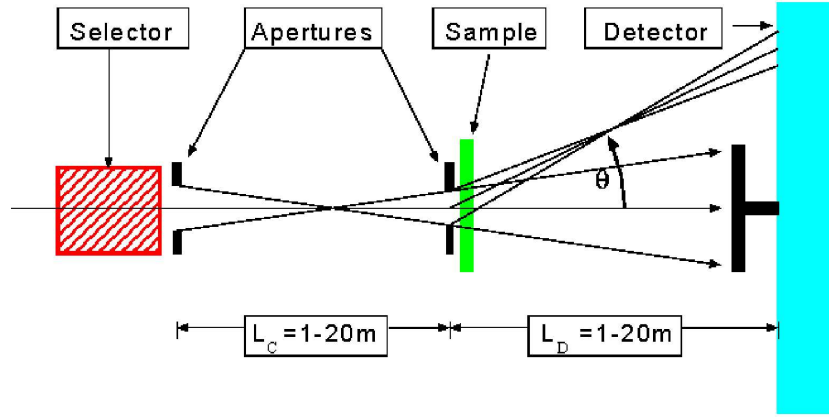


Figure 3.1: *Schematic picture of a scattering experiment.*

λ is the wavelength of neutrons adjusted by the velocity selector. The scattering vector $\vec{Q} = \vec{k} - \vec{k}'$ is defined as the difference between the incident and the scattered wave vector. The absolute value of the scattering vector is given by:

$$Q = \frac{4\pi}{\lambda} \sin \frac{\theta}{2} \quad (3.1)$$

The scattering angle θ is depicted in Fig.3.1.

3.2 Absolute calibration

The obtained scattering intensity should be treated by corresponding reduction procedures to obtain the scattering cross-section, which is independent of the experimental setup and the background. The measured intensity is connected to the cross section $\frac{d\Sigma}{d\Omega}$ by

$$I = I_i D_e \Delta\Omega A T d \left(\frac{d\Sigma}{d\Omega} \right) \quad (3.2)$$

where I_i is the incident beam intensity, D_e is the detector efficiency, A is the irradiated sample area, d is the sample thickness, T is the sample transmission and $\Delta\Omega$ is the angle of one detector element. For the absolute calibration we used a reference material with a flat cross section in the measured Q range. Mainly

Table 3.1: *Instruments details*

Characteristic	KWS2
Monochromator	Velocity selector [DORNIER]
$\Delta\lambda/\lambda$	0.1
Wavelength, λ	7.3Å
Sample aperture, d_s	~ 1 cm
Collimation aperture,	3×3 cm
Collimation length	2-20 m
Detector length	1.4-20 m
Detector:	
Active area	50×50 cm ²
Gas	³ He
Space resolution	8 mm
Max.pulse rate	7 kHz
Dead time, τ_d	15 μ s
Q-range	$2 \cdot 10^{-3} - 0.2$ Å
Neutron flux at sample	$10^5 - 6 \cdot 10^6$ n/cm ² s

Lupolene is used, but water is appropriate too. Using indices s for the sample, and l for Lupolene, and the definition for the solid angle $\Delta\Omega \sim L^{-2}$ one obtains:

$$\left(\frac{d\Sigma}{d\Omega}\right)_s = \frac{I_s L_s^2 d_l T_l}{I_l L_l^2 d_s T_s} \left(\frac{d\Sigma}{d\Omega}\right)_l \quad (3.3)$$

The Lupolene calibration constant is a function of wave length $\mu_l(\lambda) = d_l \frac{d\Sigma}{d\Omega_l} T_l$, which is calibrated by a primary standard. For our experimental setup $\mu_l(7.3\text{Å}) = 0.0734$. The scattering cross-section can be written in the form:

$$\left(\frac{d\Sigma}{d\Omega}\right)_s = \frac{\mu}{C} I_s \quad (3.4)$$

in this expression $C = I_l T_s d_s L_l^2 / L_s^2$. Corrections caused by the scattering of the sample container and electronic noise should be included. Using the the empty cell I_{EC} and transmission T_{EC} and the background intensity I_{BG} for blocked

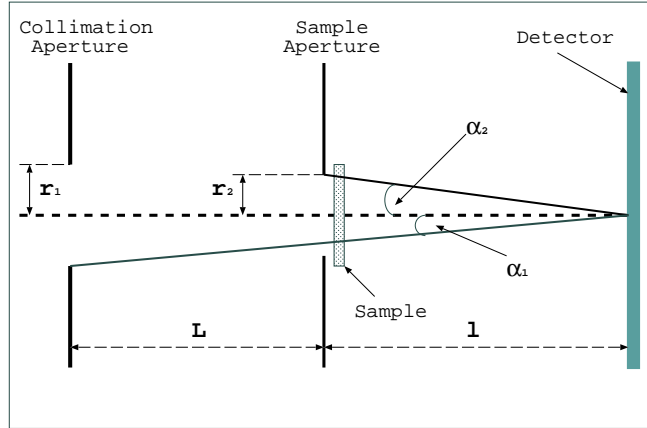


Figure 3.2: *Determination of divergence by geometric factors.*

neutrons, one finally obtains:

$$\left(\frac{d\Sigma}{d\Omega}\right)_s = \frac{\mu (I_s - I_{BG}) - T_s(I_{EC} - I_{BG})/T_{EC}}{C (I_l - I_{BG}) - T_l(I_{EC} - I_{BG})/T_{EC}} \quad (3.5)$$

3.3 Resolution effects

The Limited resolution of the instrument leads to smearing of the measured scattering data. The reason can be wavelength spread, collimation effects and detector resolution. So, the measured intensity at Q_0 is the averaged scattering cross section $\frac{d\Sigma(Q)}{d\Omega}$ by the distribution (resolution) function $R(Q, Q_0)$ [39, 40].

$$I(Q) = \int R(Q, Q_0) \frac{d\Sigma(Q)}{d\Omega} dQ \quad (3.6)$$

The distribution function for the radially averaged data [39] reads

$$R(Q, Q_0) = \frac{Q}{\sigma_{Q_0}^2} \exp\left[-\frac{Q^2 + Q_0^2}{2\sigma_{Q_0}^2}\right] I_0\left[\frac{QQ_0}{\sigma_{Q_0}^2}\right] \quad (3.7)$$

where I_0 is the modified Bessel function and $\sigma_{Q_0}^2$ is related to smearing effects caused by the different physical reasons:

$$\sigma_{Q_0}^2 = \frac{1}{8 \ln 2} \left(\left(Q_0 \frac{\Delta \lambda}{\lambda} \right)^2 + (k_0 \Delta \beta)^2 + (k_0 \Delta Q_D)^2 \right) \quad (3.8)$$

Here, $\Delta \lambda / \lambda$ comes from the wavelength spread, $k_0 = 2\pi / \lambda$ is the absolute value of the wave vector. The parameter $\Delta \beta$ accounts for the finite collimation effect and the parameter ΔQ_D accounts for the detector resolution. The parameter $\Delta \beta$ is defined by the next equation.

$$\Delta \beta = \begin{cases} \frac{2r_1}{L} - \frac{r_2^2(l+L)^2}{2r_1 l^2 L}, & \alpha_1 \geq \alpha_2 \\ 2r_2 \left(\frac{1}{L} + \frac{1}{l} \right) - \frac{r_1^2 l}{2r_2 L(L+l)}, & \alpha_1 < \alpha_2 \end{cases} \quad (3.9)$$

where L and l are distances from the source to the sample and from the sample to the detector respectively, r_1 is the radius of the source aperture and r_2 is the radius of the sample aperture. The angles are $\alpha_1 = r_1 / (L + l)$ and $\alpha_2 = r_2 / l$. The whole geometry is depicted in figure 3.2. The first case of equation 3.9 is the more common one. It appears for rather small sample apertures, which we chose in our set-up. Then, the resolution is dominated by the divergence defined by an ideal collimation. The correction term accounts for the finite sample aperture, which makes the characteristic divergence slightly smaller.

3.4 Multiple scattering

Since our sample thickness d is of the order of one millimeter, multiple scattering occurs for cross sections $\frac{d\Sigma}{d\Omega} \gg 10 \text{ cm}^{-1}$. For small angles, predominantly elastic neutron scattering is the responsible mechanism [41]. The scattering probability of the experiment is $H(\vec{Q}) = d_s \frac{d\Sigma^*}{d\Omega}(\vec{Q})$, and the apparent scattering probability is $S(\vec{Q}) = d_s \frac{d\Sigma}{d\Omega}(\vec{Q})$ where d_s is the sample thickness. The simple expression connects the Fourier images with the real space.

$$s(r) = k_0^2 \ln \left[1 + \frac{h(r)}{k_0^2 - h(0)} \right] \quad (3.10)$$

Here $s(r)$ and $h(r)$ are the two dimensional Fourier transforms of s and h :

$$s(\vec{r}) = \int e^{i\vec{Q}\vec{r}} S(\vec{Q}) d^2\vec{Q} \quad (3.11)$$

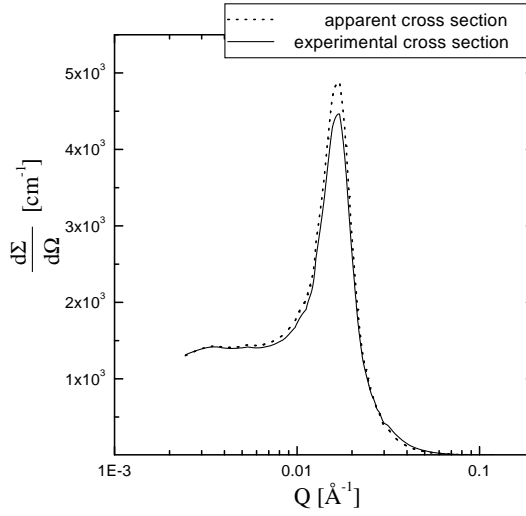


Figure 3.3: *An example of deviation caused by multiple scattering for the bicontinuous microemulsion. The lower curve represents experimental data with multiple scattering. The upper curve represents corrected data. This figure makes it plausible that mainly the correlation length ξ (peak width) is affected and not the domain spacing d (peak position).*

$$h(\vec{r}) = \int e^{i\vec{Q}\vec{r}} H(\vec{Q}) d^2\vec{Q} \quad (3.12)$$

k_0 is the wave number of the beam. If S and H depend on $|Q|$ only, the integrals 3.11, 3.12 turn to one dimensional integrals

$$s(r) = 2\pi \int J_0(Qr) S(Q) Q dQ \quad (3.13)$$

$$h(r) = 2\pi \int J_0(Qr) H(Q) Q dQ \quad (3.14)$$

The final result for the scattering probability $S(Q)$ is obtained by the integral

transform to Q -space:

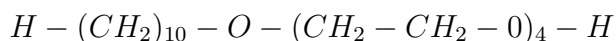
$$S(Q) = \frac{1}{2\pi} \int_0^{r_{max}} J_0(Qr) s(r) r dr \quad (3.15)$$

For the calculation r_{max} should be larger than the maximum correlation length in the system, and Q_{max} should be large enough that the integral from Q_{max} to ∞ is negligibly small. Practically, in order to obtain Fourier images $h(\vec{r})$ in real space, the numerical Fourier transform was performed in two dimensions. In order to give an example of deviations caused by multiple scattering, we considered one bicontinuous microemulsion. One example of a multiple scattering correction is shown in fig. 3.3. Depending on the composition of surfactant, the deviations of the domain size d and the correlation length ξ caused by multiple scattering were in the range from 0.1% to 0.7% and from 3% to 7% for d and ξ , respectively.

Chapter 4

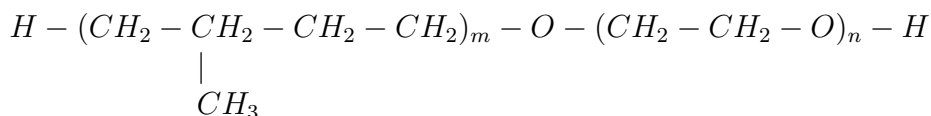
Sample preparation

We investigated microemulsions consisting of oil, water, surfactant with addition of small amounts of diblock copolymers and homopolymers. The surfactant we used, was the non-ionic surfactant like n-Decyltetraoxyethylene ($C_{10}E_4$).



This is a long-chain surfactant with linear structure, and belongs to the most common non-ionic surfactants C_xE_y . Here x is a number of carbon atoms in the hydrophobic alkyl chain, and y is a number of ethylene oxide groups. The hydrogenated surfactant ($C_{10}E_4$) was purchased from Bachem Biochemica GmbH with a purity of 98%, and was used without further purification.

As additives to the microemulsions block copolymers and homopolymers were used. The block copolymers are polyethylenepropylene-co-polyethyleneoxide ($PEP_x - PEO_y$) polymers, where x and y denote the molecular masses of each of the blocks in kg/mol.



The homopolymers were polyethylenepropylene (PEP_5) and polyethyleneoxide (PEO_5). Here 5 kg/mol is the mass of each polymer. All polymers were synthesized by J. Allgaier at IFF, FZ Jülich by living anionic polymerizations; the detailed description of the process can be found in [42]. Some polymer characteristics are summarized in [table 7.1](#) and [table 7.2](#).

The used oil was either n-decane ($C_{10}H_{22}$) or deuterated n-decane. The deuterated n-decane- d_{22} (d-decane) was made by Cambridge Isotope Laboratories with

a purity of 99%. The used water was D_2O from Aldrich Chemical Company, Inc. (purity 99.8%).

Selecting deuterated or hydrogenated components it is possible to obtain scattering from the interface (film contrast) or from solvents (bulk contrast). Bulk contrast for our experiments was observed by using hydrogenated surfactant with D_2O and h-decane while the film contrast was observed with use of d-decane instead. Scattering length densities of materials and its other parameters are summarized in [table 7.3](#).

Chapter 5

The bicontinuous phase

In this chapter we study the bicontinuous microemulsion with a) addition of homopolymer only and b) simultaneous addition of homopolymer and diblock copolymer. First, phase diagrams are discussed in the context with predictions of the saddle splay bending modulus $\bar{\kappa}$. Second, small angle neutron scattering measurements probe the microscopic structure. By fitting the Teubner-Strey model we get two structural parameters: the domain spacing d and the correlation length ξ . Both can be scaled with the surface per volume S/V , which is suitable for the comparison with the Gaussian random field model. The expression for the bending rigidity $\kappa \sim \xi/d$ of the Gaussian random field model is finally discussed in the context with theoretical predictions of κ .

5.1 Results

For the characterization of the system we employ the following volume fractions of components:

$$\phi_o = \frac{V_{oil}}{V_{oil} + V_{water}} \quad (5.1)$$

$$\phi_\delta = \frac{V_{diblock}}{V_{diblock} + V_{surfactant}} \quad (5.2)$$

$$\phi_p = \frac{1}{2} \frac{V_{homopolymer}^W}{V_{homopolymer}^W + V_{water}} + \frac{1}{2} \frac{V_{homopolymer}^O}{V_{homopolymer}^O + V_{oil}} \quad (5.3)$$

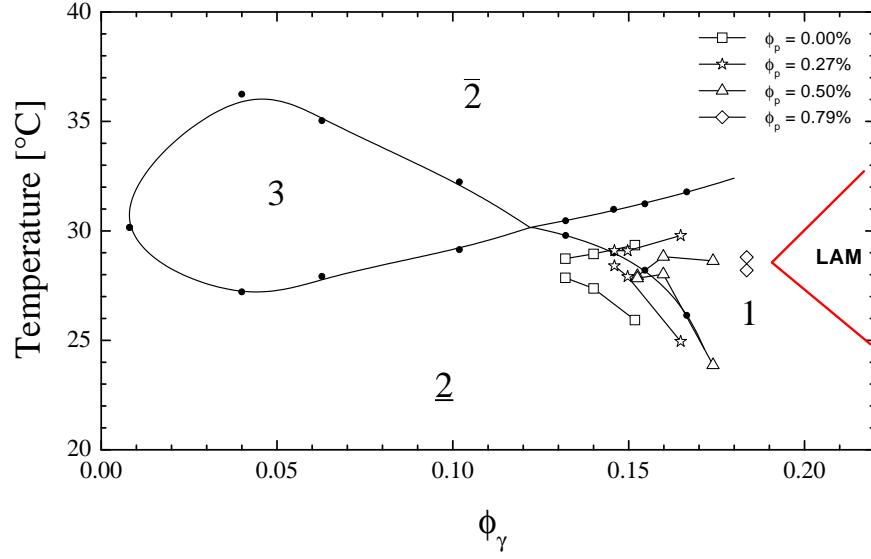


Figure 5.1: *Phase diagram: the shift of the fish tail point (solid line, black dots) for H_2O - n -decane- $C_{10}E_4$. Amounts of water and n -decane are equal. For additions of homopolymers in D_2O - n -decane- $C_{10}E_4$ lines with hollow symbols are used. The temperature shift in the phase diagrams is caused by the use of D_2O instead of H_2O . The lamellar phase is estimated by a measurement at $T = 28^\circ C$.*

$$\phi_\gamma = \frac{V_{surfactant}}{V_{surfactant} + V_{diblock} + V_{oil} + V_{water} + V_{homopolymer}^{O+W}} \quad (5.4)$$

where V_{xx} corresponds to the respective volume of the different components. To achieve a bicontinuous phase, we chose ϕ_o to be 0.5. ϕ_p is the average of the two volume fractions of homopolymers in the oil and water phase, which are virtually identical. Varying these parameters and temperature it is possible to observe the phase behavior of the microemulsion. It is important to notice that the solubility of the surfactant, in our case $C_{10}E_4$, at $30.1^\circ C$ is $2wt\%$ in decane and $0.2wt\%$ in water. So for the accuracy of results, the membrane volume fraction Ψ is the surfactant volume fraction ϕ_γ with accounted solubility.

5.1.1 Addition of homopolymers only

Here we discuss small additions of homopolymers PEP_5 and PEO_5 to the microemulsions. We restricted the study to the equal amounts of water and oil ($\phi_o = 0.5$). The phase diagram (Fig. 5.1) shows the temperature as a function of surfactant content. At low temperatures there is the two-phase region (2) with an excess oil phase, and at high temperatures there is the two-phase region ($\bar{2}$) with an excess water phase. At higher surfactant concentration, there is a one-phase region (1); with addition of more surfactant, the lamellar phase occurs and at lower surfactant concentrations there is also a three-phase region (3), where all three phases: oil-rich, water-rich and microemulsion coexist. Small amounts of homopolymer PEP_5 and PEO_5 added to the microemulsion increase the minimum quantity of surfactant needed to solubilize water and oil, or in other words decrease the efficiency (anti-boosting effect).

The presence of homopolymer chains in water and oil in the neighborhood of membrane causes a change of physical parameters of membrane. The theory of ideal and self-avoided polymers near membrane [43] predicts a decrease of the bending rigidity and an increase of the saddle splay modulus of the membrane (see eqs. 2.19, 2.20). Such changes of the elastic constants should entail a decrease of efficiency because of equation 2.6. The phase diagram measurement provides a qualitative proof of this prediction. The fish tail point moves in the direction to higher surfactant contents for every next portion of homopolymer addition. It is important to check the quantity of this influence. In the neighborhood of the fish tail point, the saddle-splay modulus $\bar{\kappa}$ is predicted to change the sign. More precisely [44], this is true within a constant, since the emulsification failure line is almost parallel to the line of the lamellar to sponge phase transition in the diagram $\ln(\Psi)$ vs $\bar{\kappa}$. Combining equation 2.20, which predicts the effect of homopolymer addition, with 2.6 one obtains:

$$\Psi = \Psi_0 \exp \left[\bar{\beta} \frac{\phi_p}{V_p} (R_{PEP}^3 + R_{PEO}^3) \right] \quad (5.5)$$

where ϕ_p is the volume fraction of homopolymers and V_p is the volume of one polymer, respectively. Theoretically, the value $\bar{\beta} = 0.0795$ is predicted [43].

At figure 5.2, the dependence of the logarithm of membrane volume fraction at the fish tail point is plotted vs. the scaled homopolymer number density. This dependence is linear as follows from equation 5.5, but the prefactor (describing this effect) is different. Comparing the theoretical value and the measured value shows, that the phase diagram is ~ 7 times more sensitive on the homopolymer addition than expected from theory [43].

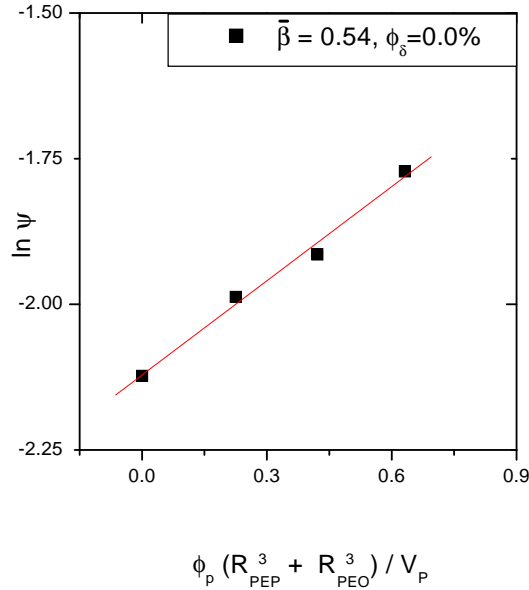


Figure 5.2: *The logarithm of the volume fraction of membrane at the emulsification boundary vs. scaled volume fraction of the homopolymer.*

For a more detailed study of structure and physical parameters of the bicontinuous microemulsion with added homopolymers, we performed SANS measurements on the system. The samples were measured under bulk contrast. The volume fraction of surfactant was held at a range from 13% to 20%. The homopolymers PEP_5 and PEO_5 were added to the oil and water, respectively, in equal amounts with an increment of approximately 0.25% (see table 7.4).

An example of SANS measurements is shown in Fig. 5.3. Here, the macroscopic cross section $\frac{d\Sigma}{d\Omega}$ is depicted vs. wave vector Q . The surface volume fraction Ψ in the samples for the represented scattering curves was held at 0.175 ± 0.003 , and the amount of homopolymers was increased from 0.0% to 0.78%. To make the picture clear, the cross section for every next addition of homopolymer was multiplied by a factor of 10. The high intensity and constant value of scattering cross section at low Q indicates big fluctuations at large scales. In the middle Q region a correlation peak exists at $\sim 0.03 \text{ \AA}^{-1}$. This is a sign of the characteristic length scale for the microemulsion. The value of $2\pi/Q_{max}$ approximately gives the domain size. The width of this peak is connected with the correlation length.

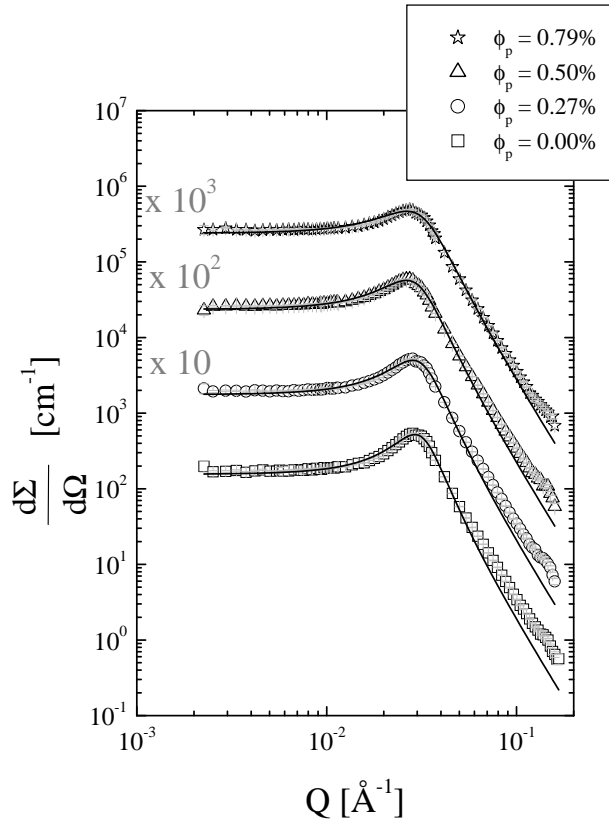


Figure 5.3: *Scattering cross section of bicontinuous microemulsion with homopolymer addition under bulk contrast. The surface volume fraction Ψ is fixed at 0.175. Errors are approximately about the size of symbols in the figure. Solid lines are Teubner-Strey model fitting.*

A Porod behavior at high Q is characteristic for the randomly oriented sharp interfaces. A detailed quantitative analysis of the scattering data was based on the Teubner-Strey formula (eq. 2.29), which was used to describe the peak intensity. Examples of fitting curves are shown in figure 5.3. From the fitting, the characteristic domain size d and correlation length ξ are obtained. This provides a way to look at the structural properties of the bicontinuous microemulsion.

Now we discuss the domain size d as a function of membrane volume fraction Ψ for the samples with different homopolymer content (see Figure 5.4). The dependence of d as a function of homopolymer volume fraction is quiet weak compared to the dependence on the surfactant volume fraction. This implies that the addition of homopolymer does not influence the structure of the microemulsion

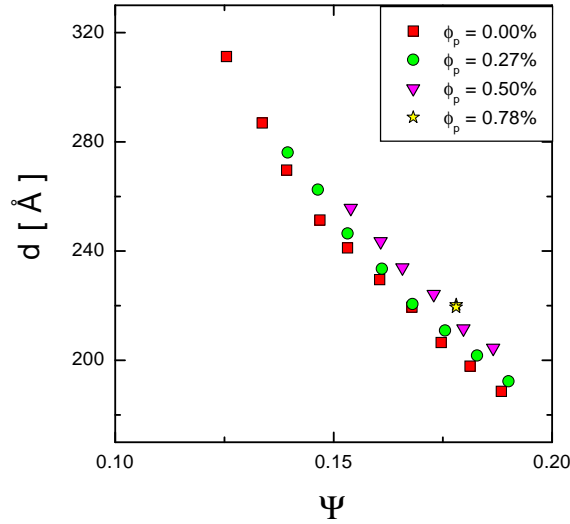


Figure 5.4: *The domain size d of bicontinuous microemulsion with different homopolymer contents obtained from Teubner-Strey model fitting.*

strongly. The structure is mainly governed by the amount of surfactant in the system. Without fluctuations, $d \sim \Psi^{-1}$ for the larger structures. For small surfactant concentrations, fluctuations of the surface can modify this dependence.

Figure 5.5 represents the correlation length ξ as a function of homopolymer content and surfactant content. It is easy to see that the addition of homopolymer decreases the correlation length or increases the strength of *membrane* fluctuations. The same effect but much more strongly is caused by the surfactant addition where the surfactant scales the structure down (compare eq. 2.11). This is already an indication that the bending rigidity decreases with homopolymer addition. So the increase of the homopolymer content causes a small growth of the domain size (compared to the surfactant increase) and makes the strength of fluctuations more pronounced.

From figure 5.6, it is seen that the characteristic domain size, which is d multiplied by corresponding ratio of surface to volume, remains constant with increased sur-

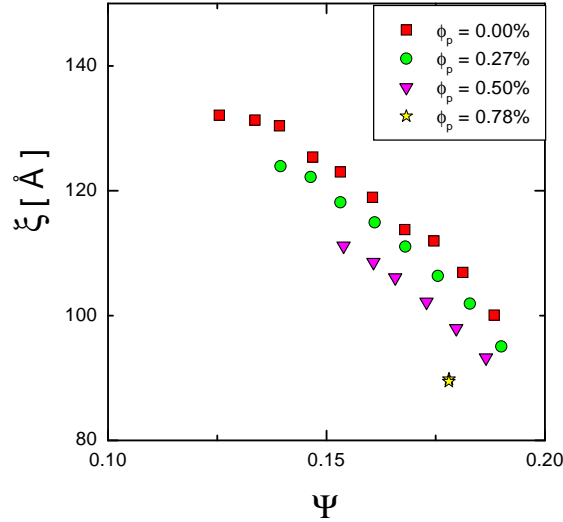


Figure 5.5: *The correlation length ξ of bicontinuous microemulsion with different homopolymer contents obtained from Teubner-Strey model fitting.*

face content. This is reasonable within the variational approach of the Gaussian random field theory (see eq. 2.10). The characteristic domain size does not depend much on the added homopolymer (5%, for $\phi_p = 0.005$). A more pronounced effect of the homopolymer addition is observed with the correlation length, which is decreased (10%, for $\phi_p = 0.005$). The Gaussian random field model would allow to calculate the bending rigidity from the scaled correlation length, but we will use the more common approach of the next paragraph.

On the basis of the Gaussian random field theory predictions, we can calculate the bending rigidity κ of the membrane if we know d and ξ (see eq. 2.9). In figure 5.7, the membrane volume fraction of the microemulsion is plotted as a function of the renormalized bending rigidity and homopolymer content. At this figure three different areas were separated by the solid lines. These areas correspond to the different phases of microemulsion. At low κ there is a three phase coexistence region. At high surfactant contents the lamellar phase appears. The presence of

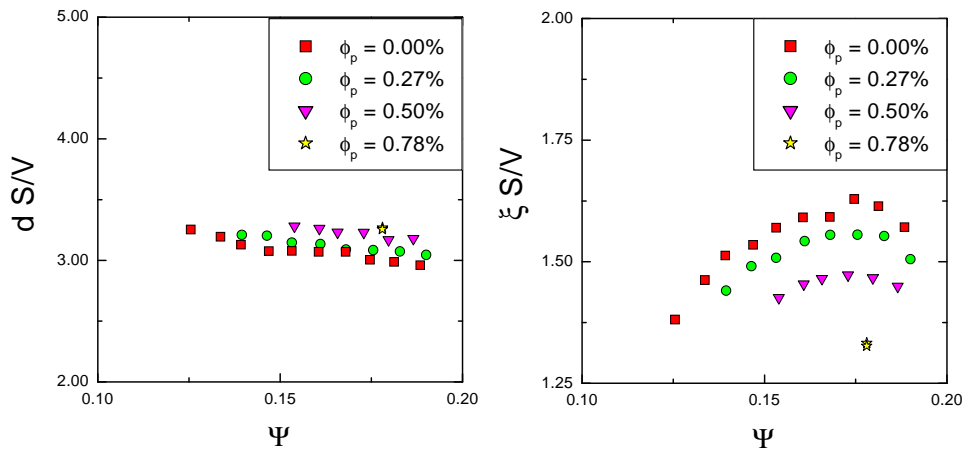


Figure 5.6: *Scaled periodicity (on the left) and correlation length (on the right) as a function of membrane content*

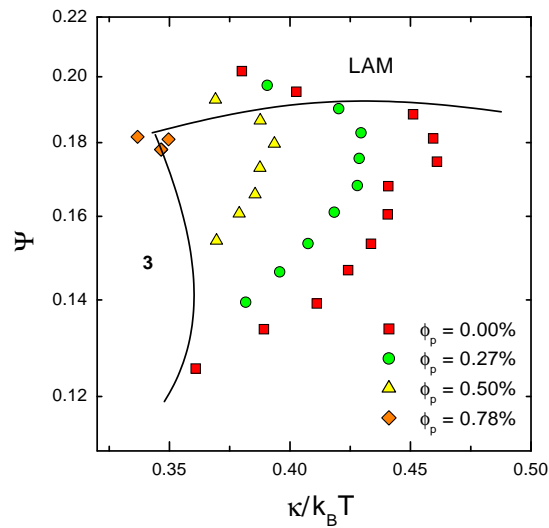


Figure 5.7: *Dependence of membrane volume fraction vs. bending modulus of membrane at different homopolymer additions. Solid lines separate regions of three phase coexistence **3** and lamellar phase **LAM**.*

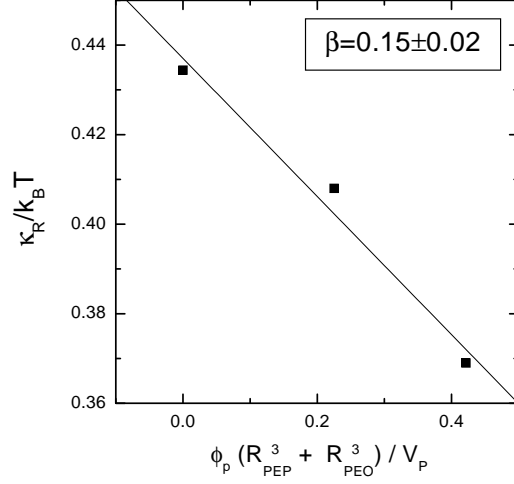


Figure 5.8: *The renormalized bending rigidity as a function of scaled volume fraction of the homopolymer.*

a lamellar phase in the system was visually observable by turbidity and indicated by the change of the shape of the scattering curves. This functional dependence between the elastic constant κ , surfactant content Ψ and homopolymer content ϕ_p provides a way to check the effect of thermal fluctuations on κ . For the spatial renormalization we get:

$$\ln(\Psi/\Psi_0) = \frac{4\pi}{\alpha} \frac{\kappa}{k_B T} \quad (5.6)$$

We found for these samples $\alpha = 3.2 \pm 0.5$. That result is in good agreement with the theoretical prediction ($\alpha = 3$).

Next, we can check the dependence of renormalized bending rigidity κ_R on homopolymer content (see also figure 5.8). The data points correspond to

$$\frac{\Delta\kappa_R}{k_B T} = -\beta\phi_p \frac{(R_{PEP}^3 + R_{PEO}^3)}{V_p} \quad (5.7)$$

We obtained $\beta = 0.15 \pm 0.02$ which is much larger than the theoretically predicted value $\beta = 0.0238$ from [43]. The origin of this discrepancy will be discussed below. This discrepancy of an approximately 7 times higher sensitivity agrees with phase diagram measurements (see fig. 5.2).

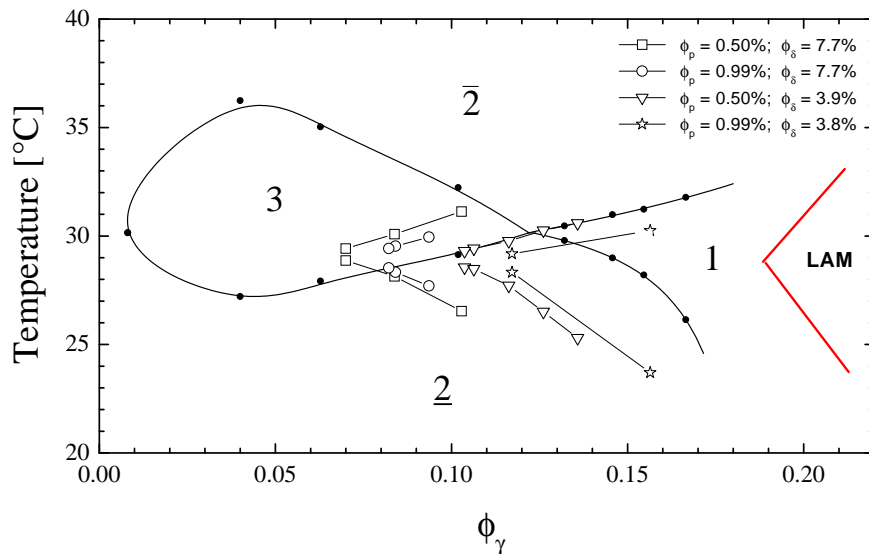


Figure 5.9: Phase diagram: the shift of the fish tail point (solid line, black dots) for H_2O - n -decane- $C_{10}E_4$ amounts of water and n -decane are equal with addition of homopolymers and diblock copolymers (lines with hollow symbols) in D_2O - n -decane- $C_{10}E_4$. The temperature shift of the phase diagrams is caused by the use of D_2O instead of H_2O .

5.1.2 Simultaneous addition of homopolymers and diblock copolymers

In order to achieve a microemulsion with a desired efficiency and adjustable viscosity, the next step was the simultaneous addition of homopolymers PEP_5 , PEO_5 and symmetric diblock copolymer PEP_5PEO_5 . We now want to check, if the two opposite effects superimposed. The phase diagrams for our samples are shown in figure 5.9. With increasing amount of diblock copolymer the fish tail point consequently moves to lower surfactant amounts. The effect of homopolymers is opposite: For a given diblock copolymer amount the fish tail point shifts to higher ϕ_γ with increased homopolymer content. The additions have opposite effects on the effectiveness of surfactant. While the homopolymers decrease the surfactant stabilization properties (see fig. 5.1), the diblock copolymer increases the surfactant efficiency [2].

For the analysis of all effects, we first start with the information that is extracted from the phase diagram measurement. In figure 5.10, the membrane volume

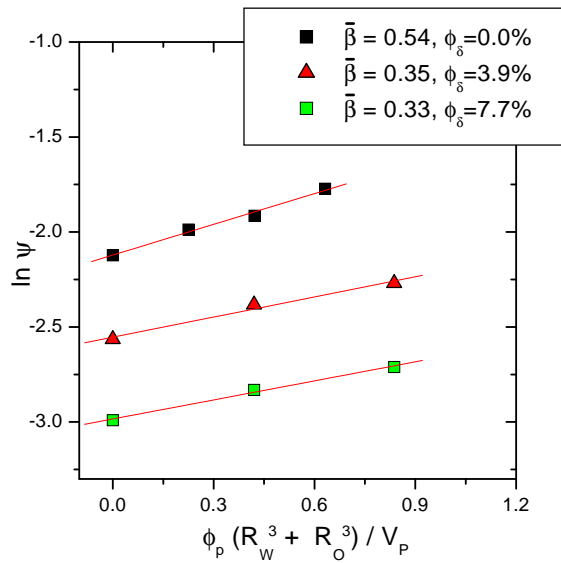


Figure 5.10: *The logarithm of the volume fraction of membrane at the emulsification boundary vs. scaled volume fraction of the homopolymer.*

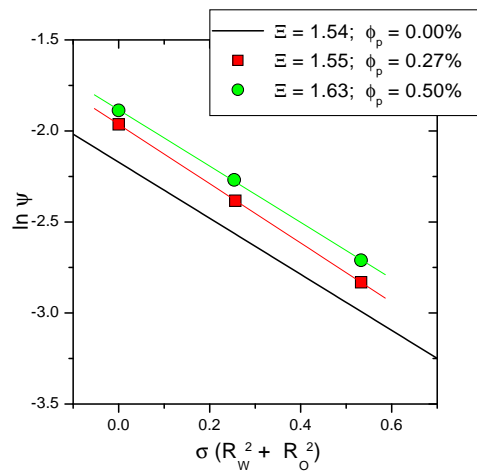


Figure 5.11: *Membrane content vs. diblock copolymer grafting density in the vicinity of emulsification failure boundary. The solid line corresponds to measurements of H. Endo [2]*

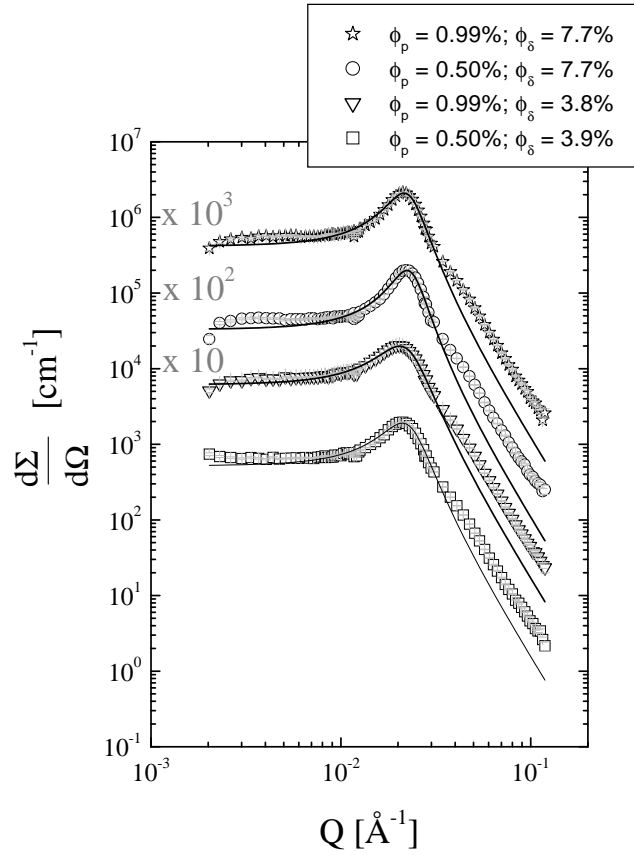


Figure 5.12: *Scattering cross section of bicontinuous microemulsion with homopolymer and diblock copolymer addition under bulk contrast. Errors are approximately about the size of symbols in the figure. Solid lines are Teubner-Strey model fitting.*

fraction is plotted as a function of homopolymer content. Similar to fig. 5.2 we observe an increase of the surfactant content with more homopolymer, which means a decrease of efficiency. The observed curves for certain diblock copolymer additions are quite parallel. The slopes $\bar{\beta}_1 = 0.35$ and $\bar{\beta}_2 = 0.33$ are comparable to $\bar{\beta} = 0.54$ without diblock copolymer (see eq. 5.5). This is already a hint for a possible superposition of the two opposite polymer effects.

As in the case of homopolymer addition we use the result of equation 2.6 for the saddle splay modulus $\bar{\kappa}$ and membrane volume fraction at the vicinity of the emulsification boundary. Combined with result of equation 2.15 for the diblock

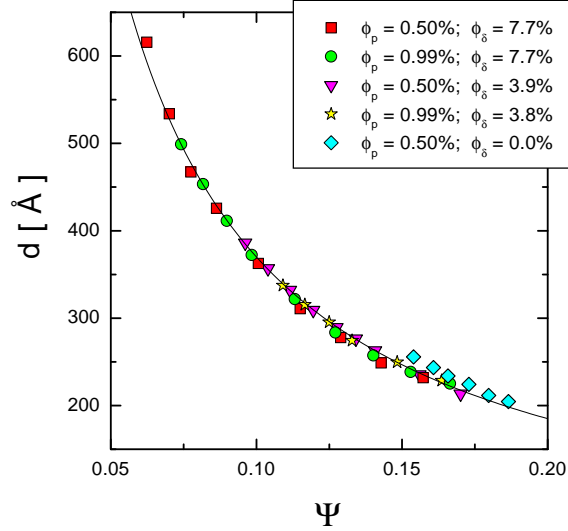


Figure 5.13: *The domain size of the bicontinuous microemulsion with different homopolymer and diblock copolymer contents obtained from Teubner-Strey model fitting. The obtained simple dependence of d as a function of Ψ shows that only the amount of surfactant is responsible for the structure. The solid line represents the dependence of d as a function of Ψ as obtained by fitting $d = 37\text{\AA}/\Psi$.*

anchoring effect on the saddle splay modulus, we obtained [2]:

$$\Psi = \Psi_0 \exp [-\Xi\sigma(R_{PEP}^2 + R_{PEO}^2)] \quad (5.8)$$

where σ is the diblock copolymer grafting density. In figure 5.11, the dependence of membrane volume fraction at the fish tail point vs. scaled polymer grafting density for samples without and with homopolymer is shown. The theory predicts $\Xi = \frac{\pi}{5} \approx 0.63$ for the ideal polymer chains. The experimental value obtained for the diblock copolymers anchored to the membrane is $\Xi = 1.54 \pm 0.05$ [2]. The values of Ξ obtained for our case of diblock copolymer and homopolymers added lie in the range of pure diblock copolymer addition $\Xi_1 = 1.55 \pm 0.05$, and $\Xi_2 = 1.63 \pm 0.05$. This result implies that the addition of homopolymer does

not inflict on the mechanism of diblock copolymer. The two opposite effects are superposable.

As in the case of homopolymer addition, to get deeper insight in the physics of the problem we performed SANS measurements. The samples were measured under bulk contrast. Volumes of *n*-decane and D_2O were approximately equal. The volume fraction of surfactant was held at a range from 7% to 20%. The homopolymers PEP_5 and PEO_5 were added to the oil and water respectively in equal amounts with increment of approximately 0.5% (see table 7.5). The amount of diblock copolymer PEP_5PEO_5 was kept constant at two values $\phi_\delta \approx 3.8\%$ and $\phi_\delta \approx 7.7\%$.

As an example of SANS measurements, the macroscopic cross section vs. wave vector is shown in Figure 5.12. The surface volume fraction in the samples for the represented scattering curves was held at 0.129 ± 0.005 and amount of homopolymers and diblock was varied. To make the picture clear the cross section data for the different samples was consequently multiplied by a factor of 10. A qualitative discussion of a single scattering curve is given for figure 5.3. From the picture, it is seen that additions of homopolymer make the peak broader and less pronounced. This means a decrease of the correlation length. The addition of the diblock copolymer causes the opposite change of the curves. A detailed quantitative analysis of the scattering data was based on the Teubner-Strey formula 2.29 which was used to describe the peak intensity. Examples of fitting curves are shown in figure 5.12.

The domain size d is plotted in figure 5.13 as a function of membrane content for the samples with different homopolymer and diblock copolymer content obtained by the Teubner-Strey fitting of scattering curves. The function $d = 37\text{\AA} \times \Psi^{-1}$ can describe the data reasonably well. This function is not sensitive to polymer additions, but can be characteristic for the surfactant. This universal behavior (no polymer influence) indicates that the surfactant dominates the structure formation.

The figure 5.14 represents the correlation length as a function of surfactant content, homopolymer content and diblock copolymer content. It is easy to see that the addition of homopolymer decreases the correlation length or increases the strength of *membrane* fluctuations. The same effect is caused by the surfactant addition. On the other hand, the addition of diblock copolymer causes an increase of the correlation length and suppresses fluctuations. From this plot, the superposition of the two different effects of polymer additions is clearly seen. Again, the polymer effect mainly results from the bending rigidity, whereas the surfactant effect causes the scaling of the structure (compare with fig. 5.5).

The Gaussian random field theory with variational approach of the spectral density provides for the sponge phase geometry the way to compare qualitative pre-

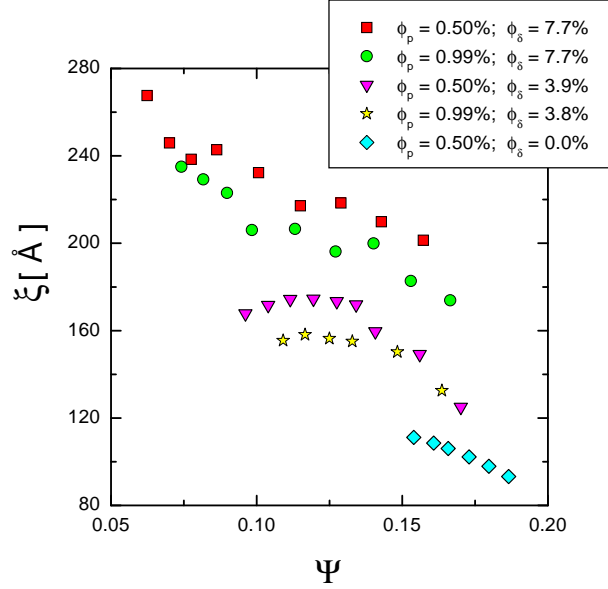


Figure 5.14: *The correlation length of bicontinuous microemulsion with different homopolymer and diblock copolymer contents obtained from Teubner-Strey model fitting.*

dictions of the theory (see eq.2.10) and experimentally obtained system parameters. As follows from the theory, the domain size multiplied by the ratio of surface to volume is a constant function of surface content. That is demonstrated on the left part of the figure 5.15. The scaled domain size is a weak function of the polymer addition (less than 10%). The scaled correlation length as follows from the theory should be proportional to the bending rigidity of membrane. The addition of diblock copolymers suppresses fluctuations on the short scale. This agrees with the picture of the small decrease of the correlation length when homopolymers added (eq. 2.21).

The Gaussian random field theory gives the function to obtain the renormalized bending rigidity of membrane from the experimental values of d and ξ for the system (see eq.2.9). This is in turn a way to compare the theoretically predicted effect of polymer addition and compare it with results obtained from phase diagram analysis.

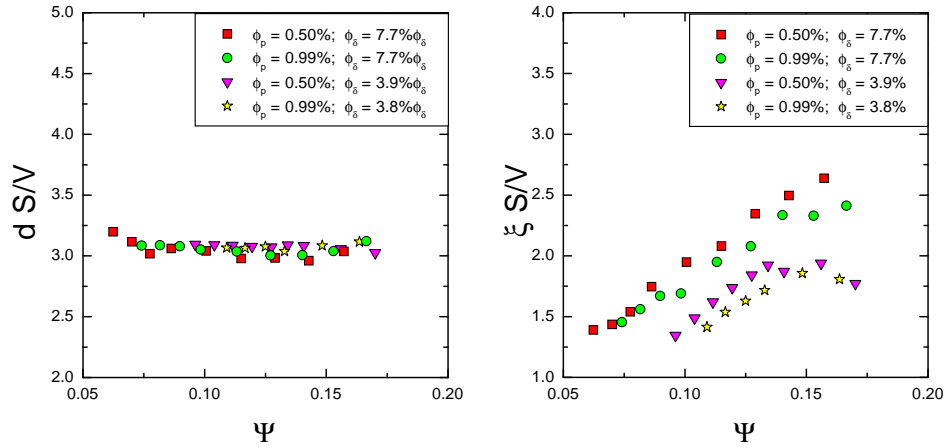


Figure 5.15: Scaled periodicity (on the left) and correlation length (on the right) as a function of membrane content

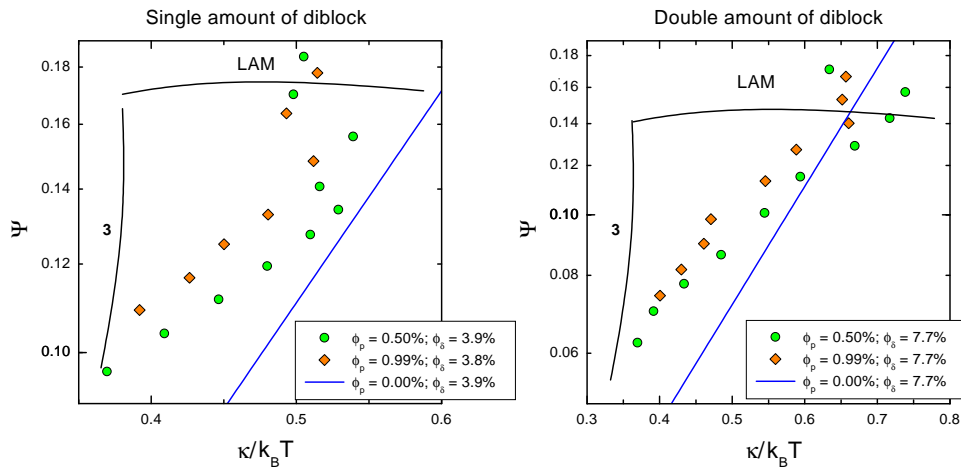


Figure 5.16: Membrane content vs. renormalized bending rigidity for different addition of polymers, solid line calculated function for the system composition but without homopolymer addition.

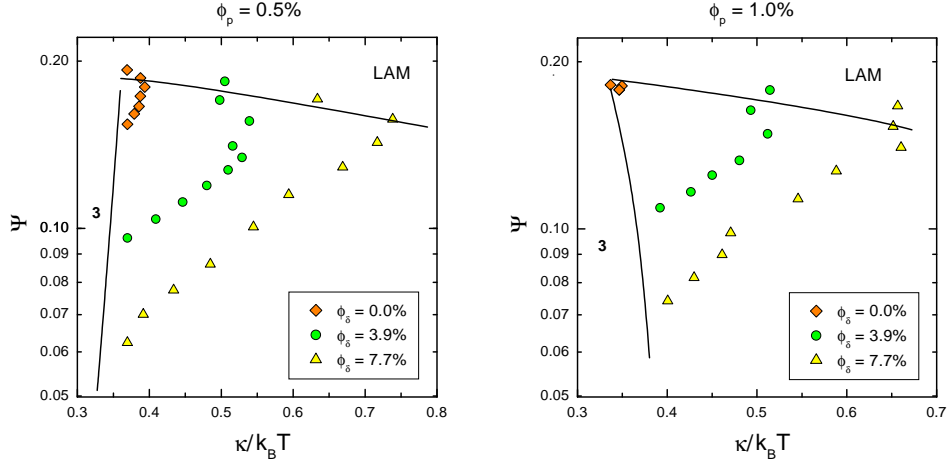


Figure 5.17: *Membrane content vs. renormalized bending rigidity for different amounts of the diblock copolymer added. On the left part amount of homopolymer $\phi_p \approx 0.5\%$. On the right part amount of homopolymer $\phi_p \approx 1.0\%$*

In figure 5.16 the membrane volume fraction of the microemulsion is plotted as a function of the renormalized bending rigidity and homopolymer content. As before, the regions of the lamellar and the three phase coexistence are outlined. The solid line is calculated on the basis of experimental values obtained in [2]. The difference of the slopes of this line and the measured behavior at low Ψ can be caused by increased fluctuations is due to the homopolymer addition. To compare with experiment, the change of bending rigidity due to the homopolymer is evaluated. The respective end-to-end distances and volumes of the homopolymers PEP_5 , PEO_5 were taken into account according to equation 5.7. From the results represented in figure 5.16, which is separated in two subplots for single and double diblock copolymer content, we obtained $\beta = 12 \pm 2$. This agrees nicely with our previous results for the system without diblock copolymer and with results obtained for the $\bar{\kappa}$ from phase diagram measurements.

The dependence of Ψ on κ for different diblock copolymer additions with 0.5% and 1% of homopolymer content is shown in figure 5.17. From equation 2.14 we get the dependence of κ on the diblock copolymer content

$$\frac{\Delta\kappa_R}{k_B T} = -\hat{\Xi}\sigma(R_W^2 + R_O^2) \quad (5.9)$$

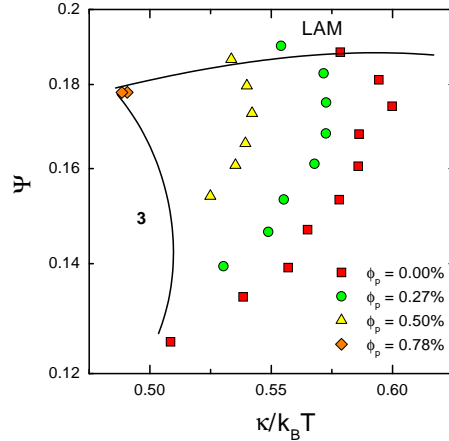


Figure 5.18: *Renormalized bending rigidity vs. membrane content for different addition of polymers, values of κ were calculated by the expression 5.10.*

We can estimate the magnitude of the prefactor $\hat{\Xi}$ with eq. 5.9 by a horizontal cut. The coefficients read $\hat{\Xi}_1 \approx 0.41$, $\hat{\Xi}_2 \approx 0.43$ which compare well with literature $\hat{\Xi} = 0.334$ [45].

The discontinuity of κ at low surface contents Ψ remains open for the discussion. This does not correspond to the phase diagrams. Nonetheless, once a certain amount of homopolymer ($\sim 0.5\%$) is added, the dependence of κ seems to behave normally. This means, that the extracted β and Ξ values correspond to the neat polymer additions. The supposed superposition of the two opposite effects of polymer additions is at least partially fulfilled.

5.2 Discussion

Now we want to discuss a different way to calculate the bending rigidity κ . The scaled correlation length is connected with κ (right part of the figure 5.6, also: fig. 5.7 and 5.18) as follows from the Gaussian random field model [16, 2] (see relation 2.11).

$$\xi S/V = \frac{128}{15\pi} \kappa \quad (5.10)$$

The so obtained bending rigidities are plotted in the same way as before (compare figs. 5.18 and 5.7). The spanned range of κ values has a width of $\Delta\kappa \approx 0.11k_B T$ in either case; just the absolute values are shifted (like $0.42 \leftrightarrow 0.57$). The literature uses the previous expression (eq. 2.9) (see H. Endo [2]), which therefore should be used for comparison in a consistent way.

The scaled domain spacing is approximately constant within the Gaussian random fields model. This does not agree with our measurements (fig. 5.6 left). We observe changes of 8.6% with addition of homopolymer. The fluctuations have a stronger influence on the domain spacing $d(\Psi)$ at smaller surfactant amounts. An expression was given by Roux et al. [46] based on a theory by Helfrich [47]. They give a dependence of the domain spacing:

$$d = \frac{2\delta}{\Psi} \left(1 + \frac{1}{4\pi} \frac{k_B T}{\kappa} \ln \left(c \sqrt{\frac{\kappa}{k_B T}} \frac{d}{2a} \right) \right) \quad (5.11)$$

$c = 1.84$ is a constant for the practical cut-off. $a \approx 7\text{\AA}$ is connected with the area (53.9\AA , [5]) per surfactant molecule. The first factor corresponds to a lamellar structure without fluctuations, the bracket describes fluctuation corrections for lamellar and/or bicontinuous structures. If the whole bracket is assumed to be constant, then one gets $d = 3.2\delta/\Psi = 38\text{\AA}/\Psi$ (using $d = 251\text{\AA}$, $\kappa = 0.42k_B T$). This compares well with the overall experimentally found behaviour (figure 5.13, coefficient 37\AA).

A more detailed discussion on the formula above can be made with the full dependence of κ . Then the dependence of the domain spacing of figure 5.6 (left) can be discussed. With the full homopolymer addition the scaled d increases by 8.6%. The bending rigidity decreases by 30% (conventional evaluation) or 20% (scaled ξ evaluation), which corresponds to an increase of the (scaled) d by 11.5% or 8%. This means that the domain spacing is influenced by the membrane fluctuations, which is relatively clearly observed for high surfactant amounts (and here: high polymer contents). The Gaussian random field theory does not describe this influence within this degree of expansion [2], but higher order terms would allow for a detailed comparison.

Now we focus on the polymer dependence of the bending rigidity κ and the modulus $\bar{\kappa}$: a) The experimental result is that the value $\bar{\beta}$ expresses a 7 times higher sensitivity on the homopolymer content than the theory of Eisenriegler would expect (fig. 5.2). Similarly β is 6.5 times more sensitive (fig. 5.8). Therefore,

both coefficients express the same higher sensitivity. By itself, these findings can be taken as an experimental result. b) The dependence of κ shows a discontinuity between no homopolymer and minimum homopolymer amount at low surfactant concentrations (fig. 5.16). Furthermore, the values of $\bar{\beta}$ are slightly dependent on the presence of diblock copolymer (fig. 5.10). The presence of one and the other polymer slightly changes the behaviour of the microemulsion. However, these changes are so small, that we still claim that the effects of the two polymer types superpose. c) The sensitivity of the phase diagram on the diblock copolymer content (Ξ , see figure 5.11) does not depend on the presence of homopolymer. The dependence of κ on the diblock copolymer content (fig. 5.17) seems to be continuous. Therefore the coefficients $\hat{\Xi}$ agree well for different homopolymer concentrations.

A first trial explanation of the high sensitivity on the homopolymer content might be given by a zone of repulsion (depletion zone) for the homopolymer. Typically, the width of this zone agrees with the radius of gyration, which leaves a smaller available volume for homopolymers. The remaining space $d/2 - 2R_g \approx (125 - 60)\text{\AA}$ measures approximatively half of the distance $d/2$. This factor would yield a 2 times higher effective polymer concentration, which does not fully explain the 7 times higher sensitivity.

Another explanation of the strong sensitivity on the homopolymer content might be given by the studies of T. Auth [48], which have not been published yet. One should compare the end-to-end distance of one dissolved block or homopolymer ($R_{ee} \approx 70\text{\AA}$) with the minimum domain spacing $d/2 \approx 100\text{\AA}$. The polymer is not really confined by the domains, but the polymer is quite close to confinement. Following the simulations of T. Auth, the influence of a *diblock copolymer* on the bending rigidity $\Delta\kappa$ for a confined geometry behaves as follows: For large d one obtains the classical value (eq. 2.14). With values of $d/2 \approx R_g$ (close to the radius of gyration! $R_g = R_{ee}/\sqrt{6} \approx 28.6\text{\AA}$) T. Auth finds a maximum value several times bigger than the classical value. For strongly confined geometries $\Delta\kappa$ becomes quite quickly negative. T. Auth explains this strong decrease of $\Delta\kappa$ by the response of the polymer (monomer distribution) on the curved surface. This response gives a negative contribution to the coefficient for the curvature squared term of the free energy, which means a negative bending rigidity contribution $\Delta\kappa$. For highly confined polymers there should be no difference between anchored polymers (diblock copolymers) and homopolymers. Therefore $\Delta\kappa$ of homopolymers would behave as follows: For large d one would obtain the classical negative value of Eisenriegler, and with decreasing d , $\Delta\kappa$ would become more and more negative. This highly negative values would - in principle - explain the high sensitivity of phase diagrams and the bending rigidity on the homopolymer content (κ , $\bar{\kappa}$). In a detailed discussion, one might find explanations for the apparent "discontinuities" of κ . Just to repeat, the only uncertainty is the range of

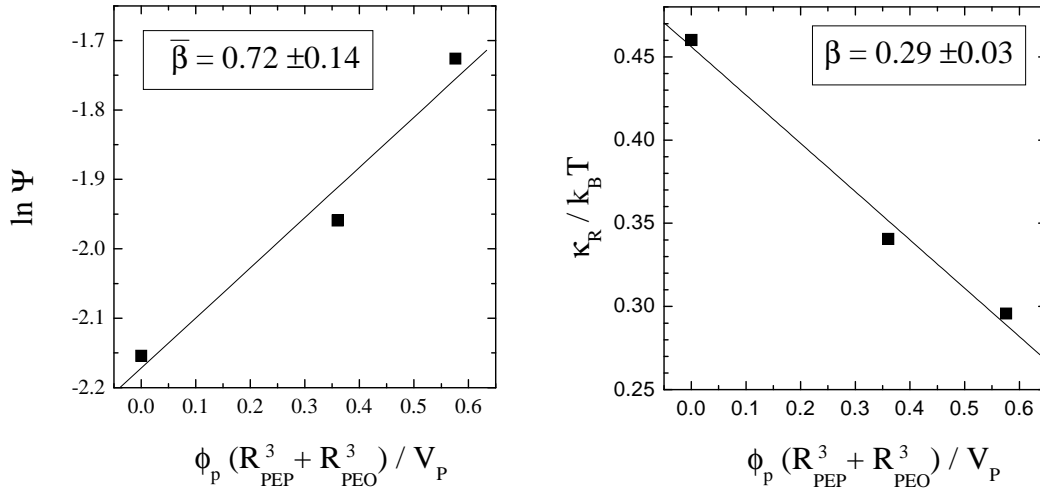


Figure 5.19: *The membrane content at the fish tail point as a function of the scaled homopolymer content (on the left) and the bending rigidity κ as a function of the scaled homopolymer content (on the right).*

confinement ($d/2$), when the scenario described above becomes dominating.

One example of last minute measurements performed by a colleague O. Holderer [49] shows that the homopolymers with higher molecular weight PEP_{10} and PEO_{10} are responsible for an even higher sensitivity of κ and $\bar{\kappa}$. This result would perfectly fit the theoretical picture drawn by T. Auth. The left part of figure 5.19 shows the membrane content at the fish tail point as a function of the scaled homopolymer content. The slope $\bar{\beta} = 0.72$ is 33% larger than the corresponding value with lower molecular weight. In the right part of figure 5.19, the bending rigidity κ is plotted as a function of the scaled homopolymer content. The value of $\beta = 0.29$ is approximately 2 times higher than the reference value of $\beta = 0.15$. These results demonstrate a higher sensitivity of κ and $\bar{\kappa}$ with stronger confinement.

The difference between the two explanations of the high homopolymer sensitivity is that on the one hand the polymer is depleted by the membrane, whereas it is not strongly repelled by the membrane in the other case. Thus question could be solved by detailed contrast variation SANS experiments.

Chapter 6

The droplet phase microemulsion

In this chapter we define a measure of the polymer boosting effect for droplet microemulsions. This is connected with the size of the one phase region in the experimental phase diagram. Furthermore, we investigated the structures of the droplets by SANS and give a connection between the boosting effect and the droplet structure.

6.1 Results

For the investigation of the microemulsion in the droplet phase we used the following components: water(D_2O), nonionic surfactant ($C_{10}E_4$), oil (h-decane/d-

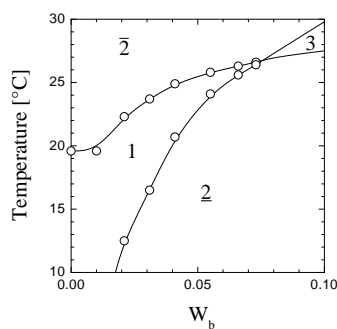


Figure 6.1: *Phase diagram for the droplet phase microemulsion. Materials: H_2O , h-decane and $C_{10}E_4$. W_b is h-decane mass fraction.*

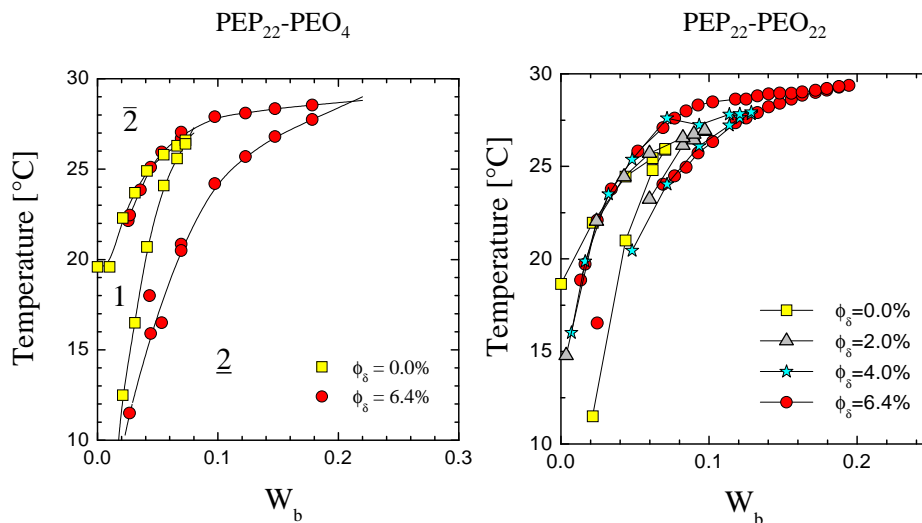


Figure 6.2: The effect of the addition of the diblock copolymer on the maximum amount of solubilized oil. The mass fraction surfactant/water (4/96) is constant for all the samples.

decane) and diblock copolymers (PEP_x-PEO_y) with different molecular weights. Some physical characteristics of the used polymers are collected in [table 7.1](#) and [table 7.2](#). The surfactant/water mass fraction was fixed to 4/96. The maximum amount of oil was limited by the surfactant. Therefore, we took this number as a measure for the efficiency of the surfactant. To describe the content of components in the microemulsion we used $\phi_o = V_{oil}/(V_{oil} + V_{water} + V_{surfactant} + V_{diblock})$, $\phi_\gamma = V_{surfactant}/(V_{surfactant} + V_{diblock} + V_{oil} + V_{water})$ and $\phi_\delta = V_{diblock}/(V_{diblock} + V_{surfactant})$.

The typical phase diagram for the microemulsion consisting of H_2O , decane and $C_{10}E_4$ is shown in figure 6.1. On the x-axis, W_b is the mass fraction of decane in the sample. The region where the droplet microemulsion is stable is indicated by 1. The symbols $\bar{2}$ and $\underline{2}$ indicate the two phase coexistence. At lower temperatures an oil excess phase appears while at higher temperatures a water excess phase appears. When the maximum available oil content is reached all three phases coexist (denoted by 3). The phase boundaries were determined by visual inspection, i.e. by turbidity. The temperature of samples was varied in a thermostated water bath.

Now we discuss phase diagrams with amphiphilic polymer additions. The poly-

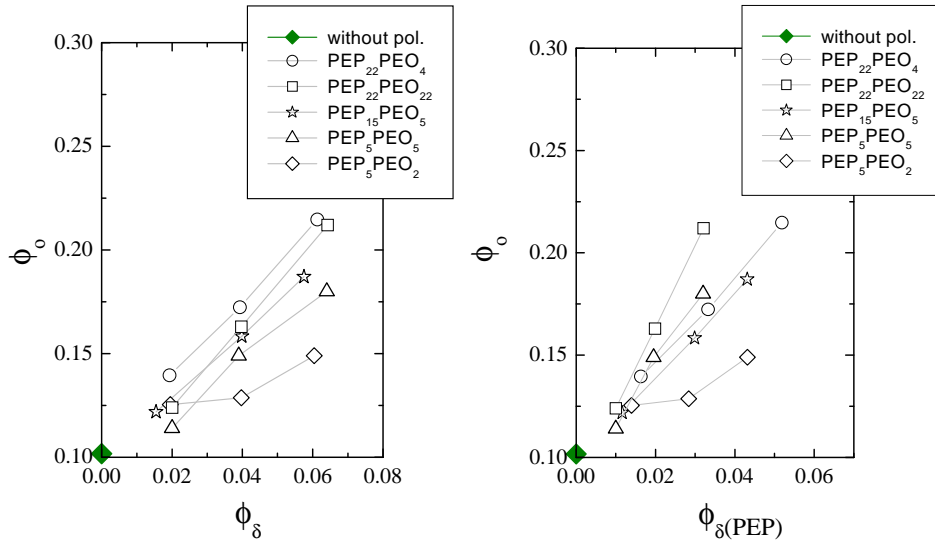


Figure 6.3: *The dependence of maximum amount of oil in microemulsion (*h*-decane/ $\text{C}_{10}\text{E}_4/\text{D}_2\text{O}$) vs. volume fraction of the whole polymer and one block for the different diblock copolymers added.*

mers used were of $\text{PEP}_x - \text{PEO}_y$ type, where x and y denote the molar masses in kg/mol units. On the left part of figure 6.2, we plotted the phase curve for the system without polymer addition and the curve when asymmetric diblock copolymer $\text{PEP}_{22} - \text{PEO}_4$ with a longer oil soluble block was added. This causes an increase of the surfactant efficiency by approximately three times. On the left part of figure 6.2 the phase diagrams of the system for consequent additions of the symmetric diblock copolymer $\text{PEP}_{22} - \text{PEO}_{22}$ is shown. The maximum amount of oil increases continuously. This means a continuous increase of the surfactant efficiency with polymer content. Therefore, amphiphilic block copolymers act similar in droplet microemulsions compared with bicontinuous microemulsions, where the polymers increase the efficiency dramatically.

Phase diagram measurements can provide an answer on the question about the influence of the block- and polymer- length on the upper boundary of emulsified oil in the system. On the left part of figure 6.3, the dependence of the maximum oil content (*h*-decane) in the samples containing different diblock copolymers vs. volume fraction of diblock copolymer ϕ_δ is shown. For every different added polymer, the maximum oil boundary demonstrates a linear dependence of polymer content $\phi_o = (1.7 \pm 0.3)\phi_\delta + \text{const}$, except for the $\text{PEP}_5 - \text{PEO}_2$, which does not fit in this picture. The extrapolation (i.e. the const.) is slightly different for each

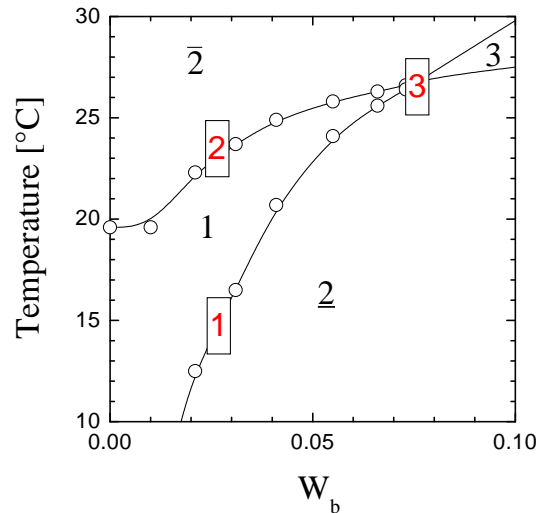


Figure 6.4: *Regions of phase diagram selected for the SANS measurement.*

polymer. This could mean that the different polymers behave similar at high polymer contents. But this remains for later discussion.

On the right part of figure 6.3, the dependence of the maximum oil content on the volume fraction of the oil soluble PEP block ϕ_{δ}^{PEP} is shown for samples with different polymers. All curves for different polymers seem to extrapolate to the same value at low polymer contents, which is explicitly measured. The different slopes indicate a different sensitivity on the PEP content. Whereas here the $PEP_{22} - PEO_{22}$ seems to be rather efficient, it is not in the left plot, where the $PEP_{22} - PEO_4$ is the best polymer booster. This means, that the left plot really characterizes the amount of used additive, whereas the right plot might bring better insight in physics. In either case, the $PEP_5 - PEO_2$ is characterized as a poor efficiency booster.

6.2 SANS

To obtain an information on the droplet size and shape, SANS measurements were performed under bulk and film contrasts. Again, all measurements were done at constant surfactant amount $\phi_{\gamma} = 3.9\%$. The droplet microemulsions were prepared for two cases: a) We chose the maximum oil content. In figure 6.4, this region is marked by box 3. The maximum oil composition ϕ_o varies with the polymer addition. b) The amount of oil was chosen to be rather low,

but big enough to observe the lower temperature boundary visually. This is experimentally hard to observe, since small amounts of excess oil in phase $\underline{2}$ lead to low turbidity. We practically chose $\phi_o \approx 4.5\%$. All b-samples were measured at the minimum and maximum temperatures close to the phase boundaries $\underline{2}$ and $\bar{2}$ (see figure 6.4). These regions are marked with boxes 1 and 2.

6.2.1 Droplets at low oil content and low temperature

The scattering cross section of the samples vs. wave vector for the oil excess (region 1 of the phase diagram) is shown in figure 6.5. The major part of this measurement was performed under bulk contrast with deuterated water D_2O and hydrogenated other components. Some selected samples were prepared under film contrast with deuterated oil (d-decane) and D_2O . The used contrast is indicated in the legend of the figures (b/c - bulk contrast, s/c - shell or film contrast).

Additions of diblock copolymers PEP_xPEO_y cause subtle changes of the shape of scattering curves but the overall shape is a typical spherical droplet structure. An approximately constant Q dependence at low scattering angles ($Q < 0.025$) is the sign that the full particle size is observed at this range. Only the steric repulsion additionally contributes for certain polymer additions. This means a suppressed intensity at low Q , and becomes quite obvious for the $PEP_{22}-PEO_{22}$. The scattering curves under film contrast show a pronounced minimum at $Q \approx 0.065 \text{ \AA}^{-1}$. The position of the minimum gives the approximate radius of the sphere according to $R_{sph} = \pi/Q_{min} \approx 50 \text{ \AA}$. The scattering curves under bulk contrast theoretically have the same minimum. But their minimum is almost smeared out by the polydispersity of the droplet size. It is possible to observe a pronounced minimum under film contrast because the observed polydispersity is related to the surface distribution, while for the bulk contrast the polydispersity is related to the volume distribution.

In order to extract numerical values of parameters from scattering curves they were fitted by the appropriate theoretical model. We used a core-shell model (see eq. 2.72) with sharp boundaries of the scattering length density distribution. To account for size polydispersity, we used the Schultz distribution function for the droplet radius (see eq. 2.80). For large polydispersities, the smearing effects, which are caused by the limited resolution of the instrument should be negligible. From the fits of the scattering intensity we deduced: the mean radius of the droplet $\langle R \rangle$, and the polydispersity parameter ϵ . To reduce the fitting parameters, we have assumed that the shell thickness $\delta = 12 \text{ \AA}$ is a constant. For the values of scattering length density (SLD), we used values of the pure h-decane, d-decane, $C_{10}E_4$, D_2O . It is discussed [50, 51] that the contrast $\Delta\rho$ of the polymer in solvents is modified by the presence of hydrogenous branches. From the

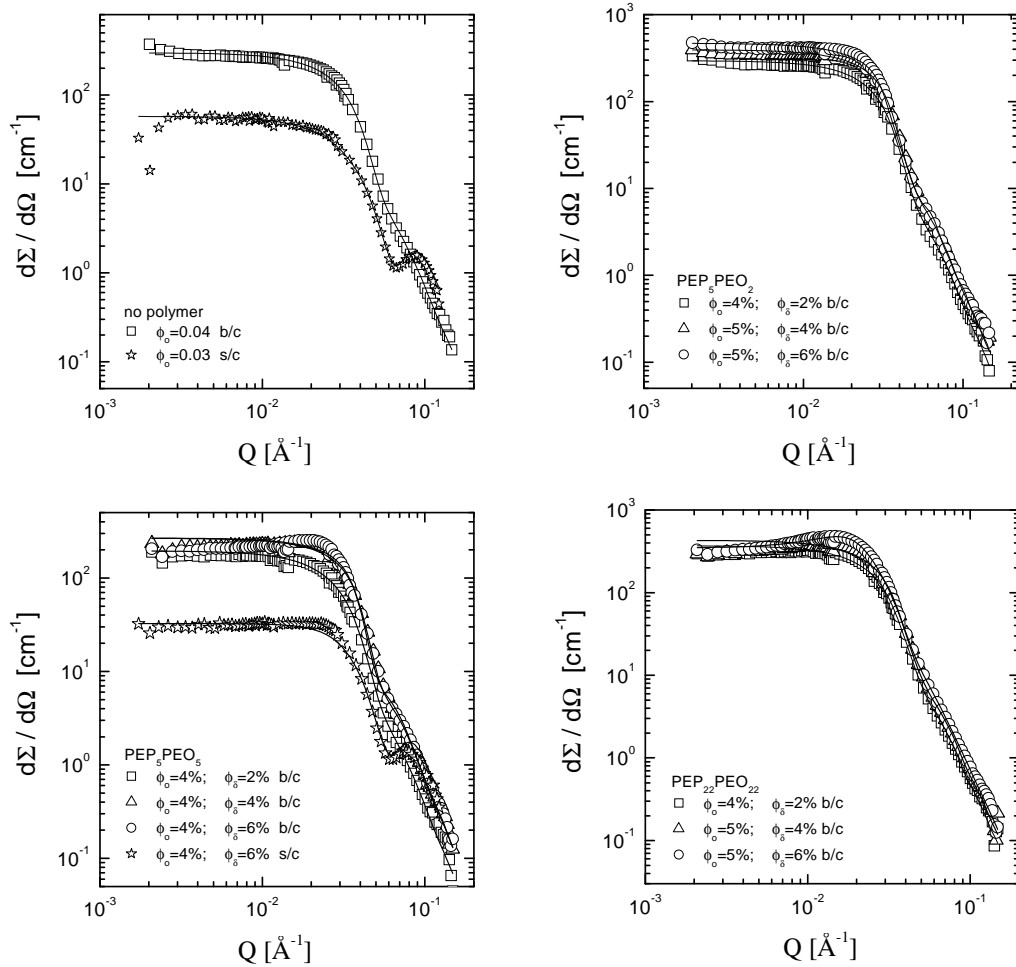


Figure 6.5: *SANS* curves for the microemulsions with low oil content measured at low temperatures. Fitting was performed with the spherical core-shell model. The signs b/c and s/c indicate samples with bulk and shell contrast, correspondingly. The error bars are typically of the symbol size.

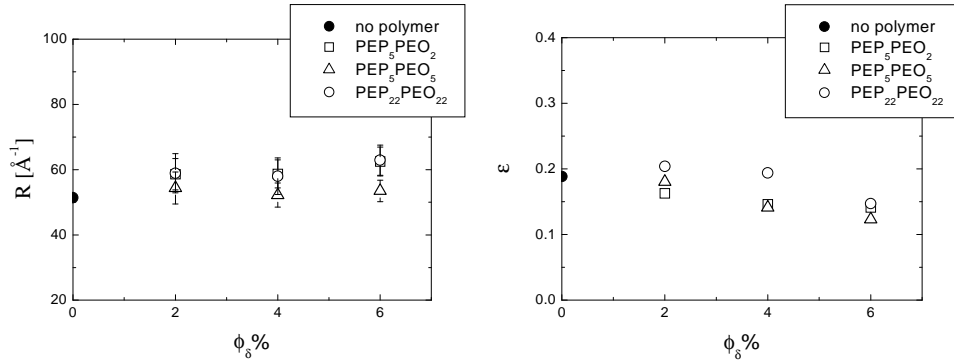


Figure 6.6: *Radius of the spherical droplets and polydispersity obtained from the fitting of SANS curves for the droplet microemulsion at low oil content and low temperature. Errors of the polydispersity are of the symbol size in the plot.*

experimentally obtained polydispersity ϵ_{exp} a corrected value can be obtained by subtracting a value of 10% for the instrumental resolution function [52]. This done by the formula $\epsilon^2 = \epsilon_{exp}^2 - 0.01$. Results of the mean droplet radius and the polydispersity are presented in the plot 6.6. The mean radius of the spherical droplet is approximately constant in the range of experimental errors. So the addition of polymers does not strongly influence the size of the droplets in the low temperature region. The polydispersity decreases slowly with increasing amount of polymer. It is likely that the positive bending rigidity increases by the diblock copolymer anchoring (see eq. 2.14). This in turn decreases the amplitude of the $l = 0$ fluctuations (see eq. 2.43), which is connected to the polydispersity in the system.

Another option to obtain the radius of spherical droplets is the Porod law, or the constraint conditions for the total volume and interfacial area in the system. The Porod behaviour at large scattering angles yields a coefficient, which is characteristic for the surface per volume, i.e. $d\Sigma/d\Omega \sim S/VQ^{-4}$. We made this coefficient independent on the neutron contrast by the Porod invariant (see in [53]), which is calculated after $Q_{inv} = \int d\Sigma/d\Omega Q^2 dQ$. Assuming spherical particles we obtain, $S/V = 3\phi/R$ (see eq.2.50 with condition that only perfect spheres are present $\psi_c = 0$). The volume fraction of the droplets is obtained by adding the two components oil ϕ_o and surfactant $\phi_\gamma/2$. Within the geometrical picture the radius of the droplets reads: $R_{geom} = 3d \frac{\phi_o + \phi_\gamma/2}{\phi_\gamma}$ (as in eq. 2.51). In table 6.1 the so obtained parameters of the spherical droplet phase microemulsion are summarized. All radii basically agree well. The errors lie in the range of $\pm 5\text{\AA}$. Also

Table 6.1: *Spherical droplet parameters. All units base on \AA , which means $[S/V]=\text{\AA}^{-1}$ and $[R_x]=\text{\AA}$. S/V and R_{Porod} are obtained from Porod law, R_{geom} from constraint conditions, and R_{SANS} by model fitting (see eq. 2.72). ϵ is corrected for experimental resolution.*

polymer	ϕ_δ	S/V	R_{Porod}	R_{geom}	R_{SANS}	ϵ	N_{pol}/N_{dr}
without polymer	0	0.0024	50.6	54.5	51.4	0.19	0
PEP_5PEO_2	0.02	0.0019	71.2	58.3	58.6	0.16	1
	0.04	0.0023	59.6	60.3	58.7	0.15	2.1
	0.06	0.0025	59.8	63.6	62.5	0.14	3.7
PEP_5PEO_5	0.02	0.0019	62.8	54.7	54.4	0.18	0.5
	0.04	0.002	59.0	54.4	52.2	0.14	1
	0.06	0.002	59.3	55.3	53.5	0.12	1.8
$PEP_{22}PEO_{22}$	0.02	0.002	63.0	56.1	58.9	0.20	0.1
	0.04	0.0022	61.2	59.9	58.0	0.19	0.3
	0.06	0.002	71.1	63.8	62.9	0.15	0.5

the polydispersity parameter and number of polymers per droplet N_{pol}/N_{dr} were included in the table. We can conclude that the structure of the oil droplets does not depend on the polymer addition (for the mentioned polymers) in the region of low oil contents and low temperatures (region 1). The size polydispersity might indicate the increasing bending rigidity with higher polymer content.

6.2.2 Bidisperse objects - low oil content and low temperature

Not for all samples at low oil contents and low temperatures we observed pure spherical shapes. We will show, that bidisperse objects are obtained for the diblock copolymers $PEP_{15} - PEO_5$ and $PEP_{22} - PEO_4$. A possible explanation could be the coexistence of oil droplets with polymer micelles. This could be connected with the fact that the end-to-end distance R_{ee} of the oil soluble block is comparable with the radius of the droplet. Figure 6.7 shows the macroscopic cross section as a function of the scattering vector Q for the polymer $PEP_{15} - PEO_5$ and $PEP_{22} - PEO_4$ with varying polymer contents. Very clearly (bulk contrast), bidisperse structures show up for the $PEP_{22} - PEO_4$ with $\phi_\delta = 6\%$. For the bulk contrast, two decays of the intensity occur at $Q \approx 0.015$ and $Q \approx 0.04$, which is an indication of bidisperse structures. For the film contrast, the first decay is almost invisible, which means that the larger particles have much less surfactant

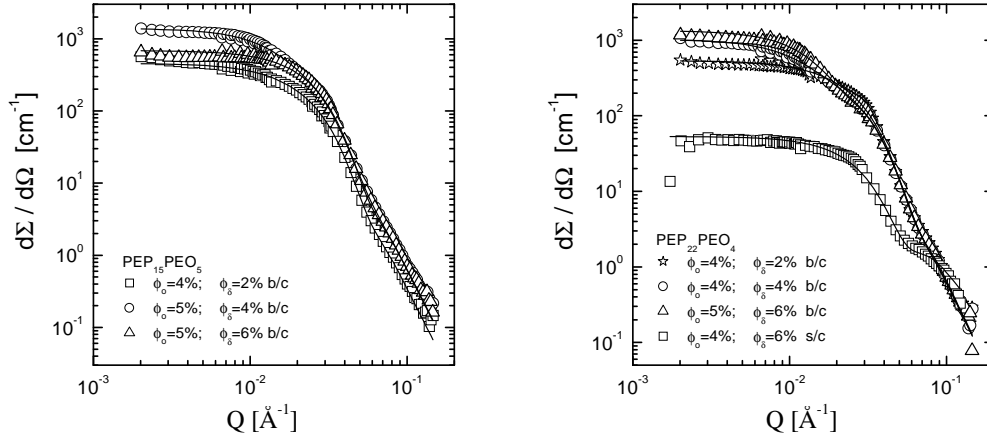


Figure 6.7: *SANS curves for the microemulsions with low oil content measured at low temperatures. Fitting was performed with the spherical core-shell model with two different particle sizes. The signs b/c and s/c indicate samples with bulk and shell contrast, correspondingly. The error bars are typically of the symbol size*

than the smaller ones. This would speak for polymer micelles coexisting with conventional spherical droplets. For this example we obtain radii of $R_2 = 149\text{\AA}$ and $R_1 = 51\text{\AA}$. The smaller radius lies in the range of the conventional spherical droplets.

6.2.3 Droplets at low oil content and high temperature

We will now discuss the droplet structure at low oil content and high temperature, i.e. at water excess (region 2 of the phase diagram (see Fig.6.4)). In the theory part it is qualitatively shown that the droplet phase microemulsion with varying composition parameters and temperature can have a transition from the spherical shape of domains to the cylindrical shape. We will show, that this shape transition occurs with increasing temperature. A characteristic feature of cylindrical structures is a q^{-1} -dependence at low scattering angles ($0.002\text{\AA}^{-1} < q < 0.017\text{\AA}^{-1}$) as shown in figure 6.8. The decay at higher q -range is caused by the radial structure of the cylinders. From this part of q -range, it is possible to apply the Porod law to obtain the surface to volume ratio S/V of

the interface with enclosed volume. The surface to volume ratio and the assumption of cylindrical geometry (based on the shape of SANS curves) allow for the estimation of the radius of the cylindrical domains. The length of the cylinders cannot always be extracted from the scattering data in the accessible range of wave vector q , ($q > 0.002\text{\AA}^{-1}$), as indicated by the missing plateau at small q (Guinier behavior). The film contrast measurement without polymer shows quite low intensity. We have no explanation for this behavior.

The the minimum of the formfactor describing the radial shape or simply the radius is smeared out by the polydispersity of the core radius. The addition of polymer does not strongly influence on the core radius within the accuracy of the measurement. To fit the SANS data, the core-shell cylindrical model was used (see eq. 2.78). To take in account the polydispersity of the cylinder radius, we used a Schultz distribution function (see eq. 2.80). From the fits of the absolute scattering intensity we deduced: the mean radius of the cylinders $\langle R \rangle$, and the polydispersity parameter ϵ . To reduce the fitting parameters, we have assumed that the shell thickness $\delta = 12\text{\AA}$ is a constant.

In table 6.2, the parameters obtained for the microemulsion with cylindrical shape of oil domains are summarized. The radii of cylinders were obtained by two different methods: 1) From Porod law and constant thickness of the surface, with assuming the geometry of cylinder. 2) From fitting of the scattering data. Similarly to the spherical droplet microemulsion, we obtain for the Porod constant of cylinders: $S/V = 2\phi/R$ (see eq. 2.50 with $\psi_s = 0$). Also the polydispersity parameter ϵ for radius distribution was included in the table. The radius and its polydispersity of the cylinders are shown in figure 6.9 as a function of polymer content for different polymers. The radius without polymer and with $PEP_5 - PEO_5$ agrees well in comparison with the spherical droplets, according to $R_{cyl} = \frac{2}{3}R_{sph}$. For the other polymers: $PEP_5 - PEO_2$, $PEP_{15} - PEO_5$ and $PEP_{22} - PEO_4$, the cylinder radius is significantly bigger than this estimation. Since the radii obtained by the different methods agree, this deviation seems to be real. The polymer seems to demand more space in the cylinder. Nonetheless, the shape of the droplets at low oil contents and high temperatures (region 2) does not strongly depend on the polymer addition. There are subtle changes of the radii for different polymers. There are changes of the cylinder length with polymer addition. Large numbers ($L \approx 2000\text{\AA}$) are taken as lower limits for the real length, since the Guinier behaviour is missing then. The polydispersity mainly seems to be constant for all samples.

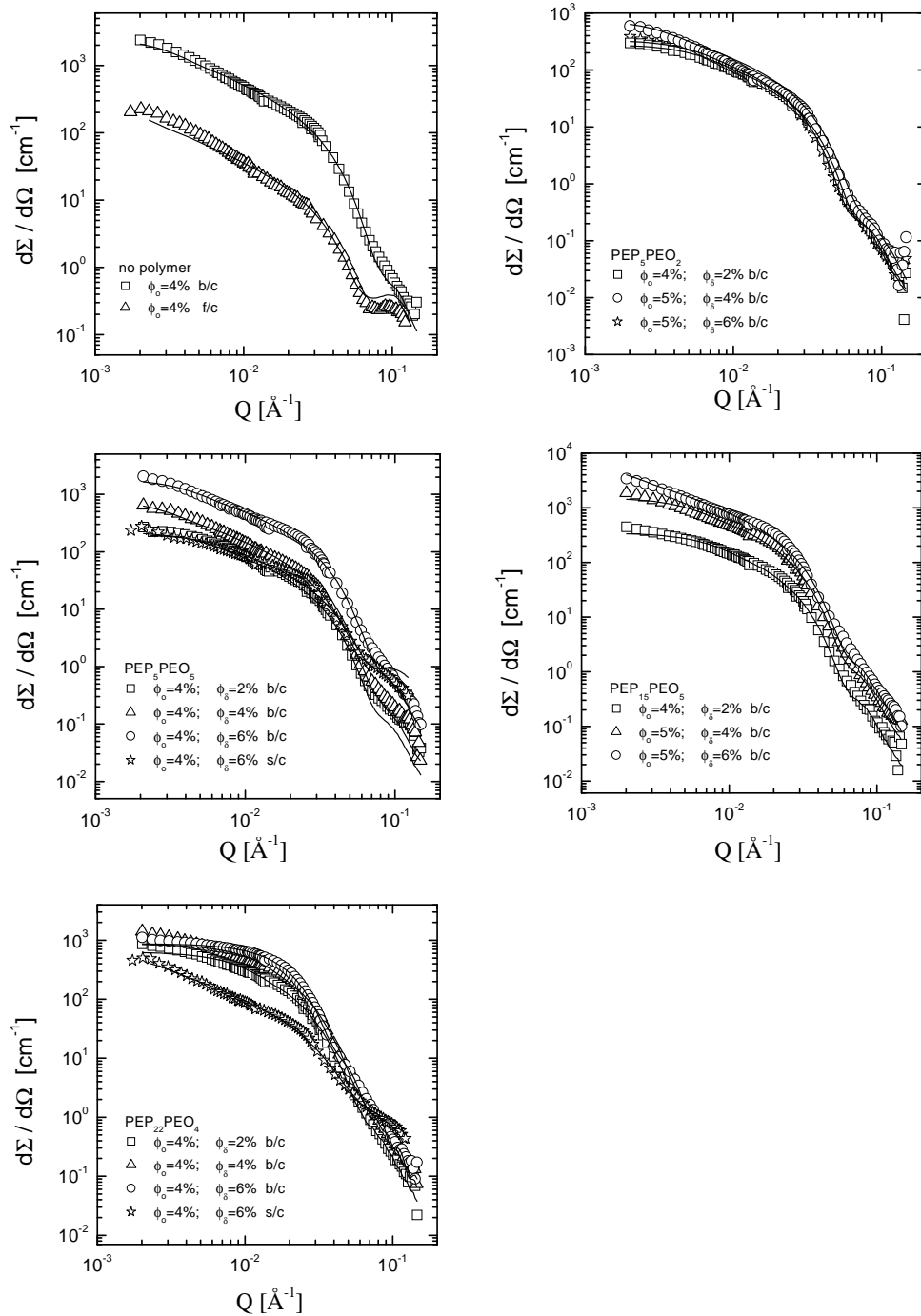


Figure 6.8: SANS curves for the microemulsions with low oil content measured at high temperatures. Fitting was performed with the cylindrical core-shell model. The signs b/c and s/c indicate samples with bulk and shell contrast, correspondingly. The error bars are typically of the symbol size

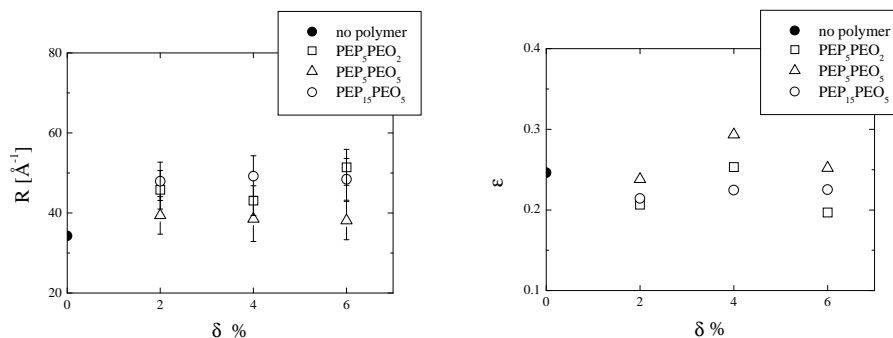


Figure 6.9: Radius of the cylindrical droplets and polydispersity obtained from the fitting of SANS curves for the droplet microemulsion at low oil content and high temperature. Errors of the polydispersity are of the order of the symbol size in the plot.

6.2.4 Droplets at high oil contents

As was shown by the phase diagram measurements (see fig.6.2), the addition of diblock copolymer to the microemulsion causes a big shift of the solubilization limit with increasing oil content. So it is quite interesting to investigate the morphology of such system by SANS. This can provide some insight on the physics of the 'boosting effect' in case of the relatively small amount of oil (droplet phase microemulsion). We will show that the structures are either cylindrical or ellipsoidal. The evaluation of the cylindrical structures is straight forward, since we use the same theories as before. More effort will be spent with the ellipsoidal structures. The macroscopic cross section as a function of the scattering angle is shown in figure 6.10 for cylindrical structures. For samples without polymer and with $PEP_5 - PEO_2$ addition, the radii of the cylinders are much bigger at the maximum oil concentration compared with low amount of oil (see table 6.3).

The major part of polymer additions at the maximum oil content leads to ellipsoidal. The scattering cross section vs. wave vector for this part is shown in figure 6.11. The used contrast is indicated in the legend of the figures. The film contrast measurement without polymer shows quite low intensity. We have no explanation for this behavior.

To model the SANS data, we used a core-shell ellipsoid of revolution model (see eq. 2.74). This was motivated by the spherical-like shapes of scattering curves. Just to describe the scattering at low Q , we needed an ellipsoidal shape model.

Table 6.2: *Cylindrical droplet parameters. System is at low oil content and at the high temperature. All units base on \AA , which means $[S/V]=\text{\AA}^{-1}$, $[R_x]=\text{\AA}$ and $[L]=\text{\AA}$. S/V and R_{Porod} obtained from Porod law and R_{SANS} by model fitting (see eq. 2.78). ϵ is corrected for experimental resolution.*

polymer	ϕ_δ	ϕ_{oil}	S/V	R_{Porod}	R_{SANS}	L_{SANS}	ϵ
no polymer	0	0.04	0.0019	42.6	34.3	1424	0.25
PEP_5PEO_2	0.02	0.044	0.0018	49.3	45.8	713	0.21
	0.04	0.046	0.0022	41.7	43.1	1782	0.25
	0.06	0.049	0.0014	67.6	51.4	764	0.20
PEP_5PEO_5	0.02	0.040	0.0015	52.0	39.4	765	0.24
	0.04	0.040	0.0015	53.4	38.5	1525	0.29
	0.06	0.041	0.0018	46.4	38.1	1056	0.25
$PEP_{15}PEO_5$	0.02	0.045	0.0021	43.3	47.9	576	0.21
	0.04	0.050	0.0018	55.0	49.2	789	0.22
	0.06	0.053	0.0022	49.6	48.4	2246	0.23
$PEP_{22}PEO_4$	0.02	0.045	0.0021	42.7	48.4	485	0.25
	0.04	0.045	0.0015	61.7	48.2	384	0.28
	0.06	0.049	0.0022	44.0	63.0	199	0.32

Table 6.3: *Cylindrical droplet parameters. System is at maximum oil content. All units base on \AA , which means $[S/V]=\text{\AA}^{-1}$, $[R_x]=\text{\AA}$ and $[L]=\text{\AA}$. S/V and R_{Porod} obtained from Porod law, R_{geom} and R_{SANS} by model fitting (see eq. 2.78). ϵ is corrected for experimental resolution.*

polymer	ϕ_δ	ϕ_{oil}	S/V	R_{Porod}	R_{SANS}	L_{SANS}	ϵ
no polymer	0	0.102	0.0026	80.8	83.5	1341	0.25
PEP_5PEO_2	0.02	0.125	0.0023	107.7	84.9	2022	0.27
	0.04	0.129	0.0020	127.5	110.3	1732	0.25
	0.06	0.149	0.0023	130.9	108.7	523	0.32

Polydispersity ϵ of ellipsoids was accounted for with the Schultz distribution function (see eq. 2.80).

In table 6.4 the parameters obtained for the ellipsoidal sphere-like model are represented. The radius of the droplets was obtained by three different methods: 1) From Porod law including constant thickness of the surfactant layer. Here we assumed the droplet to have the shape of a sphere. 2) Calculating radius from the

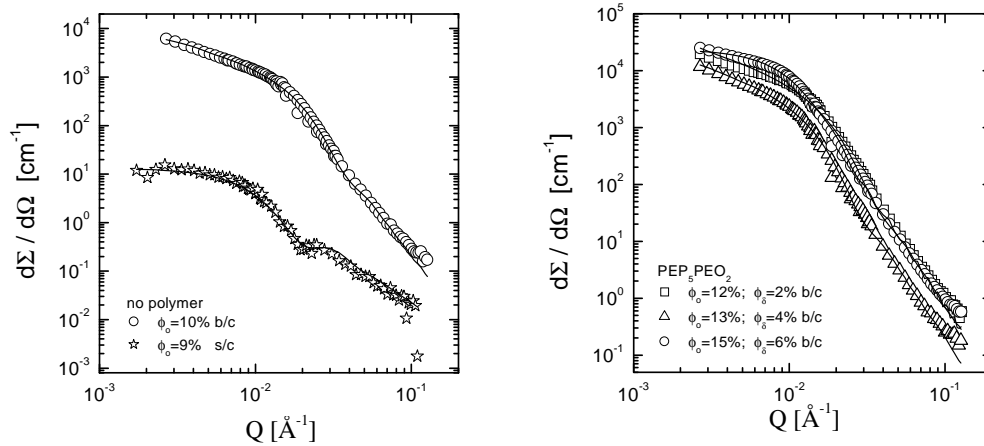


Figure 6.10: *SANS curves for the microemulsions with high oil content. Fitting was performed with the cylindrical core-shell model. The signs b/c and s/c indicate samples with bulk and shell contrast, correspondingly. The error bars are typically of the symbol size*

composition of the sample also assuming constant thickness of the surfactant layer and spherical geometry of droplets. 3) From the model fitting of the scattering data with the elliptical model. Also the polydispersity parameter ϵ for the radius distribution, the axis ratio ϵ and the number of polymers per droplet N_{pol}/N_{dr} were included.

From the SANS radius and number of polymers per droplet N_{pol}/N_{dr} we are able to classify the grafting behavior of the polymer (see Fig. 2.5). Even the most dense covered droplets still belong to the mushroom regime. So the influence of the polymer addition on the bending rigidity should be described by the classical theories in the mushroom regime [19] (see eq. 2.14, 2.15).

To compare these predictions, we can estimate the effect of polymer addition on the bending modulus of membrane by using the theory for the droplet shape fluctuations [23]. It gives the connection between the two experimentally observable parameters polydispersity ϵ and ratio of ellipsoid axes ϵ with fluctuation modes of the droplets (see eqs. 2.38, 2.40). That is on the other hand connected with the bending modulus. The calculated fluctuation modes $\langle |u_{00}|^2 \rangle$ and $\langle |u_{20}|^2 \rangle$ are shown in table 6.5. The general tendency, which is clearly extracted from the experiment, is the fast decrease of the mode $\langle |u_{20}|^2 \rangle$ (see eq. 2.44), which corre-

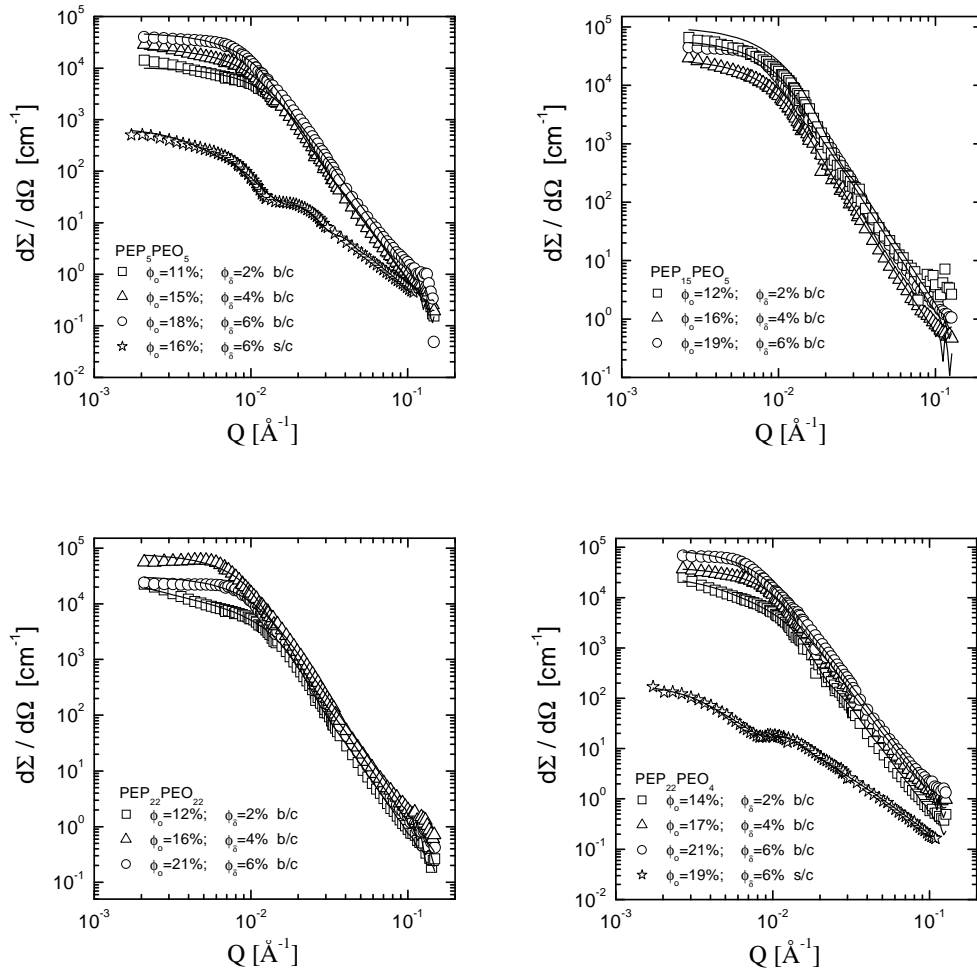


Figure 6.11: SANS curves for the microemulsions with high oil content. Fitting was performed with the ellipsoid of revolution, core-shell model. The signs b/c and s/c indicate samples with bulk and shell contrast, correspondingly. The error bars are typically of the symbol size

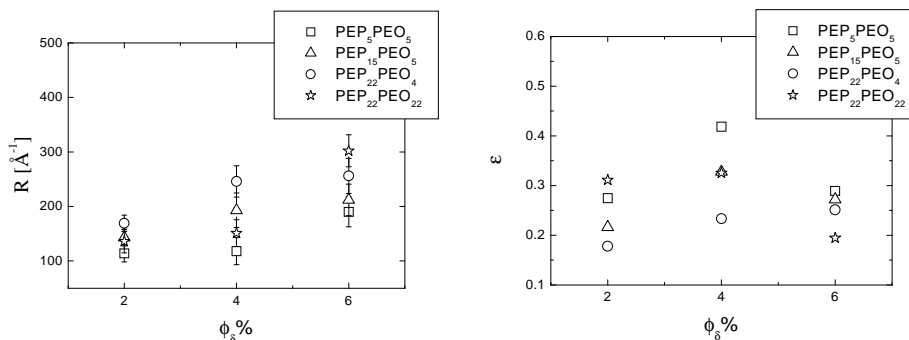


Figure 6.12: Radius of the elliptical droplets and polydispersity obtained from the fitting of SANS curves for the droplet microemulsion (see eq. 2.74) at high oil content. Errors of the polydispersity are of the order of the symbols size in the plot.

sponds to the most probable peanut deformation of the droplets [23]. This causes the stabilization of the droplet shape and indicates an increase of the bending rigidity of the membrane. These two factors indicate increased emulsification properties of the surfactant.

6.3 Discussion

We defined the maximum amount of oil, which is allowed for a certain amount of surfactant/water, as a measure for the boosting effect. The dependence of this number is given in figure 6.3 as a function of the diblock and the PEP block content for several polymers. The left plot shows the dependence on the whole additive amount, which is important for the final application. Both plots characterize the $PEP_5 - PEO_2$ polymer as a bad efficiency booster.

We measured the droplet structure at three regions in the phase diagram (see table 6.6). For low oil content and low temperature (region 1), we mainly observe spherical droplets. From the repulsive structure factor one observes that the longer the water soluble PEO block is, the higher the repulsive interaction is. Therefore, the outer block seems to have some influence on the effective potential. All droplet radii are constant within experimental error. They agree well between the different evaluation methods. Therefore, we claim that only the surfactant determines the structure and size of the droplet in this region of the

Table 6.4: *Ellipsoid parameters. System is at maximum oil content. All units base on \AA , which means $[S/V]=\text{\AA}^{-1}$ and $[R_x]=\text{\AA}$. S/V and R_{Porod} obtained from Porod law, R_{geom} from constraint conditions, and R_{SANS} by model fitting (see eq. 2.74). ϵ is corrected for experimental resolution. ε is the axis ratio.*

polymer	ϕ_δ	ϕ_o	R_{Porod}	R_{geom}	R_{SANS}	ϵ	ε	N_{pol}/N_{dr}
PEP_5PEO_5	0.02	0.114	152	131	114	0.29	1.45	4.3
	0.04	0.149	195	172	118	0.43	0.98	9.9
	0.06	0.18	226	212	190	0.31	1.05	27.2
$PEP_{15}PEO_5$	0.02	0.122	214	140	143	0.24	1.86	2.7
	0.04	0.159	220	183	193	0.34	0.88	5.8
	0.06	0.187	206	220	212	0.29	1.12	15.7
$PEP_{22}PEO_4$	0.02	0.14	188	161	169	0.2	3.17	5.4
	0.04	0.173	196	202	246	0.25	1.25	7
	0.06	0.215	252	259	256	0.27	1.09	16.2
$PEP_{22}PEO_{22}$	0.02	0.041	99	56	62	0.35	1.57	0.2
	0.04	0.045	112	60	109	0.24	0.77	0.2
	0.06	0.049	82	64	104	0.28	0.97	0.5
$PEP_{22}PEO_{22}$	0.02	0.124	158	143	136	0.33	6.00	4.5
	0.04	0.163	208	183	151	0.34	1.16	3
	0.06	0.213	271	256	302	0.22	1.09	8.9

phase diagram. The polydispersity ϵ goes down with increasing polymer content. This subtle change is connected with the bending rigidity, which suppresses fluctuations of the mean droplet radius ($\langle |u_{00}|^2 \rangle$ mode).

Nonetheless, we also found bidisperse structures in the region 1 for polymers with longer oil soluble *PEP* blocks (compared to the *PEO* blocks), i.e. for the $PEP_{15} - PEO_5$, and the $PEP_{22} - PEO_4$. We interpreted this occurrence with neat droplets as we have seen before and larger polymer micelles with only small amounts of surfactant (the film contrast shows mainly the small droplets). The radius of the neat droplet agrees well with the other measurements of region 1. The radius of the polymer micelles (149\AA) is rather small compared with "pure" polymer micelles [51]. The small amounts of surfactant in the micelle must have reduced the surface tension of *PEP* vs. water. For these polymers, the embedding of the *PEP* block in the oil droplet must be unfavourable compared with the micelles.

For low oil contents and high temperatures (region 2), we mainly observe cylindrical structures. The radii obtained by the SANS modelling do not agree as well as before (spheres) with the Porod evaluation. The radii of the samples

Table 6.5: *Fluctuations modes*

polymer	ϕ_δ	ϕ_o	$\langle u_{00} ^2 \rangle$	$\langle u_{20} ^2 \rangle$
PEP_5PEO_5	0.02	0.114	0.94839	0.01133
	0.04	0.149	2.20144	0.00002
	0.06	0.18	1.05207	0.00022
$PEP_{15}PEO_5$	0.02	0.122	0.58833	0.02953
	0.04	0.159	1.64926	0.00123
	0.06	0.187	0.93033	0.00104
$PEP_{22}PEO_4$	0.02	0.14	0.39794	0.09856
	0.04	0.173	0.68507	0.00362
	0.06	0.215	0.79159	0.00059
$PEP_{22}PEO_{22}$	0.02	0.041	1.42574	0.01832
	0.04	0.045	0.61791	0.00414
	0.06	0.049	0.85608	0.00005
$PEP_{22}PEO_{22}$	0.02	0.124	1.21690	0.27026
	0.04	0.163	1.33046	0.00192
	0.06	0.213	0.47560	0.00054

without polymer and with $PEP_5 - PEO_5$ correspond to the spherical droplets. Here the surfactant dominates the cylindrical droplet size and shape. For the polymers $PEP_5 - PEO_5$, $PEP_{15} - PEO_5$, and $PEP_{22} - PEO_4$, the radii are slightly elevated. The polymer seems to demand more space here. But still the shape of the droplets seems to be dominated by the surfactant. The cylinder lengths L behave not very systematic. Only for the $PEP_{22} - PEO_4$ polymer, the length seems to decrease systematically with increasing polymer content. For the $PEP_{22} - PEO_{22}$, the shape is not cylindrical anymore. We had to use the ellipsoidal model in this case.

For the maximum oil content (region 3), we observe either cylindrical or ellipsoidal structures. For the samples without polymer and with $PEP_5 - PEO_2$, we observe cylinders with large radii. This feature seems to be connected with the weak efficiency boosting of the $PEP_5 - PEO_2$ (see fig. 6.3). We want to stress, that the length of the cylinder decreases with increasing polymer content, which seems to be connected with the higher slope of the maximum oil content versus polymer addition (see fig. 6.3). This seems to be an onset of polymer boosting which is connected with the shortening of the cylinder. The same explanation might hold for the samples with polymers $PEP_{22} - PEO_4$ and $PEP_{22} - PEO_{22}$ in region 2 of the phase diagram.

For the remaining polymers ($PEP_5 - PEO_5$, $PEP_{15} - PEO_5$, $PEP_{22} - PEO_{22}$, and $PEP_{22} - PEO_4$) we observe ellipsoidal shapes. All of these polymers are

Table 6.6: *Droplet structures*

Polymer	Region	Structure
No polymer	1	Sphere
	2	Cylinder
	3	Cylinder (larger diameter)
PEP5PEO2	1	Sphere
	2	Cylinder(shorter)
	3	Cylinder (larger diameter)
PEP5PEO5	1	Sphere (slightly repulsive)
	2	Cylinder(shorter)
	3	Ellipsoid revolution
PEP15PEO5	1	Bidisperse: Spheres+pol. Micelles
	2	Cylinder
	3	Ellipsoid revolution
PEP22PEO22	1	Sphere (repulsive)
	2	Ellipsoid revolution
	3	Ellipsoid revolution
PEP22PEO4	1	Bidisperse: Spheres+pol. Micelles
	2	Cylinder (shorter)
	3	Ellipsoid revolution

responsible for a strong boosting effect. The radii of different model evaluations partially deviate (but e.g. the assumption of a sphere for the Porod constant is wrong). The axis ratio ε at the maximum polymer content is generally smaller than ε at low polymer content. The idea of the shortening of the cylinder length continues here: The stronger the polymer boosting, the shorter the long axis (or the more spherical) the droplet is. This is also expressed by the amplitude $\langle |u_{20}|^2 \rangle$. Some problems arise when we try to obtain numerical values for the bending rigidity and saddle splay modulus of elliptical droplets. The estimated values come up with some tens of $k_B T$. A possible explanation could be the osmotic pressure of the encapsulated polymer. Another reason might be, that we measure quite close to the emulsification boundary and not far away from the upper phase boundary at high temperatures. The theory for fluctuating droplets mainly applies to the case of low temperatures which is not true for the region 3. So despite this, the theory gives a qualitative insight in the process of droplet shape formation.

Therefore, the structures (and partially sizes) at low oil contents are mainly determined by the surfactant. At high oil contents the polymer boosting is con-

nected with the droplet shape. The boosting polymer tends to drive the axis ratio towards 1.

The dominance of the surfactant for the microemulsion structure partially applies also in the bicontinuous case. The domain spacing (see figure 5.13) is determined by the surfactant, mainly, whereas the correlation length is also influenced by the bending rigidity and therefore by the polymer addition.

Table 6.7: *Comparison of our measurements with literature [54]: concentrations and temperatures for the droplet microemulsion with addition of $PEP_5 - PEO_5$ diblock copolymer together with the measured radius, polydispersity, and fluctuation modes describing size and shape fluctuations.*

	Low oil content, low temperature	data from [54]	Max oil content
ϕ_γ	0.039	0.041	0.033
ϕ_δ	0.063	0.102	0.062
ϕ_O	0.041	0.058	0.180
T [°C]	15.5	21.0	26.9
R [Å]	54	88	190
ϵ	0.12	0.18	0.31
$\langle u_{00} ^2 \rangle$	0.18	0.41	1.05
$\langle u_{20} ^2 \rangle$	–	0.038	0.00022

Now we want to compare our measurements with literature. In table 6.7 our values for averaged radius R , polydispersity ϵ and shape fluctuations $\langle |u_{00}|^2 \rangle$, $\langle |u_{20}|^2 \rangle$ are listed and compared with values obtained in [54] for $PEP_5 - PEO_5$ polymer addition. The data are sorted by the amount of oil (ϕ_O), whereas the surfactant amount (ϕ_γ) and polymer amount (ϕ_δ) are almost constant. With increasing amount of oil, the selected temperature was minimal, medium and restricted by the phase diagram. With the increasing oil amount the average radius and polydispersity increase correspondingly. The growth of the fluctuation mode $\langle |u_{00}|^2 \rangle$ describing droplet size fluctuations agrees nicely with the picture of size and shape fluctuations with changing droplet size R (see eqs. 2.41, 2.42). The shape fluctuations mode $\langle |u_{20}|^2 \rangle$ depends in the opposite manner, which correctly agrees with this picture. Only at the minimum oil concentration we did not find a corresponding value. In this work we focused on the minimum temperature, where fluctuations are minimal. A corresponding medium temperature would allow for larger shape fluctuations, but non-published measurements show: a competition of the repulsive structure factor with shape fluctuations at small Q , and due to

the selected bulk contrast strong smearing of the formfactor minimum, which does not allow for a detailed analysis of shape fluctuations.

Chapter 7

Summary and Conclusions

We investigated microemulsions consisting of water, oil, nonionic surfactant and various polymers by two complementary methods: we studied the macroscopic phase behavior, and the corresponding microscopic structure was obtained by SANS measurements. The main aim of our work was to get a deeper insight in effects caused by small additions of polymers to the microemulsions. After the polymer boosting effect has been established - this is a strong enhancement of the emulsification behavior by addition of amphiphilic diblock copolymer - the complementary effect of homopolymers was under consideration now. Simultaneous addition of homopolymers and diblock copolymer were investigated to check if the two opposite effects are superposable and if one can get a constant efficiency with changed viscosity. Then the boosting effect was transferred from the bicontinuous to the droplet microemulsion. In this part of experiments, amphiphilic diblock copolymers with different chain lengths and chain length ratios were used in order to study the link between the strength of the boosting effect and diblock copolymer structure.

First, we added homopolymers to the bicontinuous microemulsion, only. We used equal amounts of water- and oil-soluble polymers with the same molecular weight. The phase behavior in this case demonstrated a diminished efficiency of the surfactant. The sensitivity of the phase diagram on the homopolymer addition is connected with the saddle splay modulus and therefore can be compared with theory. By SANS we measured the microscopic structure of the microemulsion. Describing the scattering data with the Teubner-Strey formula we obtained the structural parameters of the microemulsion: the characteristic domain size d and the correlation length ξ . The Gaussian random field model allows to extract the elastic modulus κ from the structural parameters. We observed the decrease of the bending rigidity κ with increasing homopolymer content. The sensitivity of the emulsification ability and of κ on the homopolymer content is about 7 times

stronger than predicted by theory. This high sensitivity agrees with the phase boundary measurements. In future it has to be discussed whether the confinement of the polymer between the membranes is responsible for this high sensitivity.

Then we focused on the simultaneous addition of homopolymers and diblock copolymer. The phase diagram indicates that the diblock copolymer increases the efficiency while the homopolymer decreases it. The connection of the emulsification boundary with saddle splay modulus $\bar{\kappa}$ leads to the deduction that $\bar{\kappa}$ increases by the homopolymer addition and decreases by the addition of diblock copolymer. Again the SANS measurements allow for the determination the structural parameters d and ξ . The bending modulus κ is calculated. Addition of the homopolymer decreases κ while the addition of diblock increases it. For this simultaneous addition of polymers, the sensitivity of κ and $\bar{\kappa}$ on the homopolymer addition is the same as in the case of neat homopolymer addition. Also the effect of diblock copolymer addition is in good agreement with results obtained in other work [2]. This brought us to the conclusion that these both opposite effects act independently in the studied range of polymer concentrations. So, this behavior allows for the change of viscosity at constant surfactant efficiency.

The other part of our work is dedicated to the droplet phase microemulsion, to which the boosting effect was to be transferred. The phase diagram shows us that the one phase region of the droplet microemulsion is extended by the block copolymer addition. As a characteristic number for the strength of boosting we took the maximum oil content of the one phase system at fixed amount of surfactant. In detail, we studied polymers with different chain length and chain length ratios. Using SANS, we measured the structure of the droplet microemulsion at three different points in the phase diagram in the one phase region. 1) Low oil content and low temperature, 2) Low oil content and high temperature, 3) Maximum amount of oil. At region 1 mainly spherical droplets form. Only $PEP_{22}-PEO_4$ and $PEP_{15}-PEO_5$ gave bidisperse spherical structures. At point 2 mainly cylindrical structures were found except for $PEP_{22}-PEO_{22}$. At point 3 for the samples without polymer and with PEP_5-PEO_2 cylindrical structures formed. Longer polymers, which cause a stronger boosting effect, yield elliptical structures. Thus, a connection between microscopic structures and the macroscopic boosting effect was found. With increased polymer content, the bending rigidity of the surfactant layer is increased, which makes the droplet more spherical. This allows us to conclude that the boosting effect was successfully transferred to the droplet morphology.

For many regions in the phase diagram, if the system appears to be in the one phase region, the surfactant dominates the structure. As it is for regions 1 and 2 of the droplet microemulsions and the domain spacing of the bicontinuous phase. Only in region 3 of the droplet microemulsion a structural change was observed with polymer addition. On the other hand the addition of the polymer

clearly influences the membrane elastic properties over the whole phase diagram (correlation length of the bicontinuous microemulsion, polydispersity of droplets and shape fluctuations at point 3). These subtle changes of the polymer are responsible for the macroscopic phase behavior and finally explain the polymer boosting effect.

Appendix

A: Tables of compositions

Table 7.1: *List of used polymers and their parameters.*

Polymer	M_n (PEP) [g/mol]	N_{PEP}	M_n (PEO) [g/mol]	N_{PEO}	M_n (PEP-PEO) [g/mol]
PEP_5PEO_2	4770	70	1200	27	5970
PEP_5PEO_5	4730	69	5750	131	10500
$PEP_{15}PEO_5$	14300	209	4650	106	18900
$PEP_{22}PEO_4$	23050	307	3220	73	26300
$PEP_{22}PEO_{22}$	23100	308	25800	588	49000

Table 7.2: *List of used polymers and their parameters continued.*

Polymer	ρ (PEP-PEO) [g/cm ³]	R_{ee} (PEP) [Å]	R_{ee} (PEO) [Å]
PEP_5PEO_2	0.910	67.1	30.7
PEP_5PEO_5	1.003	66.9	77.1
$PEP_{15}PEO_5$	0.922	121.9	70.0
$PEP_{22}PEO_4$	0.960	158.9	54.5
$PEP_{22}PEO_{22}$	1.036	159.0	181.2

Table 7.3: *Scattering length densities of used materials.*

	ρ [g/cm ³]	M [g/mol]	V [cm ³ /mol]	scattering length density [cm ⁻²]
D_2O	1.105	20.02	18.12	6.356E+10
H_2O	0.997	18.02	18.07	-5.582E+09
h-decane	0.726	142.28	195.96	-4.855E+09
d-decane	0.840	164.28	195.47	6.486E+10
h- $C_{10}E_4$	0.974	334.50	343.27	1.151E+09

Table 7.4: *Parameters of samples for SANS experiments on the bicontinuous microemulsion with homopolymer addition only.*

sample	$\phi_p\%$	ϕ_α	ϕ_γ	Ψ	d	ξ	$\kappa/(K_B T)$
w.p	0	0.5	0.132	0.125	311	132	0.361
	0	0.5	0.14	0.134	287	131	0.389
	0	0.5	0.146	0.139	270	130	0.411
	0	0.5	0.153	0.147	251	125	0.424
	0	0.5	0.159	0.153	241	123	0.434
	0	0.5	0.167	0.161	230	119	0.441
	0	0.5	0.174	0.168	219	114	0.441
	0	0.5	0.181	0.175	207	112	0.461
	0	0.5	0.187	0.181	198	107	0.459
	0	0.5	0.194	0.188	189	100	0.451
	0	0.5	0.201	0.195	181	86	0.403
	0	0.5	0.208	0.202	180	80	0.38
first portion	0.27	0.5	0.146	0.14	276	124	0.382
	0.27	0.5	0.153	0.147	262	122	0.396
	0.27	0.5	0.16	0.153	246	118	0.408
	0.27	0.5	0.168	0.161	234	115	0.418
	0.27	0.5	0.174	0.168	221	111	0.428
	0.27	0.5	0.182	0.176	211	106	0.429
	0.27	0.5	0.189	0.183	202	102	0.43
	0.27	0.5	0.196	0.19	192	95	0.42
	0.27	0.5	0.203	0.198	190	87	0.391
second portion	0.5	0.5	0.16	0.154	256	111	0.37
	0.5	0.5	0.167	0.161	244	109	0.379
	0.5	0.5	0.172	0.166	234	106	0.386
	0.5	0.5	0.179	0.173	224	102	0.388
	0.5	0.5	0.186	0.18	212	98	0.394
	0.5	0.5	0.193	0.187	205	93	0.388
	0.5	0.5	0.199	0.193	203	88	0.369
	0.5	0.5	0.199	0.193	203	88	0.369
third portion	0.78	0.5	0.184	0.178	220	90	0.347
	0.78	0.5	0.187	0.181	214	88	0.35
	0.78	0.5	0.184	0.178	219	89	0.347
	0.78	0.5	0.188	0.182	219	87	0.337

Table 7.5: *Parameters of samples for SANS experiments on the bicontinuous microemulsion with simultaneous homopolymer and diblock copolymer addition.*

sampl	$\phi_\delta\%$	$\phi_p\%$	ϕ_α	ϕ_γ	Ψ	d	ξ	$\kappa/(K_B T)$
sample1	3.87	0.5	0.5	0.104	0.097	386	168	0.369
	3.87	0.5	0.5	0.112	0.105	357	172	0.409
	3.87	0.5	0.5	0.119	0.113	332	174	0.446
	3.87	0.5	0.5	0.127	0.121	309	174	0.48
	3.87	0.5	0.5	0.135	0.129	289	173	0.51
	3.87	0.5	0.5	0.142	0.135	276	172	0.529
	3.87	0.5	0.5	0.148	0.142	263	160	0.516
	3.87	0.5	0.5	0.164	0.157	235	149	0.539
	3.87	0.5	0.5	0.178	0.171	213	125	0.498
	3.87	0.5	0.5	0.191	0.185	196	117	0.505
sample2	7.72	0.5	0.5	0.07	0.063	616	268	0.37
	7.72	0.5	0.5	0.078	0.071	534	246	0.392
	7.72	0.5	0.5	0.085	0.078	467	238	0.434
	7.72	0.5	0.5	0.094	0.087	426	243	0.485
	7.72	0.5	0.5	0.108	0.102	363	232	0.545
	7.72	0.5	0.5	0.123	0.116	311	217	0.594
	7.72	0.5	0.5	0.137	0.130	278	218	0.669
	7.72	0.5	0.5	0.151	0.144	249	210	0.717
	7.72	0.5	0.5	0.165	0.159	232	201	0.738
	7.72	0.5	0.5	0.179	0.173	211	157	0.634
sample3	3.83	0.99	0.5	0.117	0.111	337	156	0.392
	3.83	0.99	0.5	0.125	0.118	315	158	0.426
	3.83	0.99	0.5	0.133	0.127	295	156	0.45
	3.83	0.99	0.5	0.141	0.135	274	155	0.48
	3.83	0.99	0.5	0.157	0.150	250	150	0.512
	3.83	0.99	0.5	0.172	0.166	229	133	0.493
	3.83	0.99	0.5	0.187	0.181	228	138	0.514
	3.83	0.99	0.5	0.187	0.181	228	138	0.514
sample4	7.72	0.99	0.5	0.082	0.075	499	235	0.4
	7.72	0.99	0.5	0.090	0.083	453	229	0.43
	7.72	0.99	0.5	0.098	0.091	411	223	0.461
	7.72	0.99	0.5	0.107	0.100	372	206	0.471
	7.72	0.99	0.5	0.122	0.115	322	207	0.546
	7.72	0.99	0.5	0.136	0.130	283	196	0.588
	7.72	0.99	0.5	0.150	0.143	257	200	0.66
	7.72	0.99	0.5	0.163	0.156	238	183	0.652
	7.72	0.99	0.5	0.177	0.170	225	174	0.657
	7.72	0.99	0.5	0.177	0.170	225	174	0.657

B: The effect of diblock copolymer addition

Here we consider the calculation of the influence of the anchored diblock copolymer on the bending moduli of the membrane. That observation concerns to the case of an ideal polymer (the number of segments and its length are N and l , respectively). We assumed a hard wall interaction between the polymer and membrane (except for the anchoring point). The polymer is in the mushroom regime (i.e. it is not influenced by neighboring polymers).

For calculating elastic constants the expansion in the curvatures of the excess free energy of the system was used. So, the excess free energy for the polymer anchored to the curved surface is

$$\Delta\mathcal{F} = \mathcal{F}(H, K) - \mathcal{F}(0, 0)$$

where $\mathcal{F}(0, 0)$ is the free energy of the polymer anchored to the flat surface. This expression is expanded in powers of dimensionless variables HR and KR^2 up to the second order [55]. Where R is end to end distance of the polymer chain ($R = lN^\nu$). H and K are mean and Gaussian curvatures.

$$\Delta\mathcal{F}(H, K) = a_1HR + a_2(HR)^2 + a_3KR^2 + \dots \quad (7.1)$$

coefficients a_1, a_2 and a_3 of the expansion are calculated by comparing this expansion for cylindrical and spherical geometries where $H = c/2, K = 0$ and $H = c, K = c^2$, respectively. For the solution of this expansion the restricted partition function $Z_N(\vec{r}_{an}, \vec{r})$ of the polymer was constructed on the lattice with q nearest neighbors. This function is the number of chain configurations starting at point \vec{r}_{an} and ending at point \vec{r} . The reduced weight $G_N(\vec{r}_{an}, \vec{r}) = Z_N(\vec{r}_{an}, \vec{r})/q^N$ of the ideal polymer chain in the absence of the external potential obeys the diffusion equation

$$\left(\frac{\partial}{\partial N} - D\Delta_{\vec{r}} \right) G_N(\vec{r}_{an}, \vec{r}) = 0 \quad (7.2)$$

with initial condition

$$G_{N=0}(\vec{r}_{an}, \vec{r}) = \delta(\vec{r}_{an} - \vec{r})$$

and $D = l^2/q$ [56]. The total partition function calculated by integration of $Z_N(\vec{r}_{an}, \vec{r})$ over all positions of the free end of the polymer.

$$\mathcal{Z} = q^N \int d\vec{r} G_N(\vec{r}_{an}, \vec{r}) \quad (7.3)$$

The excess entropy is given by $\Delta\mathcal{F} = \ln(\mathcal{Z}/\mathcal{Z}_{fs})$ where \mathcal{Z}_{fs} is the partition function for the flat surface. In the following the solutions of the problem will be compared for the three cases: a flat surface, a spherical surface and a cylindrical surface. And the form of general expansion (eq. 7.1) will be obtained.

1. The solution of equation 7.2 for the plain $x = 0$ with a polymer anchored at $\vec{r}_{an} = (l_{an}, 0, 0)$ is [57]

$$G_t(\vec{r}_{an}, \vec{r}) = (4\pi t)^{-3/2} \left[e^{-[(x-l_{an})^2+y^2+z^2]/4t} - e^{-[(x+l_{an})^2+y^2+z^2]/4t} \right] \quad (7.4)$$

with $t \equiv DN$ and $R = lN^{1/2} = \sqrt{qt}$ and putting in 7.3

$$\mathcal{Z}_{hs} = q^N \operatorname{erf}[\sqrt{q}l_{an}/(2R)] = q^N \frac{\sqrt{q}l_{an}}{\sqrt{\pi}R} + q^N O((l_{an}/R)^3) \quad (7.5)$$

2. For a polymer anchored at distance l_{an} outside a sphere of radius R_s in spherical coordinates with $(r_{an} = R_s + L_{an}, \theta_{an} = 0, \phi = 0)$, equation 7.2 is solved by

$$G_t(\vec{r}_{an}, \vec{r}) = \sum_{n=0}^{\infty} G_{t,n}(r_{an}, r) P_n(\cos(\theta)) \quad (7.6)$$

where $P_n(x)$ are Legendre polynomials. The contribution for the $n = 0$ case is given by [57]

$$G_{t,0} = \frac{1}{4\pi r_{an} \sqrt{\pi t}} e^{-((r-R_s)^2+l_{an}^2)/4t} \sinh((r-R_s)l_{an}/2t) \quad (7.7)$$

Integrating over the free end of the chain gives:

$$\mathcal{Z}_{sp} = q^N 4\pi \int_{R_s}^{\infty} dr r^2 G_{t,0}(r_{an}, r) = \frac{l_{an}/R_s + \operatorname{erf}[l_{an}/(2\sqrt{t})]}{1 + l_{an}/R_s} \quad (7.8)$$

Where $\operatorname{erf}(x)$ is the error function. The ratio of the partition functions for the sphere and half space is:

$$\mathcal{Z}_{sp}/\mathcal{Z}_{hs} = \frac{1 + l_{an}/(R_s \operatorname{erf}[\sqrt{q}l_{an}/(2R)])}{1 + l_{an}/R_s} \quad (7.9)$$

For the limit $l_{an}/R_s \ll 1$, this leads to:

$$\mathcal{Z}_{sp}/\mathcal{Z}_{hs} \approx 1 + \sqrt{\pi/q}R/R_s \quad (7.10)$$

And excess entropy up to the second order in the mean curvature reads:

$$\Delta\mathcal{F}_{sp}/T = \sqrt{\pi/q}RH - (\pi/2q)(RK)^2 + O((RH)^3) \quad (7.11)$$

For the polymer anchored inside a sphere the result is equivalent [19]. T measures the temperature in energy units.

3. Similar calculations were done for the cylindrical geometry. For the polymer anchored outside an infinitely long cylinder of radius R_c , it was obtained [19]:

$$\mathcal{Z}_{cyl}/\mathcal{Z}_{hs} = 1 + \frac{\sqrt{\pi}}{\sqrt{q}}RH - \frac{1}{q}(RH)^2 + O((RH)^3) \quad (7.12)$$

Excess entropy for the polymer anchored outside the cylinder is

$$\Delta\mathcal{F}_{cyl}/T = \sqrt{\pi/q}RH - (\pi/2q + 1/q)(RH)^2 + O((RH)^3) \quad (7.13)$$

So finally combining results for spherical equation 7.11 and cylindrical geometry equation 7.13 the coefficients of equation 7.1 are $a_1 = \sqrt{\pi/q}$, $a_2 = -(1/q + \pi/2q)$, $a_3 = 1/q$. The excess free energy of an ideal polymer anchored to a curved surface relative to a flat surface is

$$\Delta\mathcal{F}_{po}/T = -\sqrt{\pi/q}RH + (\pi/2q + 1/q)(RH)^2 - 1/q(KR^2) + O((R/R_s)^3) \quad (7.14)$$

The gain of the free energy of the polymer is balanced by the bending energy of the membrane.

$$\Delta\mathcal{E}_{me} = 2c_A\kappa(RH)^2 + c_A\kappa_GKR^2 \quad (7.15)$$

The constant c_A is connected with the area affected by the presence of the polymer A ($A = c_A R^2$ and c_A of order one). The excess free energy is given finally by the sum $\Delta\mathcal{F} = \Delta\mathcal{F}_{po} + \Delta\mathcal{E}_{me}$, and after substitution the full expressions are obtained:

$$\Delta\mathcal{F}/T = -a_1RH + 2c_A(\kappa/T^2 - a_2/(2c_A))(RH)^2 + c_A(\kappa_G/T^2 - a_3/c_A)(KR^2) \quad (7.16)$$

Finally, the addition of the polymers change the elastic constants to

$$\kappa_{eff} = \kappa + T \frac{1 + \pi/2}{2c_A q} \approx \kappa + 0.21T \quad (7.17)$$

$$\bar{\kappa}_{eff} = \bar{\kappa} - T \frac{1}{c_A q} \approx \bar{\kappa} - 0.17T \quad (7.18)$$

Numerical values corresponds to the simple cubic lattice $q=2d=6$ and $c_A = 1$. Such values were used to obtain the expressions 2.14, 2.15, which perfectly describe the experimental case [2] and our results..

List of Figures

2.1	Introduction of principal curvatures	6
2.2	Droplet structure with polymers	15
2.3	Droplet microemulsion phase diagrams	16
2.4	Droplet to cylinder transition	20
2.5	Regimes for grafted polymers in a sphere	23
2.6	Core shell structure of a droplet	27
3.1	A SANS experiment	34
3.2	Divergence given by geometric factors	36
3.3	Multiple scattering correction	38
5.1	Fish tail phase diagram: homopolymer addition effect	44
5.2	Membrane content at fish tail point vs homopolymer content . . .	46
5.3	Cross section for several homopolymer contents	47
5.4	Domain size vs membrane content, several homopolymer contents	48

5.5	Correlation length vs membrane content, several homopolymer contents	49
5.6	Scaled domain size and correlation length vs membrane content	50
5.7	Bending modulus, several homopolymer contents	50
5.8	Bending modulus as a function of homopolymer content	51
5.9	Fish tail phase diagram: homopolymer and diblock copolymer addition effect	52
5.10	Membrane content at fish tail point vs homopolymer content	53
5.11	Membrane content at fish tail point vs. diblock copolymer grafting density	53
5.12	Cross section for homopolymer/diblock copolymer additions	54
5.13	Domain size vs membrane content, several polymers added	55
5.14	Correlation length vs membrane content, several polymers added	57
5.15	Scaled domain size and correlation length, several polymers added	58
5.16	Membrane content vs bending modulus, fixed diblock content	58
5.17	Membrane content vs bending modulus, fixed homopolymer content	59
5.18	Alternative calculation of bending rigidity (compare figs. 5.6, 5.7)	60
5.19	The membrane content and the bending rigidity vs homopolymer content	63
6.1	Characteristic phase diagram of a droplet microemulsion	65
6.2	Phase diagrams of droplet microemulsions with polymer addition	66

<i>LIST OF FIGURES</i>	101
6.3 Maximum oil content vs. amount of polymer	67
6.4 Regions of the phase diagram selected for SANS measurements . . .	68
6.5 Cross section for spherical droplets	70
6.6 Sphere radius and polydispersity.	71
6.7 Cross section for bidisperse objects	73
6.8 Cross section for cylindrical droplets	75
6.9 Cylinder radius and polydispersity	76
6.10 Cross section of cylindrical droplets, maximum oil content	78
6.11 Cross section of elliptical droplets	79
6.12 Ellipsoid radius and polydispersity	80

List of Tables

3.1	SANS Instrument details	35
6.1	Spherical droplet parameters	72
6.2	Cylindrical droplet parameters	77
6.3	Cylindrical droplet parameters at maximum oil content	77
6.4	Ellipsoid parameters	81
6.5	Fluctuation modes of ellipsoids	82
6.6	Summary of droplet structures	83
6.7	Data comparison for the $PEP_5 - PEO_5$ polymer addition	84
7.1	Used diblock copolymers and their characterization	91
7.2	Used diblock copolymers and their characterization	91
7.3	Scattering length densities of used materials	92
7.4	Parameters of samples for SANS experiments on the bicontinuous microemulsion with homopolymer addition only	93

7.5 Parameters of samples for SANS experiments on the bicontinuous microemulsion with simultaneous homopolymer and diblock copolymer addition	94
---	----

Bibliography

- [1] B. Jakobs, *Langmuir* **15**, 6707 (1999).
- [2] H. Endo M. Mihailescu M. Monkenbusch J. Allgaier G. Gompper D. Richter B. Jakobs T. Sottmann R. Strey I. Grillo, *J. Chem. Phys.* **115**, 580 (2001).
- [3] G. Gompper, in *33. IFF-Ferienkurs: Soft Matter*, Forschungszentrum Jülich GmbH, Jülich, 1991 , Kap. B9.
- [4] W. Helfrich, *Z. Naturforsch.* **28c**, 693XS (1973).
- [5] T. Sottmann S Müller R. Strey J. Allgaier D. Richter, *Abstr. Pap. Am. Chem. S.* **224**, 262 (2002).
- [6] G. Gompper and M. Schick, *Self-Assembling Amphiphilic System*, Academic Press, London, New York, 1994.
- [7] M. Teubner and R. Strey, *J. Chem. Phys.* **87**, 3195 (1987).
- [8] E. Eisenriegler A. Hanke and S. Dietrich, *Phys. Rev. E* **54**, 1134 (1996).
- [9] L. Peliti and S. Leibler, *Phys. Rev. Lett.* **54**, 1690 (1985).
- [10] D. Nelson T. Piran and S. Weinberg, *Statistical Mechanics of Membranes and Surfaces*, World Scientific, Singapore, 1989.
- [11] D. C. Morse, *Phys. Rev. E* **50**, R2423 (1994).
- [12] N. F. Berk, *Phys. Rev. Lett.* **58**, 2718 (1987).
- [13] N. F. Berk, *Phys. Rev. A* **44**, 5069 (1991).
- [14] M. Teubner, *Europhysics Letters* **14**, 403 (1991).
- [15] P. Pieruschka and S. A. Safran, *Europhysics Letters* **22**, 625 (1993).
- [16] P. Pieruschka and S. A. Safran, *Europhysics Letters* **31**, 207 (1995).
- [17] R. P. Feynman, *Statistical Mechanics*, Addison-Wesley, Reading, MA, 1972.

- [18] S. T. Milner and T. A. Witten, *J. Phys. France* **49**, 1951 (1988).
- [19] C. Hiergeist and R. Lipowsky, *J. Phys. II France* **6**, 1465 (1996).
- [20] H. Endo J. Allgaier G. Gompper B. Jakobs M. Monkenbusch D. Richter T. Sottmann R. Strey, *Phys. Rev. Lett* **85**, 102 (2000).
- [21] K. Yaman P. Pincus F. Solis and T. A. Witten, *Macromolecules* **30**, 1173 (1997).
- [22] S. A. Safran, *Phys. Rev. A* **43**, 2903 (1991).
- [23] S. A. Safran, *J. Chem. Phys.* **78**, 2073 (1983).
- [24] S. T. Milner S. A. Safran, *Phys. Rev. A* **36**, 4371 (1987).
- [25] M. Borkovec, *J. Chem. Phys.* **91**, 6268 (1989).
- [26] M. Borkovec, *Adv. Colloid Interf. Sci.* **37**, 195 (1992).
- [27] M. Gradzielski D. Langevin and B. Farago, *Phys. Rev. E* **53**, 3900 (1996).
- [28] L. D. Landau and E. M. Lifshitz, *Statistical Physics*, Pergamon, New York, 1980.
- [29] L. A. Turkevich S. A. Safran and P. A. Pincus, *J. Phys. Lett. (France)* **45,19**, L (1984).
- [30] R. Menes S. A. Safran R. Strey, *Phys. Rev. Lett* **74**, 3399 (1995).
- [31] E. M. Blokhuis W. F. C. Sager, *J. Chem. Phys.* **115**, 1073 (2001).
- [32] M. Manghi M. Aubouy C. Gay and C. Ligoure, *Eur. Phys. J. E* **5**, 519 (2001).
- [33] A. Guinier, *Ann. Phys.* **12**, 161 (1939).
- [34] M. Kotlarchyk S.-H Chen, *J. Chem. Phys.* **79**, 2461 (1983).
- [35] G. V. Schulz, *Z. Physik. Chem. B* **43**, 25 (1939).
- [36] B. H. Zimm, *J. Chem. Phys.* **16**, 1093 (1948).
- [37] J.-P. Hansen and I. R. McDonald, *Theory of Simple Liquids*, Academic Press, London, 1991.
- [38] N. W. Ashcroft and J. Lekner, *Phys. Rev.* **145**, 83 (1966).
- [39] J. S. Pedersen D. Posselt and K. Mortensen, *J. Appl. Cryst.* **23**, 321 (1990).

- [40] S. Hansen and J. S. Pedersen, *J. Appl. Cryst.* **24**, 541 (1991).
- [41] J. Schelten and W. Schmatz, *J. Appl. Cryst.* **13**, 385 (1980).
- [42] J. Allgaier A. Poppe L. Wilner D. Richter, *Macromolecules* **30**, 1582 (1997).
- [43] A. Hanke E. Eisenriegler and S. Dietrich, *Phys. Rev. E* **59**, 6853 (1999).
- [44] G. Gompper and D.M. Kroll, *Phys. Rev. Lett.* **81**, 2284 (1998).
- [45] H. Endo, *Dissertation*, Universität Münster, Münster, 2001.
- [46] D. Roux F. Nallet E. Freyssingeas G. Porte P. Bassereau M. Skourian J. Marignan, *Europhysics Letters* **17**, 575 (1992).
- [47] W. Helfrich, *Z. Naturforsch. A* **33**, 305 (1978).
- [48] T. Auth, *Dissertation*, Universität Köln, Köln, unpublished .
- [49] O. Holderer, Unpublished measurements by O. Holderer on PEP_{10} and PEO_{10} homopolymers, 2003.
- [50] A. Poppe, *Dissertation*, Universität Münster, Münster, 1998.
- [51] H. Kaya, *Dissertation*, Universität Münster, Münster, 2002.
- [52] F. Sicoli D. Langevin L. T. Lee, *J. Chem. Phys.* **99**, 4759 (1993).
- [53] G. Porod, *Small Angle X-ray Scattering (ed. Kratky, O.G.O.)*, Academic Press, London, 1982.
- [54] M. Mihailescu, *Dissertation*, Universität Münster, Münster, 2001.
- [55] R. Lipowsky, *Europhysics Letters* **30**, 197 (1995).
- [56] P.G. de Gennes, *Scaling Concepts in Polymer Physics*, Cornell University Press, Ithaca, 1979.
- [57] H. Carslaw and J. Jaeger, *Conduction of heat in solids*, Clarendon Press, Oxford, 1959.

Acknowledgments

I would like to thank Prof. Dr. D. Richter for giving me the opportunity to work at his Institut für Neutronenstreuung, IFF of Forschungszentrum Jülich, for his support and supervision.

I am particularly grateful to Dr. H. Frielinghaus. His close supervision and support, his knowledge and experience in field of polymer physics and neutron scattering. His contribution to this work cannot be appreciated highly enough.

I would like to thank Prof. Dr. G. Gompper for the brilliant and inspiring discussions, for his fruitful and clear explanations of the physics of microemulsions.

Many thanks to T. Auth for his ideas in theoretical interpretation of results.

I am grateful to Dr.J. Allgaier for the synthesis of the polymers and the help in the preparation of samples.

I would like to thank to Dr. M. Heiderich for the technical support at KWS2.

I sincerely thank to all the people, whom I have met in FZ-Jülich for their friendly atmosphere and careful attention.

Lebenslauf

Dmytro Byelov,

geboren am 21 Juli 1974 in Odessa, Ukraine;
verheiratet, 1 Sohn;

Vater: Vladimir V. Byelov;
Mutter: Valentina V. Byelova, geb. Tarasenko.

- Schulbildung:** 09/1981 - 07/1989 Mittelschule für Allgemeinbildung 23 der Stadt Odessa.
09/1989 - 06/1991 das Lyzeum 36 der Stadt Odessa.
- Hochschulreife:** 18/07/1991 Abitur.
- Studium:** 09/1991 - 07/1996 Studium der Physik an der I.I. Mechnikov Staats-Universität in Odessa, Ukraine.
- Diplomarbeit:** 09/1995 - 07/1996 Thema: "The contact resistance in quantum nano-chemes";
I.I. Mechnikov Staats-Universität in Odessa, Ukraine.
- Prüfungen:** 03/07/1996 Diplom im Fach Physik an der I.I. Mechnikov Staats-Universität in Odessa, Ukraine.
- Promotionsstudiengang:** 10/2002 - 09/2003 Chemie und Pharmazie an der Westfälischen Wilhelms-Universität, Münster.
- Tätigkeiten:** 11/2000 - 11/2003 Physiker mit Doktorandenförderung am Forschungszentrum Jülich.
- Dissertation:** seit dem November 2000 am Institut für Festkörperforschung, Forschungszentrum Jülich;
Betreuer: Prof. Dr. Dieter Richter;
Mitbetreuer: Dr. Henrich Frielinghaus.

Jülich, 10. November 2003

